https://eprints.gla.ac.uk/285749/

Emerging Two-Dimensional Metal Oxides: From Synthesis to Device Integration

Kui Zhou, Gang Shang, Hsiao-Hsuan Hsu, Su-Ting Han, Vellaisamy A. L. Roy and Ye Zhou*

Dr. K. Zhou, Prof. Y. Zhou

Institute for Advanced Study, Shenzhen University, Shenzhen 518060, P. R. China.

E-mail: yezhou@szu.edu.cn

G. Shang, Prof. S.-T. Han

College of Electronics and Information Engineering, Shenzhen University, Shenzhen 518060, P. R. China.

Prof. H.-H. Hsu

Department of Materials and Mineral Resources Engineering, National Taipei University of Technology, Taipei, Taiwan

Prof. V. A. L. Roy

James Watt School of Engineering, University of Glasgow, Glasgow, G12 8QQ UK

Abstract: Two-dimensional (2D) metal oxides have aroused increasing attention in the field of electronics and optoelectronics due to their intriguing physical properties. In this review paper, an overview of recent advances on synthesis of 2D metal oxides and their electronic applications is presented. First, the tunable physical properties of 2D metal oxides that related to the structure (various oxidation-state forms, polymorphism, *etc.*), crystalline and defects (anisotropy, point defects, and grain boundary), and thickness (quantum confinement effect, interfacial effect, *etc.*) are discussed. Then, advanced synthesis method for 2D metal oxides besides mechanical exfoliation are introduced and classified into solution process, vapor phase deposition, and native oxidation on metal source. Later, the various roles of 2D metal oxides in widespread applications, i.e., transistors, inverters, photodetectors, piezotronics, memristors, and potential applications (solar cell, spintronics and superconducting devices) are discussed. Finally, the outlook of existing challenges and future opportunities in 2D metal oxides are proposed.

1. Introduction

Two-dimensional (2D) materials have fascinating properties including tunable bandgap, high carrier mobility, superior immunity to short-channel effect, high microfabrication and monolithic 3D integration compatibility, high transparency, mechanical flexibility and strong quantum confinement effects, which make them exhibiting extraordinary potential toward next-generation electronics, optoelectronics, spintronics and beyond.[1-4] The capability of accessing to atomically thin structure makes 2D materials approach to the physical limit of the condensed matter and opens new horizons for novel properties that are dissimilar from their bulk counterparts towards innovative applications.[5-8] With the continuous preparation of 2D materials, their influence gradually covers the whole range from broadband insulators to superconductors, in which graphene,[9-10] h-BN,[11-12] transition metal dichalcogenides (TMDs),[13-14] MXenes,[15-16] and 2D elemental semiconductors,[7] have attracted the most attention of researchers.

Despite considerable progress, these 2D materials still suffer from some inherent limitations. First of all, the pristine surfaces of 2D materials tend to form van der Waals (vdW) gap with contacted metal electrodes instead of covalent bonds due to the chemically inert surfaces.[17] The vdW gap plays the role of an extra "tunnel barrier" for carriers beyond the inherent Schottky barrier, which greatly hinder the charge injection from metal electrodes. Furthermore, dangling-bond-free characteristic of 2D materials also impede the direct growth of high-quality dielectric materials on their surface due to the wetting problem.[18] Secondly, the intrinsic optical features are not sufficiently diverse to satisfy broadband optoelectronic applications including UV photodetector and transparent transistor due to the insufficient candidates of 2D materials with bandgap in the range of 3 to 5 eV. Most metal chalcogenides and Mxenes possess the bandgap in range of 1 to 2 eV that is corresponding to visible and infrared wavelength while the h-BN has a bandgap of up to 6 eV that is capable for vacuum ultraviolet (UV) detection. The 2D materials with bandgap of < 3.0 eV are not efficient for detecting UV light that has photon energy > 3.0 eV since a considerable part of the absorbed photons dissipates in the form of non-radiative relaxation of photocarriers. Third, 2D materials in wafer-scale are critical requirement for their up-scaling application in integrated circuit towards high-end electronics or optoelectronics. However, most vdW 2D materials are usually obtained as small flakes in micrometer scale through exfoliation. Bottom-up growth can significantly improve the lateral size of vdW 2D materials, while seamless large-area and well-controlled films with proper layer thickness and lattice orientation is still an important challenge.[19] Moreover, the

WILEY-VCH

stability of materials is critical for the lifespan and reliability of a practical device in various applications. Unfortunately, most of 2D materials are susceptible to ambient environment due to the high chemical activity. Temperature, optical radiation, adsorbed molecules, stress and external electric field can drastically tune the lattice structures or electronic structures of 2D materials, and some of these issues may degrade the performance. Consequently, the issue of environmental stability and associated high-cost have to be settled before practical use.[20]

Metal oxides are widely applied in electronic and optoelectronic fields, which have the advantages of low cost, easy manufacture and high stability in environments. The bandgaps of metal oxides are mostly located in the range of 3 to 5 eV, which is complementary to the vdWs 2D materials. Metal oxides exhibit a combination of visible-light transparency, high conductivity, and high electron mobility, which offer a variety of usages in (opto)electronic devices, such as displays, thin film transistors, transparent electronics, flexible electronics and high-power electronics. Currently, semiconductor metal oxides are rarely applied as channel materials for scaled atomically thin electronic devices because they usually present amorphous state in industrial application with low electron mobility of about 10 cm^2 V^{-1} s^{-1}. The film thickness of the deposited metal oxides is various in the range from a few nanometers to hundreds of nanometers. However, recent advance in atomic layer deposition (ALD) technique has developed the oxide semiconductor with sub-1 nm channel thicknesses and high electron mobility (μ_{FE}) of >10 cm^2 V^{-1} s^{-1},[21-24] making oxide semiconductor transistors as promising candidates in CMOS back-end-of-line (BEOL) for monolithic three-dimensional (3D) integrations. The insulating metal oxides can be used as high-κ dielectric in field-effect transistor (FET), aiming to achieve the equivalent oxide thickness of sub-1 nanometer. Metal oxide thin film has to take crystallinity into consideration in the electronic applications in view of device performance, processing implementability and compatibility. Besides, metal oxide thin films have also been studied in other electronic applications, such as spintronic and superconducting electronics.[25-28]

Compared with metal oxide thin films, 2D metal oxides not only inherit the properties of former, but also may exhibit unprecedented properties due to the quantum confinement effects and interfacial interactions. Moreover, recent advance of synthesis methods has provided new technical supports for 2D metal oxide studies, realizing the preparation of atomically thin nonlayered metal oxide and novel layered 2D metal oxides.[29-32] Thus far, 2D metal oxides have substantially expanded the scope of the 2D family and shown great potential for electronics and optoelectronics. For example, a novel p-type 2D hexagonal TiO$_2$ (h-TiO$_2$) demonstrated a high hole mobility up to 950 cm^2 V^{-1} s^{-1}.[32] The

high-κ dielectric 2D perovskite $SrTiO_3$ formed vdW interface with channel materials in 2D FET. The short-channel CVD-MoS_2/$SrTiO_3$ based FETs demonstrated a steep subthreshold swing (SS) of 79 mV dec^{-1} and on/off current ratio of 10^6.[33] The SS of MoS_2 based FET reached 64 mV dec^{-1} for 2D Sb_2O_3 as the dielectric.[34] In addition, 2D ZnO-based photodetector exhibited excellent performance for UV detection with responsivity of 2.0×10^4 AW^{-1} and detectivity of 6.83×10^{14} Jones at wavelength of 254 nm.[35] The photodetectors based on 2D Fe_3O_4 nanosheets realized ultrabroadband response ranging from UV (375 nm) to long-wavelength infrared (10.6 μm).[36] Moreover, a few unit-cell thick ZnO (~1.1 nm thick) showed a giant piezoelectric coefficient of 80 ± 0.8 pm V^{-1}.[37] 2D graphitic $Zn_{1-x}Co_xO$ (gZCO) monolayer and bilayer possessed long-range ferromagnetic order at room-temperature and environmental stability, which is promising for spintronics, magneto-optics, as well as new quantum and topological phases.[38] The monolayer (half unit-cell) $Bi_2Sr_2CaCu_2O_{8+x}$ (Bi-2212) exhibited a high superconductive transition temperature with T_c value of ~88 K.[39] Besides, 2D oxides have also shown application potential in resistive memory,[40] memtransistor,[41] and electro-photonic memristor,[42] which is promising for future neuromorphic computing systems.

In this article, to distinguish from metal oxide thin films, we understand 2D metal oxides as those metal oxides (including both layered and nonlayered structures) that could exist without a substrate and can reach to only single- or few-atoms thick (typically less than 5 nm). In other words, they can be isolated as free-standing materials from synthesis substrate. With this definition in mind, an overview of recent advances on synthesis of 2D metal oxides and their electronic/optoelectronic applications are presented (**Figure 1**). First, the tunable physical properties of 2D metal oxides that related to the structure (various oxidation-state forms, polymorphism, *etc*.), crystalline and defects (anisotropy, point defects, and grain boundary), and thickness (quantum confinement effect, interfacial effect, *etc*.) are discussed in section 2. Then, advanced synthesis method for 2D metal oxides beside mechanical exfoliation are introduced and classified into solution process, vapor phase deposition, and native oxidation on metal source in section 3. Later, the various roles of 2D metal oxides in widespread applications, *i.e.*, transistors, inverters, photodetectors, piezotronics, memristors, and potential applications (solar cell, spintronics and superconducting devices) are summarized in section 4. Finally, the outlook of existing challenges and future opportunities in 2D metal oxides are proposed.

2. Crystal structures and properties of 2D metal oxides

2.1. Crystal structure of 2D metal oxides

To date, the reported 2D metal oxides cover the insulator (e.g., HfO_2, Sb_2O_3, $SrTiO_3$), semiconductor (n-type, such as In_2O_3, ZnO, SnO_2, β-Ga_2O_3, γ-Bi_2O_3; p-type, such as SnO, h-TiO_2), metallic oxide (e.g., MO_2, VO_2), superconductor (e.g., Bi-2212) and magnet (e.g., gZCO). The properties and applications of these 2D metal oxides are closely related to the structures. Here, due to the complexity and diversity of 2D metal oxides, instead of introducing them one by one, we would like to discuss some common features in structures, such as layered/nonlayered structures, various oxidation-state forms and polymorphism. Then some advanced structural characterization techniques and methods are briefly introduced, as well as research status of novel 2D metal oxides.

Table 1 summarized the structure information of 2D metal oxides in experimental studies. Obviously, 2D metal oxides are in general binary or complex oxides with one or more metallic elements, presenting various crystalline structures with interconnected building blocks (Figure 2a). These structures can be categorized into non-layered and layered structure. The non-layered 2D metal oxides feature the growth in 3D directions but a restriction in out-plane direction, leading to unsaturated dangling bonds on the surface (Figure 2b). On the contrary, the layered 2D metal oxides consist of stacking monolayer *via* vdW interaction, which have great potential to be thinned down to atomic scale without sacrificing the crystalline quality in comparison with the bulk counterparts (Figure 2c). Generally, binary metal oxide crystals consist of MO_n building blocks (M for metal, O for oxygen, *n* is the coordination number of oxygens around metal center in the range from three to six) linked by corner, edge and face sharing, in which one M atom and *n* O atoms are bonded in the form of tetrahedra (e.g., ZnO), octahedra (e.g., In_2O_3, SnO_2, MoO_3), pyramid (e.g., SnO) or polygonal (e.g., Sb_2O_3). In particular, 2D Sb_2O_3 consists of 0D molecules of Sb_4O_6, in which the building blocks of Sb_4O_6 adamantanoid cages are connected by vdW forces even in each layer.[43] Except the binary metal oxides, some complex metal oxides have also drawn great researching interests. Typically, perovskite oxide ABO_3 crystallizes as non-layered structure, in which each A cation is located at the center of the cube that is composed of eight corner-sharing BO_6 octahedra (Figure 2d). Recent progress has demonstrated a freestanding and high crystalline ABO_3 perovskite film with a single unit cell by reactive molecular beam epitaxy on sacrificial buffer layer.[44] Besides, some layered perovskites (*e.g.,* $Sr_2Nb_3O_{10}$,[30] $Ca_2Nb_3O_{10}$[45]) can be exfoliated into monolayer-thick from DJ phase

layered oxide by ion-exchange assist exfoliation, which adopt the general formula as $(A_{n-1}B_nO_{3n+1})$ (Figure 2e). Besides, other more complex metal oxides are formed by orderly combination of different MO_n building blocks. Several common and typical crystal structures of 2D metal oxides are shown in Figure 2f-i.

A given metal, especially transition metal, usually has a family of oxides that are composed of metal in different oxidation states. The oxidation state of metal cation is critical to determine the structure and property of metal oxide. A controlled oxidative reaction environment can effectively regulate the oxidation state of metal and thus dominate the composition and structure of 2D metal oxide. For instance, SnO_2 is n-type semiconductor with nonlayered structure while SnO presents layered structure and exhibits high-mobility in p-channel FETs and complementary devices (Figure 2f). In a typical process, 2D SnO_2 can be obtained by liquid Sn printing method at ~250 °C in ambient air but 2D SnO should be prepared at lower temperature (~200 °C) to avoid the formation of SnO_2.[46] The post annealing process can turn the SnO into SnO_2. Therefore, to get desired oxidation-state form, the great attention should be paid to the control of oxidation environment during the 2D metal oxide synthesis. Moreover, it also enlightens us that post oxidation or reduction process could convert the 2D metal oxides into other oxidation-state forms.

Diverse coordination mode between metal and oxygen will lead to various crystal phase of a certain metal oxide, namely polymorphism. The polymorph phase is often expressed as chemical formula of metal oxide with a prefix of Greek letter (*e.g.,* α-MoO_3, β-Ga_2O_3, γ-Bi_2O_3). In most cases, the crystal phase of metal oxides is often determined by the temperature at which the crystal is formed, as well as pressure and humidity.[47-49] The oxygen vacancy defects and adsorbed species on the surface could help to decrease surface energy and stabilize the metastable phase at ambient condition.[43, 48, 50] Moreover, the reversible phase transition phenomenon widely exists in metal oxide, accompanying by the change of properties. For example, 2D Sb_2O_3 demonstrates a reversible transition between α- and β-phase by modulating the temperature, in which α- and β-Sb_2O_3 consists of 0D Sb_4O_6 molecules and 1D chains of $[SbO_3]$ trigonal pyramids, respectively.[43] (Figure 2g). The experiment study reveals that α-phase shows an insulating property while β-phase exhibits a semiconducting behavior, which may be attributed to the decrease of band-gaps from 3.0 eV (α-phase) to 2.1 eV (β-phase).[51] Another example is that VO_2 shows 10^3 to 10^5 times resistivity difference between the metallic and the insulating phases of VO_2.[52] Sometimes, the phase transition is irreversible, for example, from layered gZnO to nonlayered wurtzite ZnO,[53] or from

layered $h-TiO_2$ to non-layered anatase phase transition.[32] Therefore, it can achieve a series of polymorphic 2D metal oxides with different properties by post phase transition treatment.

Given that the phenomena of various oxidation-state forms and polymorphism widely exist, the structure identification is important and challenging in 2D metal oxide study. Mostly, the structure of 2D materials can be determined by comparing to the known bulk crystal phase with the assist of diverse characterization methods, such as X-ray photoelectron spectroscopy (XPS), transmission electron microscopy (TEM), Raman spectra, *etc*.[36, 41, 50] However, some novel 2D metal oxides have no bulk phase counterparts, such as gZnO, h-BeO and $h-TiO_2$.[32, 54-55] Thus, several powerful atomic-structure analysis techniques have been introduced to reveal the atomic configuration of 2D metal oxide, which include scanning tunneling microscopy (STM), surface x-ray diffraction (SXRD), and high-angle annular dark-field scanning transmission electron microscopy (HAADF-STEM).[32, 53, 55] Moreover, the density functional theory (DFT) calculations and other simulation methods are always helpful to identify the crystal phase and orientation.[32, 54]

The discovery and preparation of these novel 2D metal oxide structure further expand the 2D metal oxide family and their potential applications. However, some novel 2D metal oxides (e.g., h-CoO, h-Ni_2O_3, h-Cu_2O) have not been systematically studied and demonstrated in electronic and optoelectronic applications, probably since the preparation of these 2D metal oxides requires special instrument and strict synthesis conditions.[32] Some 2D metal oxides can only be achieved in small lateral size that is difficult for device fabrication.[55-56] In addition, many metal oxide monolayers with different atomic structures have been investigated by first-principles calculations, which exhibit various electrical and optical properties, indicating a wide range of opportunities for future electronic and optoelectronic applications.[57] Therefore, developing and preparing 2D metal oxides is an emerging and promising topic towards advanced 2D devices.

2.2. Defects in 2D metal oxide

2D metal oxides are attracting growing research interest owing to their diverse structures and physical properties. Moreover, the ubiquitous defects in 2D metal oxides offer another opportunity to tailor their electronic and optoelectronic properties. Herein, we will introduce the anisotropy in monocrystalline (almost defect-free) 2D metal oxides and then discuss the defect effects on their properties, such as charge transport ability, dielectric performance, optical properties, magnetic phenomenon.

The crystalline solids possess anisotropic physical property due to their ordered and periodic atom arrangement. The properties are dependent on measuring direction and thus affected by the solid nature including refractivity, thermal conductivity, electrical conductivity, photoelasticity and so on. On contrary, the amorphous solids hold tightly packed random arrangement of the constituent particles, which are said to be isotropic since the particle distribution will be generally different along each axis. Taking the anisotropy into account is a useful strategy for improving the physical properties and expanding the breadth of applications of 2D metal oxides.

As shown in Figure 3b, 2D vdW α-V_2O_5 possesses strong in-plane optical anisotropy, and the strongest intensity of A_{1g} 482 cm^{-1} mode occurs once the incident light is polarized along the long axis of rectangular α-V_2O_5 flakes.[58] Recently, α-MoO_3 has attracted a numerous of research interests on anisotropic photonic quasiparticles in vdW materials due to the discovery of in-plane hyperbolic phonon polaritons in such a biaxial polar crystal.[59-62] The twisting stacked α-MoO_3 slabs has achieved a configurable light-matter waves-phonon polaritons over a broad range of twist angles, giving the potential for tunable nanophotonic devices.[61-62]

Figure 3c exhibits the electrical conductivity anisotropy of α-V_2O_5. The material shows enormously strong anisotropic angular-dependent electrical conductance with *a* axis, leading to 2 orders of magnitude less conductance compared to that of *b* axis. The directional dependent conductivity is predicted to be correlated to deformation potentials, 2D elastic constants and absolute phonon-scattering limited mobilities.[61]

Defects seem to be inevitable in solid materials, which terminate the translational symmetry of the crystal lattice and affect the anisotropy theoretically. The defects can be broadly categorized as volumetric defects (such as pores), planar defects (such as grain boundaries), linear defects (dislocations) and point defects (such as vacancies).[63] All types of defects could have more-or-less impact on the electronic and optoelectronic properties of metal oxides.[64] Herein we mainly focus on point defects and grain boundary as they are the most intrinsic defects and play a crucial role in modulation of electronic and optoelectronic properties (Figure 3d and 3g). To get insight of the chemical principle underlying the defect effects, the electronic structures of metal oxides are briefly introduced at first.

2D metal oxides usually possess the thickness in cluster- or molecule-level while lateral size far beyond the molecule-level. In the theoretical studies, the molecular orbitals diagram with frontier orbitals (highest occupied molecular orbital (HOMO) and lowest unoccupied molecular orbital

(LUMO)) are usually used for describing the electronic energy levels in building blocks (metal oxide clusters) of 2D materials, in which HOMO and LUMO is closely related to valence band (VB) and conduction band (CB) of bulk phase in band theory. The simplified the molecular orbitals diagram of n-type and p-type metal oxides are depicted in Figure 3e.[65] In n-type metal oxides, the electron-transport path in the CB correlate to the LUMO that is mainly made of metal s orbitals. The s orbitals in CB are spherically extended and sufficiently overlapped, leading to large electron mobility even in the amorphous structure. Besides, the strong ionic bonds cause low-density electron traps in the bandgap. However, VB (the transport path for holes) correlate to the HOMO that mainly consists of anisotropic and localized oxygen 2p orbitals, leading to relative low mobility. The hybridized VB that is mainly composed of orbitals in metal ions can create a less localized hole-transport pathway for high hole mobility. For example, Sn(5s) based HOMO and Cu(3d) based HOMO dominate the hole transport paths in VB of p-type SnO and Cu_2O, respectively.[66]

The defects will change the form of metal-oxygen coordination in metal oxide cluster and therefore shift the frontier orbitals, which could introduce extra energy levels into the band gap of metal oxides. The defect-introduced trap states can be distinguished as shallow states (usually within ≈26 meV close to band edge at room temperature) and deep states, leading to great impact on the electronic and optoelectronic properties of metal oxides (Figure 3f).[64] In general, the defects could allow materials absorption and emission at longer wavelengths. The shallow states can tune the conductivity of metal oxides while the deep states, can act carrier killer for trapping or the recombination of charges, and can also lead to a Fermi level pinning in the bandgap.

The point defects can be generally sorted into two categories, which are the intrinsic species (e.g., vacancies, interstitials, dangling bonds) and the extrinsic species (e.g., substitution or doping) (Figure 3d). The intrinsic defects will result in non-stoichiometric ratio in 2D metal oxides. The defects like oxygen vacancies (V_O) or metal interstitials (M_i) will transfer one to several electrons and thus affect the electron conductivity. On the contrary, metal vacancies (V_M) is the probable origin of the p-type conductivity in the metal oxides while oxygen interstitial (O_i), as a deep-level defect, have also been identified as possible acceptor defects.[66] Notably, owing to the low formation energy, V_O can produce enough electrons that benefit for n-type conductive metal oxides, but also annihilate holes, making the difficulty in high performance p-type metal oxide.[67] The high concentration of V_O can turn the insulator into conductor, which is one of the common mechanism in memristive devices.[68] The V_O on the surface can help to stabilize the crystal phase of metastable metal oxide polymorph

WILEY-VCH

(e.g., 2D γ-Bi_2O_3) at room temperature. V_O as trap on the surface can lead to nonlinear relationship between photocurrent and light intensity.[50]

The extrinsic substitution or doping in metal oxide also can modulate the conductivity,[69] magnetism,[38] and superconductivity.[39] Incorporation of Zn dopants into the single unit-cell thick In_2O_3 can shift the Fermi level toward the conduction band edge. Low-level doping can significantly improve the conductivity of the semiconducting In_2O_3 host to 5.95×10^2 Ω^{-1} cm^{-1}, while high-level doping sample exhibits metallic behavior with relatively low conductivity of 7.41×10^3 Ω^{-1} cm^{-1}.[69] Changing the doping level of Co substitution in nonmagnetic gZnO monolayer and bilayer can endow the new 2D metal oxide (namely gZCO) long-range ferromagnetic property with tunable coercive field at room temperature and environmental stability.[38] $Bi_{1.9}Sr_{2.1}CaCu_2O_{8+x}$, as a modified stoichiometric form of layered 2D superconductor $Bi_2Sr_2CaCu_2O_{8+x}$ (Bi-2212), exhibits a highest transition temperature (T_c) of 88 K at optimal doping. Doping holes into the CuO_2 planes of Bi-2212 can reach a T_c of 91 K.[39]

Grain boundary defects also play important role in charge transport and material tolerance. Generally, single crystalline 2D materials are preferable for electronic and optoelectronic devices due to the less of traps and dispersion from structure defects. However, the formation of single crystal usually requires high cost and complex process, thus, grain boundary defects will be always found in the large area crystalline materials. However, the formation of single crystal usually requires high cost and complex process, thus, grain boundary defects will be always found in the large area crystalline materials. As shown in Figure 3d, the interface between two adjacent grains becomes electrically active due to the charge trapping arising from the localized gap states (dangling bonds, interfacial defects, dopants or impurities). The charge transport in crystalline materials with grain boundary defects will be mainly dominated by the grain size and grain boundaries, in which sub-gap defects between grains can significantly hinder charge transport, resulting in low mobility.[70] The carriers can pass through the grain boundary by thermionic emission, tunneling or hopping phenomenon (Figure 3h).[71] Grain engineering in enlarging the grain size and decreasing the sub-gap defects can significantly improve the charge transport in 2D metal oxides.[72]

Similar to monolayer graphene, the grain boundary can also be regarded as line defect in atomically thin 2D metal oxide.[73] 2D ITO (~1.5 nm thick) features the interconnected 2D grains with small grain size as shown in Figure 3i. These grain boundaries also reduce the mobility in 2D semiconductors. For instance, the 2D ITO featured polycrystalline structure which exhibited a Hall effect mobility of 14 cm^2 V^{-1} s^{-1} while the mobility of monocrystalline ITO was estimated to be ~290 cm^2 V^{-1} s^{-1}.[29]

However, 2D metal oxide generally shows a higher conductivity than nanoparticle or sol-gel printing film, where the boundary/grain ratio of 2D grains is much lower than that of the 3D nanoparticle film with similar grain size. Thus, the 2D polycrystalline metal oxide will have less inter-grain transport of charge compared to the 3D nanoparticle film, indicating a higher conductivity.[74]

Furthermore, the ideal dielectric thin films should prevent leakage paths and have sharp interfaces with semiconductor and the gate material, which can further lead to enhanced mobility and stability of the transistor. The defect states on the surface of dielectrics could broaden the distribution of the density of states of the semiconductor and hence obstruct the charge transport. The grain boundary in dielectric materials will cause current leakage and poor long-term endurance. Recent studies have revealed that the single crystal materials could be the best choice for dielectrics, especially in 2D nanoelectronics, owing to their ideal atomically sharp and defect-free surface.[75-76] 2D ultrahigh-κ single-crystalline perovskite oxide[33] and metal oxide[34] can be promising vdW dielectric materials in 2D FET, while hBN[77] and CaF_2[78] are also proper candidates.

2.3. Thickness effects in 2D metal oxides

Compared to the bulk phase, the ultrathin feature of 2D metal oxides can make significant change in their optical and electronic properties due to the quantum confinement and interfacial effect (**Figure 4**a). Thinning the bulk metal oxide into 2D form and tunning the thickness in the 2D range can modulate the bandgap, Raman spectrum, light transmittance, carrier mobility, efficient dielectric, piezoelectric property, superconducting transition temperature and magnetic moment of 2D metal oxides.

The Raman spectrum can be used to identify the atomic layers of the 2D materials on the basis of the peak shift.[79-80] As stated in the classical harmonic oscillator model, the frequencies of both A_{1g} and E_g vibrational modes are expected to decrease when the film thickness is reduced from bulk to 2D limit owing to the weak interaction between atoms in neighboring layers. However, no obvious shift in the peak positions of Raman spectrum can be observed during the transition from bulk to 2D SnO (Figure 4b). The reason is that the dielectric screening of the effective Coulomb potential gets less effective in the transition from bulk to 2D materials, resulting in the enhancement of long-range electrostatic force.[81-82] A tradeoff between long-range dielectric screening effects and the short-range inter layer effects may cancel out the influence on the Raman characteristic peak position. Nevertheless, the integrated intensity ratio of A_{1g} and E_g peaks increases almost linearly with the decrease of film thickness, which can be used as a parameter to distinguish the thickness of the SnO.

For the optical study, the atomically thin feature endows the 2D metal oxide high transparency and increasement of the light adsorption in short wavelength range. 2D SnO film exhibited an increasing light transmittance across the all-range spectrum as the thickness decrease (Figure 4c). In 2020, 2D ITO (~1.5 nm thick) that fabricated by liquid metal printing method exhibited minimal absorption in the visible region with a transmittance loss of 0.4%. In addition, the bilayer ITO can maintain a transparency of 99.3%. Therefore, 2D metal oxides have been proven as a promising alternative in the circumstance that have critical requirement on transparency.[29] Figure 4c also exhibits a large blue shift in light adsorption as the thickness decrease, which could be understood by the quantum confinement effects. The change in adsorption wavelength can alter or improve the performance of 2D materials in optoelectronic applications.

2D metal oxides experience transitions in the band structure as the thickness reduce to a few nanometers or sub-nanometer, which will further affect the conductivity and mobility of the materials. As shown in Figure 4d, the multi-layer SnO mobility shows monotonic increase with increased number (5 to 12) of channel layers, while the mobility starts reducing and reaches ~0.1 cm^2 V^{-1} s^{-1} when the number of channel layers is further increased to 30 layers. The thickness-dependent mobility variation occurs owing to the interlayer coupling and screening effects in layered materials.[83] Similarly, 2D h-TiO_2 has layered crystal structure with monolayer thickness of ~0.55 nm. As shown in Figure 4e, scanning tunnelling spectroscopy (STS) revealed that the thickness-dependent bandgap due to the quantum confinement effects, in which the bandgap energies for mono-, bi- and tri-layered h-TiO_2 were 2.35, 2.0 and 1.85 eV, respectively. The 0.5-nm-thick h-TiO_2-based FET device demonstrated a hole mobility of ~10 cm^2 V^{-1} s^{-1}, while a ~5-nm-thick device showed a mobility of 950 cm^2 V^{-1} s^{-1} at room temperature.[32] Amorphous In_2O_3 thin film on the surface of Al_2O_3 shows a bandgap enhancement from 1.40 to 2.43 eV by decreasing the thickness from 1.5 to 0.7 nm, which can be understood by the quantum confinement effect like layer dependent band-structures in 2D vdW materials.[24] The decreasing mobility can be attributed to the stronger disorder induced potential fluctuation in CB and electron scattering in atomic layer thin In_2O_3 film.

Metal oxides can also be promising candidates of high-κ dielectric. The metal oxide usually exhibits a lower effective dielectric constant (ε_{eff}) when the thickness decreases to nanoscale (Figure 4f). Although it is still a debate that size-related permittivity suppression occurs on the high-κ oxide surface. The creditable explanation is given that incomplete screening occurs in real metal/dielectric interface and some of the voltage drop in the electrodes. During the miniaturization of high-κ dielectric thickness, the experimentally observed reduction in effective permittivity is usually

expressed in terms of low interfacial capacitance density (dead layer) presenting at the electrode/dielectric boundaries and acting in series with the pristine bulk capacitance (Inset of Figure 4g). Hence, the overall effective dielectric constant (ε_{eff}) is given by: $t/\varepsilon_{eff} = t/\varepsilon_{bulk} + D$, in which t is the dielectric layer thickness, ε_{bulk} is the dielectric constant of the bulk material, D is constant related to interfacial dead layer. Thus, ε_{eff} significantly decreases when the thickness is small.

The thickness also significantly affects the piezoelectric properties of 2D metal oxide. Thinning the physical dimensions of bulk materials can induce an ability to withstand extreme deformation and enhanced surface area-to-volume ratios with optimized surface energies, which have been demonstrated or predicted to introduce or enhance the piezoelectricity of the materials.[84] Mahmood et al. reported a thickness dependent piezoelectricity characteristic in 2D wurtzite ZnO on substrate of α-SiO$_2$. 2D ZnO with 2.5 unit-cell (~1.1 nm) thick demonstrated a maximum d_{33} values of 80 ± 0.8 pm/V, and that is roughly 8 times higher than that of crystalline ZnO crystal (Figure 4g). This phenomenon is different from that in TMDs such as MoS$_2$, which exhibited maximum piezoelectricity for monolayer structure.[85] The DFT study revealed that the highest d_{33} value of ~1.1 nm thick ZnO was the result of trade-off between the thickness effect of ZnO and its interaction with the substrate.

2D metal oxide exhibits great potential in discovering new atomically thin high-T_c superconductors. In previous studies, the superconductors, as in the case of metallic lead and indium thin film, have demonstrated a lower T_c with thickness down to 2D limit.[86-88] For instance, the lead thin film exhibits a T_c value of 4.9 K (2-ML thick) and 6.7 K (4-ML thick), which is thought to be related to film-substrate interactions.[87] However, as shown in Figure 4h, 2D superconductor Bi-2212 monolayer (half unit-cell) exhibits a T_c value of 88 K, which is almost as high as that of the bulk counterparts. Besides, the high crystallinity Bi-2212 monolayer can be easily obtained by mechanical exfoliation, which will provide more opportunities for development of new fabrication technologies for high-T_c 2D superconductors.

Reducing the thickness of metal oxide can expose more metal ions to the surface, thus charge transfer and valence change could take place in the materials, which can possibly modulate the magnetic property. Balan et al. has successfully produced the 2D ilmenene from the bulk titanate ore ilmenite (FeTiO$_3$) by liquid phase exfoliation.[89] As shown in Figure 4i, 2D ilmenene shows an enhancement of coercivity and remanent magnetization compared to the paramagnetic bulk ilmenite, indicating a weak ferromagnetic ordering of 2D ilmenene at room temperature. The ferromagnetic behavior can be attributed to anisotropy due to surface spins.[90] In addition, the

WILEY-VCH

charge transfer excitation from $Fe^{2+}Ti^{4+}$ to $Fe^{3+}Ti^{3+}$ may occur on the surface of 2D ilmenene, where $Fe^{3+}Ti^{3+}$ favors the ferromagnetic state. $BiFeO_3$ thin film exhibits a thickness-dependent magnetic moment.[91] At magnetic field of 15 KOe, $BiFeO_3$ film with 30-nm-thick and 120-nm-thick shows a magnetic moment of ~ 70 and 20 emu cm^{-3}, respectively. The high magnetic moment in thinner film probably originates from the high concentration of Fe^{2+} due to the presence of oxygen vacancies. Despite the lack of further research, these works offer a glimpse into the possibility of studying thickness dependent magnetic properties of 2D metal oxides.

 Besides, one existing limitation of bulk metal oxide is that it is brittle upon bending. Reducing the metal oxide thickness to only a few atoms is recognized to significantly increase the flexibility,[92] allowing the potential application in flexible devices.

3. Advances in synthesis strategies of 2D metal oxides

The controllable synthesis of 2D metal oxide with expected structure (composition, phase, defects, *etc*.), morphology (size, thickness, *etc*.) and surface property is the prerequisite for studying their chemo-physical properties and potential applications. Typically, mechanical exfoliation, namely scotch tape method, has been widely adopted for peeling off ultrathin 2D material from the layered bulk counterpart.[93-94] Some layered 2D metal oxides, like MoO_3,[95] WO_3,[96] can be prepared by mechanical exfoliation owing to the weak vdW interaction between adjacent layers. While, non-layered Ga_2O_3 thin films also could be mechanically exfoliated from bulk crystals, which is correlated to the large lattice constant along the [100] direction (12.336 A˚) [97] Beside the mechanical exfoliation, many efforts have been made on looking for efficient and reliable method to prepare high-quality ultrathin 2D metal oxide, even for metal oxide monolayers. Thus far, lots of methods have been successfully developed, including solution-processed synthesis, vapor phase deposition (the space-confined growth method), liquid metal printing, metal-gas interface, native oxide on 2D metal chalcogenides. Here we offer a summary of these methods, elaborating on the working principles and progress, as well as strengths and weaknesses.

3.1. Solution process

To control the 2D morphology of metal oxides, the general idea in bottom-up strategy comes from the crystallization and growth of metal oxide on the ultra-flat templates. Thus, the key becomes how to construct a proper hyperflat surface or so-called interface.

The first technique is to introduce structure directing agent or capping agents (surfactants) as a soft template to determine the in-plane crystal growth.[98] The soft templates are generally constructed using ionic surfactants (e.g. sodium oleylsulfate) and non-ionic surfactants (e.g. amphiphilic block copolymer polymers, P123). The surfactant ions or molecules are preferentially adsorbed on the specific facet of the crystal nuclear to inhibit the growth along the direction of this crystal facet, guiding the formation of 2D structure.[99] The ionic surfactant will strongly bond with the products, which can be hardly removed by washing. In general, two working modes for these soft templates have been developed in 2D metal oxide synthesis, which are surfactant monolayer at the water-air interface and lamella of surfactant bilayers in the solution.

Adaptive ionic layer epitaxy method (AILE) is a typical water-air interface method for 2D nanosheets synthesis. In a typical process, the ionic surfactant is dissolved in the water to form a close-paced monolayer at the interface of water and air. The ionic monolayer acts as a soft template, of which the packing density adapts to attract metal cations to form supersaturated region near the solution surface to promote the crystallization and guides the epitaxial growth of nanosheets (**Figure 5**a). In 2016, Wang and co-workers synthesized nanometer-thick single-crystalline ZnO nanosheets through AILE.[100] In their work, the Sodium oleylsulfate (SOS) is selected to form ionic monolayer to attract Zn^{2+} ions to form supersaturated region at the interface of water and air, resulting in the initial formation of a continuous amorphous films. Later, nanocrystals evolve from amorphous film and further merge into larger crystalline 2D nanosheets through self-alignment. The as-synthesized 2D ZnO nanosheets demonstrate wurtzite structure in triangular shape with side length of tens of micrometer and thickness of 1-2 nm. This long-range self-alignment is originated from the synergistic effect of strong association between the ionic headgroups and the metal cations below and the vdW interaction among the hydrocarbon tails. Meanwhile, the local packing density of the ionic monolayer can spontaneously adapt to the nanosheet lattice during the crystal growth. Thus, an appropriate selection of ionic surfactant is crucial to the 2D growth of a certain material. Yu et al.[35] has demonstrated that using sodium dodecyl sulfate (SDS) instead of SOS for 2D ZnO synthesis can significantly improve the crystallinity and reduce the residual contamination. By selecting suitable ionic surfactant, the ionic layer epitaxy approach can be utilized in other 2D materials synthesis, such as 2D NiO, Au, and Pd nanosheets.[100-101] Notably, the oleysulfate monolayer will cap on one side of the as-synthesized 2D ZnO, which causes an unusual p-type semiconducting behavior. If necessary, the ionic surfactant can be removed by further treatment (*e.g.*, thermal or UV ozone treatment). Moreover, it should be noted that the 2D metal oxide nanosheets are only formed in the water-air interface while the chunky nanocrystals are still formed in the bulk solution. Some other surfactants,

WILEY-VCH

like oleylamine, has been reported to assist 2D cobalt oxide and cobalt nickel oxide nanosheets formation through guiding a 3D-to-2D transition (nanocrystal-to-nanosheet transition) in the solution. The driving forces of 3D-to-2D transitions are associated to the competition between the negative surface energy and the positive edge energy, which are arising from the intrinsic material properties.[102]

Different from surfactant monolayer templating growth, the lamella of surfactant bilayers templating growth are generally performed using surfactant lamellar micelles to confine the 2D materials growth.[103-104] On the basis of the molecular packing theory, some hydrocarbon amphiphiles can self-assemble into lamellar micelles that are composed of planar bilayer in which part of the amphiphilic molecule faces toward the solvent and another part locates inside the bilayer.[105] In a typical synthesis route, as shown in Figure 5b, the reactant precursor is firstly introduced into the planar lamellar micelles constructed by the surfactant. Then the confined crystallization takes place under the hydrothermal or solvothermal condition. Finally, fine products of 2D metal oxide nanosheet are obtained after removing the surfactant templates. In 2014, Kim et al.[106] has successfully synthesized various nanosheets of 2D metal oxide in an ethanol solution with inverse lamellar micelles which is constructed by polyethylene oxide-polypropylene oxide-polyethylene oxide (P123) surfactant together with ethylene glycol (EG) co-surfactant. The hydrated metal source precursors were confined inside the inverse lamellar micelles as oligomers. Further solvothermal treatment was conducted to promote the assembly of the oligomers and formation of 2D metal oxide due to the confinement effect of the lamellar surfactant bilayer. The as-synthesized ZnO, Co_3O_4, and WO_3 nanosheets possess the lateral size of 1-10 μm while the TiO_2 nanosheets are much smaller (~200 nm). The thicknesses of the metal oxide nanosheets distribute in the range of 1.6 to 5.2 nm which is equal to 2 to 7 stacking layers. In this method, the addition and ratio of P123/EG/water is the key to form 2D morphology of metal oxide. P123 as surfactant can be adsorbed on the surface of oligomers to prevent agglomeration, while the EG molecules as co-surfactant and co-solvent can effectively stabilize the lamellar structure to confine the growth of ultrathin 2D architecture. Controlled experiments reveal that 2D morphology cannot be obtained without P123 or EG, or with large excess of water.

In comparison to the ionic surfactant monolayer templating method, the nonionic surfactant can be easily removed by solvent extraction. Also, larger particles are not easy to be precipitated from lamellar solution since the diffusion of the metal ions is slower than the nucleation. The raw 2D metal oxide without organic shell capping can present intrinsic semiconducting properties and well-

contact with electrodes in the process of device fabrication and integration. Moreover, the surfactants in colloid chemistry have been extensively exploited for over a century, which can provide plenty of planar templates for the preparation of 2D metal oxide nanosheets. Despite considerable advancements, the surfactant bilayer templating method still suffers from the following disadvantages. Firstly, the optimized experimental conditions are difficult to be controlled due to the uncertain effects of introducing metal source. For instance, some metal source may break the lamellar structure of the surfactant or have poor solubility in ternary mixture with nonionic surfactant, which may lead to the failure of the template and the precipitation of bulk metal oxide. In addition, the confined growth along the soft templates will generate a curvature in the crystal lattice, resulting in a significant increase of the defect in the final products.

The second technique is to introduce hard templates with atomically flat hydrophilic surface which can attract the crystallization of metal oxides. Graphene features atomically flat but chemically inert which hinders its role as a template material in wet chemistry. The oxidized derivation namely graphene oxide (GO) can endow graphene with active functional groups, such as hydroxyl and carboxyl groups, which makes GO nanosheets as promising templates for the nucleation and growth of nanomaterials.[107] The typical process has three steps as shown in Figure 5c. Firstly, the metal ions and GO were well-mixed in the solution to form a homogeneous dispersion. The metal cations with positive charge diffused and anchored on the negatively charged GO surface due to the electrostatic attraction. Then, the dispersion was heated up to accelerate the hydrolysis of metal ions on the surface of GO to form a thin precursor coating on the basis of LaMer's law.[108]. Finally, thermal treatment at high temperature was conducted to remove the GO template, resulting in ultrathin 2D metal oxide nanosheets.

In 2017, Zhao et al.[109] has prepared six metal oxide nanosheets (MgO, ZrO$_2$, Al$_2$O$_3$, TiO$_2$, SnO$_2$, and Sb$_2$O$_5$) with lateral size up to 50 μm by using sacrificial GO templates. The ultrathin nanosheets exhibit typical ripples and wrinkles that appear in solution synthesis, of which thickness vary in the range from 2.1 nm to 4.7 nm. To avoid the formation of independent large precipitates in the bulk solution, the hydrolysis process needs to be suppressed before the metal ions are adsorbed to the GO surface, which can be achieved by appropriate configuration of metal ion concentration, pH and temperature. To obtain the uniform 2D nanosheets, the key is the balance between heterogeneous growth and nucleation of metal ions on the GO surface during hydrolysis, which requires a stable pH of the system. Thus, a buffer solution is necessary to accurately control pH during the synthesis. As the metal oxides are restricted to grow on the GO templates, the lateral size of as-synthesized metal

oxide nanosheet is determined by the size of the sacrificial GO templates. Besides, thickness of the 2D nanosheets can be tuned by varying the concentration of the metal salts in the solutions.

To achieve thinner 2D metal oxide, Yao's group further modified this strategy to confine the crystallization of metal ions in the vdW gaps between the adjacent layers of GO by thermal treatment in inert atmosphere, instead of hydrolysis in the solution.[54] Briefly, the zinc acetate dihydrate precursor solution initially intercalates and diffuses into the GO templates on a substrate through immersion. Then, the metal ions weakly adsorbed on the outer surface of GO are rinsed off while the metal ions confined in the GO interlayer gaps crystallize to form ZnO/rGO composite after thermal treatment in inert atmosphere. The 2D ZnO nanosheets are obtained after removal of rGO by further calcination in air, which exhibit structure of graphitic layered phase gZnO with thicknesses down to a monolayer (thickness of 0.28 nm) and sizes up to 20 μm. In 2021, they introduced heteroatom doping conception to synthesize single-atom-thick cobalt-doped gZnO (gZCO) using a mixture solution precursor of zinc acetate and cobalt acetate. The 2D gZCO exhibited tunable ferromagnetism at room temperature by changing the doping level of magnetic Co atoms.[38]

As shown in Figure 5d, the single crystal of salt also features the atomically flat ionic surface, which has been used in synthesis of 2D metal oxide,[110] or other 2D materials.[111] The common procedure consists of three steps: (i) coating a metal ion precursor solution on the salt template; (ii) 2D metal oxide formation on the salt template through heating treatment under controlled environment; (iii) isolation of 2D metal oxide by washing out the salt template with water. Xiao et al. produced various transition metal oxides (h-MoO_3, MoO_2, h-WO_3 and MnO) with the surfaces of water-soluble salt (NaCl or KCl) crystals as the growth templates. The as-synthesized 2D metal oxide nanosheet exhibited a large lateral size up to 100 μm and thickness down to < 2 nm.[110] In this method, the dilute alcoholic solution of metal source was selected as molecular precursor to prevent the nucleation before coating on the salt. Then, limited volume of precursor was mixed with a large amount of salt to achieve the mixture of ultrathin precursor coated salt, in which ultrathin coating can avoid the formation of structurally stable nanocubes. Lastly, the crystallized metal oxide should possess an identical crystal geometry with the salt template to promote Frank–van der Merwe mode growth and heteroepitaxy.[112] Otherwise, only non-2D particles will be obtained due to the large lattice mismatch.[113] The biggest advantage of salt templating method is that the removal of the template is green, convenient and complete, as the ionic salt is easily soluble in water, whereas GO and organic surfactant require treatment with high temperatures or organic solvents. In addition, the thickness of 2D metal oxide can be easily tuned by changing precursor-to-salt ratio since lower

precursor-to-salt ratio will give a thinner precursor coating on the salt template which generally result in thinner 2D metal oxide products. Meanwhile, the lateral size of 2D metal oxide can be regulated by controlling the surface size of the salt.

Liquid exfoliation of layered materials is a general top-down way for 2D materials preparation. The bulk layered materials in solution can be exfoliated into ultrathin sheets with the assist of mechanical sonication, ion intercalation and exchange, and electrochemical methods.[114] Diverse layered 2D metal oxides have been attained by mechanical sonication method, such as MoO_3,[115] WO_3,[116] RuO_2,[117] etc. The small ions or molecules can be introduced as intercalant to weaken the interlayer association in layered materials to facilitate the exfoliation. For some atypical layered oxides with strong interlayer ionic bonds, ion exchange pretreatment is essential for further liquid exfoliation. As shown in Figure 5e, Fang's group reported stable and nontoxic 2D perovskite-type oxide $Sr_2Nb_3O_{10}$ (SNO) nanosheets with thickness down to 1.8 nm (monolayer) by liquid exfoliation.[118] In a typical process, the bulk materials of Dion-Jacobson layered oxide was firstly conducted an ion-exchange with proton to kick out the interlayer Cs^+ cations to form $HSr_2Nb_3O_{10}$ (HSNO), followed by exfoliation in tetrabutylammonium (TBAOH) solution. The TBA^+ cations can intercalate into the interlayer gaps of HSNO, of which alkyl group can weaken the interlayer association to promote exfoliation process. Ultrathin 2D SNO nanosheets will be harvested after the removal of TBA^+ under UV, which feature the thickness from 1.8 to16 nm and median lateral size of 0.9 μm. Similarly, other 2D perovskite-type metal oxides have been synthesized, such as $Ca_2Nb_3O_{10}$,[45] $Ca_2Nb_{3-x}Ta_xO_{10}$.[119] Although the liquid exfoliation often suffers from chemical residues, broad thickness distribution and relatively small lateral size, it is still a promising method in scale-up synthesis of 2D metal oxide for large-area electronic or optoelectronic device.

3.2. Vapor phase deposition

The vapor phase deposition is a general thin film preparation technique for metal oxides, which can also be used for single crystal nanomaterial growth. Generally, it can be separated into two categories: physical vapor deposition (PVD) and chemical vapor deposition (CVD).

In PVD process, using a physical process (typically heating or bombardment), source materials can be transformed into a vapor or plasma. Then the vapor moves towards a substrate and condenses on the surface to form solid product. As shown in **Figure 6a**, PVD technique has various subdivisions, such as sputtering, thermal evaporation, molecular beam epitaxy (MBE) and pulsed laser deposition

WILEY-VCH

(PLD). For example, in PLD, a high-power density and narrow frequency bandwidth laser is adopted as a source to vaporize the desired material. It can successfully deposit ultrathin oxide films, such as ZnO[120], $SrTiO_3$ and $La_{0.7}Sr_{0.3}MnO_3$,[121] The 2D perovskite oxide with a few unit-cell thick was epitaxially grown on the water-soluble $Sr_3Al_2O_6$ on perovskite substrate by PLD method.[121] Single-crystalline membranes with lateral size up to millimeter can be isolated by etching the $Sr_3Al_2O_6$ layer in water, and can be transferred to arbitrary substrates and integrated with heterostructures of layered compounds and semiconductors.[122] MBE is a highly effective approach to grow homogeneous film on desired substrates with controlled thickness and structural precision at the unit-cell level. For example, MBE has been used in single crystal 2D metal oxide,[55] and perovskite oxide with a few unit-cell (u.c.) thick, such as 2 u.c. thick $LaNiO_3$,[123] 1 u.c. thick $SrTiO_3$ and $BiFeO_3$.[44]

Unlike the high vacuum environment in physical vapor deposition mentioned above, the physical vapor transport (PVT) approach usually needs a carrier gas to bring the gaseous metal oxide to the substrate at downstream for epitaxial growth. The passivator can be introduced into the system to confine the thickness of 2D metal oxide (Figure 6b). Liao et al.[124] synthesized freestanding single crystal high-κ Al_2O_3 nanoribbons through a physical vapor transport approach at high temperature. The thickness of Al_2O_3 nanoribbons typically vary from 15 to 150 nm, and have almost atomically smooth surface with small root mean square roughness. 2D Sb_2O_3 can be prepared as thin as 0.64 nm by PVT approach with the help of passivator Se.[43]

In CVD process, gaseous materials will react in the vapor phase or on the surface of substrate to condense into solid products. The texture of the products including thickness, size, morphology and even introduction of defects or dopants can be tuned by modulating the growth condition such as carrier gas flow rate, pressure, temperature, ratio of the reactants, and source-substrate distance. Based on the characteristics of the preparation method, CVD technique has various subdivisions, such as atomic layer deposition (ALD), metal-organic chemical vapor deposition (MOCVD), low pressure chemical vapor deposition (LPCVD) and plasma enhanced chemical vapor deposition (PECVD).

ALD is a technique based on the sequential use of a gas-phase chemical process. The reactions in metal oxide thin films use two chemicals: organometallic compound as metal precursor and water or ozone as oxygen precursor. The precursors will react with the surface of a material once at a time in a self-limiting and sequential manner, which can even achieve sub-nanometer film deposition (Figure 6c). Hai et al. reported a monolayer WO_3 with thickness of 0.71 nm by ALD method.[125] Si et al. deposited amorphous In_2O_3 film with 0.7 nm thickness by ALD. The as-fabricated In_2O_3-channel

FETs exhibited n-type enhancement-mode semiconducting behavior.[24] Further scaling of the In_2O_3 channel into 0.5 nm-thick has been demonstrated in another work.[23]

CVD with horizontal tube reactor is the most common configuration, where the substrates are exposed to the volatile precursors to allow materials or thin film growth under a controlled gas flow. Wu et al. demonstrated that 2D metastable γ-Bi_2O_3 flakes with non-layered structure could be synthesized by vdW epitaxy method in CVD (also called chemical vapor transport, CVT) setup as shown in Figure 6d. The low melting point Bi powders was used as the precursor. 2D ultrathin metastable γ-Bi_2O_3 flakes can be attained under atmosphere pressure on mica substrate at 680 °C with an Ar flow of 100 sccm. Metal salt also has been used as metal precursor in growth of 2D Fe_2O_3 crystal,[126] and Sb_2O_3 crystal.[43] Yin et al. prepared high-quality nonlayered 2D Fe_3O_4 nanosheets by space-confined CVD.[36] Briefly, Fe foil as metal source was sandwiched between two vertically stacked flurophlogopite mica, resulting in a slight gap size for space confinement. The small gap provided a local microreactor with a very low precursor density and restrained the growth along the out-of-plane direction. Meanwhile, a low melting point materials (BiI_3) was adopted as the surface passivator to get the non-layered 2D Fe_3O_4 nanosheets since the preferential adsorption of iodine on the (111) plane of Fe_3O_4 can suppress the isotropic growth along 3D directions.[127] The 2D Fe_3O_4 exhibits crystalline morphology with lateral size of ~5 μm and thickness down to 1.95 nm.

3.3. Native oxidation on metal source

The *in-situ* formation of oxide on the flat metal source is a fascinating idea for 2D metal oxide growth. The 2D metal oxide can be formed by oxygen oxidation of metal and oxygen ion exchange with anion in the metal source, in which the atomically flat surface of metal source can provide self-template. Several metal sources have been demonstrated for 2D metal oxides growth, including metal in liquid phase or solid phase and 2D layered metal chalcogenides.

Most metals feature an ultrathin skin layer of self-limiting thin oxide which is natural 2D metal oxide at metal-air interface in ambient condition. The formation process of the oxide skin has been explained by Cabrera-Mott oxidation model,[128] which involves the initial oxygen chemisorption on the surface of metal, followed by subsurface oxygen-metal bonding, and finally formation of oxide lattice on surface of metal substrate.[129] This model suggests that an uniform 2D oxide layer is possible to be obtained by precisely controlling the homogeneous adsorption and penetration depth of oxygen atoms on a flat metal surface. Inspired by this idea, two synthesized strategies have been

WILEY-VCH

developed: (1) oxidation on the liquid metal surface; (2) oxidation on the surface of polished flat solid metal.

Liquid metals are referred to metals and metal alloys which are in liquid state in their practical application environment (usually at temperature below 300 ℃), which has been widely used in catalysis, synthesis, microfluidics, sensing and soft electronics.[130] Recently, the liquid metals has demonstrated their great potential in synthesizing 2D metal oxide since the self-limiting thin oxide layer on the surface is considered as perfect 2D planar material.[131-132] Moreover, thanks to the weak interfacial force, it is quite easy to achieve the isolation of the surface oxide from the bulk phase of liquid metal.

In 2017, Zavabeti et al.[133] investigated the preparation of a series of 2D metal oxide nanosheet using liquid alloy. They proposed two major methods which are so-called air injection into liquid metal and liquid metal printing technique (**Figure 7a-b**). Air bubble injection method is preferred when the free-standing 2D metal oxide is required, while the liquid metal printing method is usually conducted to place the 2D metal oxide on the desired substrates. The liquid metal printing method can bring 2D metal oxide into large lateral size or even wafer scale, which benefits the electronic device fabrication. Notably, it is possible to get the amorphous 2D metal oxide nanosheets if the time for oxidation reaction is not enough for certain metal oxide. To get pure 2D metal oxide, it is essential to concern the issue of multi-component metal oxides[134] and co-existence of metal oxides in multi-valence states[135] on the liquid alloy surface during the synthesis. Thus, the oxidation condition needs to be carefully optimized, as well as the concentration of desired metal in the alloy.

Interestingly, the metal oxide skin on the liquid metal alloy surface is preferentially evolved from most reactive metal element, instead of all alloying elements. In other words, the oxide with lowest Gibbs free energy change for oxide formation (ΔG_f) can be selectively obtained by alloying its counterpart metal element into liquid metal. Based on this principle, diverse 2D metal oxides including Ga_2O_3 (2.8 nm), HfO_2 (0.6 nm), Al_2O_3 (1.1 nm), and Gd_2O_3 (0.5 nm) can be selectively formed and isolated from the surface of Galinstan or their metallic counterpart precursors alloyed with Galinstan, respectively.[133]

Besides the liquid metal alloy, the pure liquid metals were also used in 2D metal oxide synthesis, such as Sn metal,[41] In metal,[136] Zn metal,[37] *etc*., while the operation temperature should be higher than their melting point. After a few years development, various isolation method has been developed, including touch printing,[133] squeeze printing,[29, 137] blade printing[138-139] liquid phase

WILEY-VCH

sonication[140] and air bubble injection.[133-134, 141] Various thin oxide sheets were obtained by utilizing the liquid metal skin, such as MnO_2[142], a-Ga_2O_3,[143-144] Bi_2O_3,[145] SnO,[146] SnO_2,[41] ZnO,[37] TiO_2,[134] ITO,[29] IZO and In_2O_3,[69] Sb_2O_3,[147] and TeO_2.[139]

Controllable oxidation of the polished metallic surface has been reported to enable the growing of vdW layered metal oxides. The mechanical exfoliation of bulk 2D layered materials is an universal method for 2D materials preparation.[94] 'Stamping' such layered metal oxides covered polished metal surface onto a substrate can exfoliate off the 2D sheets. Schematic illustration of material growth and mechanical exfoliation approach is shown in Figure 7c-d.

Recently, Zhang et al.[32] reported a series of 2D layered hexagonal metal oxide growth on the metal-gas interface. The 2D layered oxides are prepared by in-situ oxidation of ultrafine polished metallic surface under precisely controlled condition. The atmosphere and temperature of oxidation process are arranged based on the chemisorption energy (E_c) of corresponding metal, aiming to achieve a mild and undisturbed oxidation process for 2D metal oxide growth. Specifically, in the temperature range 200-300 °C, oxygen concentrations need to be strictly controlled under ppm-level in the cases of Co, Ni, Cu and Gd, or even under ppt-level in the cases of Ti, Mn, Fe, Al and Ge. This method is widely applicable for preparing various fully stoichiometric metal oxides monolayer including transition metal oxides (TiO_2 (~0.55 nm), MnO (~0.65 nm), Fe_2O_3 (~0.64 nm), CoO (~0.84 nm), Ni_2O_3 (~0.71 nm) and Cu_2O (~0.42 nm)), post-transition metal oxide (Al_2O_3 (~0.62 nm)), metalloid oxide (GeO_2 (~0.51 nm)) and lanthanide oxide (Gd_2O_3 (~0.71 nm)). The extremely slow oxidation process favors the formation of the honeycomb-like planar hexagonal crystal coordination to minimize surface energy. On the contrary, the high oxygen concentration and temperature will turn the 2D layered oxides into non-layered bulk phase. For instance, the conventional non-layered anatase phase can be obtained after annealing the h-TiO_2 in ambient environment beyond 400 °C. In their work, the h-TiO_2 exhibited exciting p-type transport behavior with the hole mobility up to 950 cm^2 V^{-1} s^{-1}. The structures and properties of other 2D metal oxides are also interesting but still blank.

2D materials, mostly 2D metal chalcogenides, are natural precursors or templates for 2D metal oxides synthesis under a controlled oxygen environment. In a typical process, the oxygen will diffuse into the 2D parent materials and replace the anions to form 2D oxides, resulting in no significant change in the geometry of parent materials (Figure 7e-f). In wet chemical process, the oxygen exchange can be carried out in the oxidative solution, for example, Azam et al. conducted the aggressive oxidation of 2D WS_2 in nitric acid solution for 2D crystalline WO_3 synthesis.[148] For dry chemical process, the oxidation of 2D templates can be performed under thermal treatment,[149]

WILEY-VCH

intense laser illumination,[150] upon exposure to oxygen plasma[151] or ozone[152], and combination of above technique as well.[153-154] Depending on the conditions of the oxidation reaction and the crystalline properties of the oxide, it is possible to generate amorphous, polycrystalline or even single-crystalline 2D oxides. Feng et al. synthesized 2D β-Ga_2O_3 polycrystalline nanosheets by thermal oxidation of 2D GaSe nanosheets under atmospheric conditions.[155] In particular, single crystal bismuth selenite (Bi_2SeO_5) could be conformally synthesized via layer-by-layer oxidation of 2D Bi_2O_2Se under thermal annealing in air.[156-157] However, under oxygen plasma treatment at room temperature, 2D Bi_2O_2Se will be oxidized into the amorphous non-stoichiometric form, namely Bi_2SeO_x.[158]

Sometimes, the partial oxidation on the 2D metal chalcogenides is very interesting for creating 2D metal oxide/metal chalcogenides heterostructure, which can extend or enforce the functionalities of 2D materials. With rapid oxidation process at low temperature, the as-prepared metal oxide usually features atomically smooth amorphous materials, of which thickness is controlled by depth of oxidation and limited by the thickness of 2D TMDs. Pang et al. conducted a controllable O_2-plasma treatment on WSe_2 at desired temperature, during which 3 layers of WSe_2 can be converted into ultrathin amorphous WO_{3-x} to form oxide/WSe_2 heterostructure, which can tune the charge transport behavior in the channel.[153] Moreover, the 2D native oxide HfO_2 on 2D HfS_2 can be used as dielectric for clean interface in 2D based transistor.[159] It seems that the native oxide methods usually yields 2D oxides, except severe oxide conditions (such as extremely high temperatures) are used.

3.4. Comparison of preparation methods

Although the major characteristics of the synthesis methods have been introduced separately in above sections, a centralized overall discussion has significance for better understanding of these synthesis methods. Here we compare the above-mentioned synthesis methods (**Table 2**) of 2D metal oxides in terms of the material defect density, general size, surface cleanliness, thickness control, substrate requirements, production efficiency, and oxide types applicable to preparation method.

The defect density has a great impact on the properties of 2D metal oxide, which is one of the most important indicators to evaluate the quality of 2D metal oxides. Generally, the mechanical exfoliation method can obtain an almost perfect single crystal of layered 2D metal oxide to achieve intrinsic performance of the material. Vapor phase methods usually can prepare high crystalline materials with low defect density, but ALD method often gives low crystallinity which may be

attributed to the sequential growth mode and substrate effect. In most cases, 2D metal oxides that prepared by native oxide strategy are highly defective due to the lattice mismatching between native oxide and source material during the oxidation conversion.

Large lateral size of 2D metal oxides can provide benefits to the device fabrication and integration. Currently, some vapor deposition methods can achieve wafer scale preparation of ultrathin amorphous metal oxide (e.g., ALD) and crystalline 2D metal oxide (e.g., MBE). CVD methods can successfully prepare the wafer scale single crystal 2D materials like graphene, hBN, MoS_2,[19] but only realize micrometer-scale for thin crystalline 2D metal oxide growth. The reason of lateral size limitation is that unsaturated dangling bonds on the surface of metal oxide promote isotropic growth along 3D directions. To a certain extent, the passivator like BiI_3 can help to suppress the out-plane growth, however, it cannot keep the metal oxide in a very thin level when the crystal continues to grow. The lateral size of the materials synthesized by template-assist solution process are highly depended on the template sizes.

A clean surface is an important guarantee for forming a good interface in device preparation and integration, which has great influence on the device performance. The solvent-free methods like mechanical exfoliation, CVD, and MBE perform quite well. However, sometimes 2D metal oxides involve transfer steps, which may lead to interface contamination. Native oxide strategy has great advantages in providing super clean interface in specific application scenarios (e.g., in-situ formation of dielectric layer).

Thickness has significant impact on the properties of 2D metal oxides. In terms of thickness control, the vapor phase methods perform high accuracy and repeatability in a wide range of thickness. Although template-assist solution process can tune the products thickness by adjusting the reaction precursor and conditions, these uncertain factors may lead to the failure of 2D metal oxides formation.

The mechanical exfoliation and liquid metal printing (using low melting point metal or alloy) does not have strict requirements on the substrate, which can easily transfer the 2D metal oxide on various substrate. The liquid metal printing using high melting point (e.g., > 400 °Cfor Zn) is not suitable for direct printing on the polymer substrate. The vapor phase methods, especially MBE, require growth on a specific substrate which may be selectively etched for subsequent material transfer. On the contrary, the liquid phase methods usually do not require a substrate during the preparation process, and the as-synthesized samples can be easily coated on any substrate.

WILEY-VCH

Liquid phase methods generally have the high production efficiency and low cost for synthesizing various 2D metal oxide nanosheets, which is promising for large-scale industrial production. Liquid metal printing also has great potential for large area 2D metal oxides production while the precursor is preferably a low melting point metal or alloy. The methods that require specific environment and instrument have relative lower efficiency and higher cost. For instance, metal-air interface method generally requires ultra-flat polished metal surface and restrict environment (oxygen concentration down to ppt-level).

In terms of the scope of application, the top-down methods (e.g., mechanical and liquid phase exfoliation) are only suitable for the layered materials with weak interlayer vdW forces. The bottom-up methods can theoretically grow all kinds of 2D metal oxides, but have various practical obstacles. For instance, liquid metal printing is not suitable for using high melting point metal. Native oxide strategy highly relies on the 2D metal source materials. For the oxides with complex compositions like layered perovskites, it seems difficult to imagine such materials arising from controlled oxidation of a metal alloy by liquid metal printing and metal-air interface method.

4. Application of 2D metal oxides

2D metal oxides can not only inherit some interesting features of their bulk counterparts, but also exhibit unprecedent characteristics that arise from the quantum confinement and structure modification (e.g., novel structures, defects engineering). The fascinating features endow 2D metal oxides with diverse functionalities, such as insulating, semiconducting, superconducting, and magnetic properties. Besides, the heterostrucutre based on 2D metal oxides can further extend the functionalities, including, for example, 2D electron/hole gas, interficial supercondutor, and interfical magnets. Thus, 2D metal oxides have attracted extensive research interest in various electronic and optoeletronic devices and systems. In this section, the applications of 2D metal oxides, including field-effect transistors and logic circuit, photodetectors, piezotronics/piezo-phototronics, memristors, and potential device applications (e.g., solar cell, spintronics, superconducting devices) are introduced.

4.1. 2D FET and circuit

The continuous miniaturization of FETs can enable the large-scale integration of FETs into a single chip with much improved performance and reduced cost. 2D semiconductors have attracted

enormous interest since atomically thin channels can reach to the scaling limit of the transistor. Although tremendous and remarkable progress has been made, there are many challenges in 2D FETs that need to be overcame. For instance, requirement of stable channel materials with high hole mobility, high-κ dielectric with good quality and interface, metal/2D contact with low contact resistance, *etc*. Bringing 2D metal oxide into 2D FET studies could be a promising way to solve some current problems. Recent progress has revealed that 2D metal oxide can be as semiconducting channel materials, high-κ dielectrics and other functional layers in 2D devices.

4.1.1. Semiconducting channel materials

FET is a semiconductor device that uses input voltage signals to modulate the charge transport in the semiconducting channel *via* a capacitive structure. It is composed of an insulator inserted between the semiconductor and the conducting gate electrode, source and drain electrodes which contacts with semiconductor. The current is injected from the source across the semiconductor and collected by drain with on and off stages under a gate voltage bias, which scales as the carrier density multiplied by the carrier mobility (μ). The μ, on/off current ratio, threshold voltage (V_T) are significant performance metrics for FET. For a simple 2D FET fabrication, the 2D materials are usually transferred onto a silicon wafer with native thermal oxide, in which heavy-doped Si works as gate and SiO_2 layer works as dielectric insulator. Then, the drain-source electrodes are defined by vapor-phase deposition with the assistance of electron beam lithography (EBL) or photolithography. In this section, recent progresses of FET based on 2D oxides are summarized, including n-type FET, p-type FET and their derived circuit (**Figure 8**a).

To study the doping effects on 2D metal oxides FET, recently, a series of n-type FET have been demonstrated using 2D In_2O_3 and 2D Zn-doped In_2O_3 (IZO) as channel materials, where the 2D channel is fabricated by liquid metal printing method.[69] The 2D IZO possess a high crystallinity with single unit-cell thickness (~1.6 nm) (Figure 8b). The FET based on 2D low-level Zn-doped IZO exhibits excellent electron mobility of ~87 cm^2 V^{-1} s^{-1} with a considerable on/off ratio of 10^5, while the mobility of In_2O_3 significantly decreases to ~4 cm^2 V^{-1} s^{-1} with a similar on/off ratio (Figure 8c-d). Moreover, the further increase of Zn content will set the FET in the "on" state with a slightly lower mobility of ~18 cm^2 V^{-1} s^{-1}, emphasizing the importance of optimizing doping level.

Nevertheless, the development of p-type oxides can significantly promote the progress in oxide electronics, enabling p-n junction for complex circuit, and improving ohmic contact for high efficient photovoltaics.[66] Recently, Zhang et al.[32] reported a back-gated FETs device based on a novel 2D h-TiO$_2$ with 0.5 nm channel thickness (Figure 8e). The I_{ds}-V_{gs} characteristics has shown a typical p-type transport behavior (Figure 8f). Moreover, the FETs based on 2D h-TiO$_2$ demonstrates a thickness-dependent hole mobilities which are various from ~10 cm^2 V^{-1} s^{-1} for a 0.5-nm-thick channel up to 950 cm^2 V^{-1} s^{-1} for a 5-nm-thick channel (Figure 8g). This remarkable value (950 cm^2 V^{-1} s^{-1}) is almost six orders of magnitude higher than the previously reported p-type TiO$_2$,[160] also significantly exceed those reports for p-type metal oxide semiconductors, even comparable with the novel 2D materials (black phosphorus,[161] WSe$_2$,[162] etc.). 2D ZnO nanosheets with 1 to 2 nm thickness were prepared by sodium oleylsulfate assisted water-air interface synthesis. The ZnO nanosheet based FET properties were further investigated with bottom gate top contact configuration. The device was fabricated by directly scooping the 2D ZnO nanosheet onto 50 nm Al$_2$O$_3$/Si silicon wafer with pre-patterned drain-source electrodes. The I-V curve showed a typical p-type semiconductor behavior. The hole mobility and carrier concentration of the nanosheets were estimated to be 0.10 cm^2 V^{-1} s^{-1} and 4.5×10^{12} cm^{-2}, respectively. The surface adsorbed molecules (SDS) have been assumed to be the key factor that causes the nanometer-thin 2D ZnO to have p-type conductivity, while it also leads to poor nanosheet-electrode -contact-, resulting in low mobility. Recently, some conventional p-type metal oxides have been scaled down to nanometer or sub-nanometer thin. The 2D SnO has been successfully grown on SiO$_2$ and sapphire wafer using a PLD method,[163] which could be utilized as the FET channel, featuring an ascending hole mobility from ~0.05 to 1.9 cm^2 V^{-1} s^{-1} with increased number of channel layers from 5 to 12-layers. The recent report of FETs with 2D metal oxides as channel layer are summarized in **Table 3**. Notably, high hole carrier mobility can be achieved in atomically thin 2D metal oxide, such as novel h-TiO$_2$ and conventional α-MoO$_3$ with defect engineering. Thus, the 2D metal oxide is expected to make up for the shortage of environmentally stable p-type 2D semiconductor materials. However, 2D metal oxides with high mobility and good quality are still scarce, which request further exploration.

Complementary inverter is the basic building block in digital/analog circuits, which typically consists of n-type and p-type transistor in series. Atomically thin oxides are highly expected in inverter due to the anticipative low cost and low power consumption. Huang et al.[46] has fabricated a high-performance p-channel FET based on SnO with thickness of ~1 nm, as well as the n-channel FET based on thin layer In$_2$O$_3$ (Figure 8h). The SnO was fabricated by metal-liquid printing process at 200 °C in air condition. By oxygen-vacancy defect termination for the SnO, the SnO FET exhibited a hole

mobility of ~0.47 $cm^2 V^{-1} s^{-1}$, low off current of $<10^{-12}$ A, on/off current ratio of ~10^6 and a SS of ~2.5 V/decade (Figure 8i). The low-power inverter based on p-channel SnO FET and n-channel In_2O_3 FET was fabricated, of which voltage-transfer characteristics (VTC) exhibited sharp voltage transition between the high and low states and clear switching with rail-to-rail output swings, and a high gain (117) was obtained at V_{dd} = 40 V (Figure 8j). The power consumption was estimated from VTC, revealing a low power dissipation of < 2 nW for the fabricated inverter.

2D metal oxide also can be used to form hybrid vdW junctions with other 2D materials. Wang et al.[164] has demonstrated a p-SnO/n-MoS_2 vdW heterojunction device, in which the thickness of MoS_2 varies in 1-, 3-, 7-layers. The devices show good ideality factor 1.77 for the 7-layer MoS_2 and large rectification ratio up to ~10^4. Anti-ambipolar transfer behavior of this device was observed and further applied in a series of gate tunable pulsed laser response measurements.

Notably, many FETs based on atomically thin 2D metal oxides have been demonstrated with the assistance of liquid metal printing method in recent studies, such as n-type In_2O_3,[46] SnO_2,[165] IZO,[69] ITO,[165] and p-type SnO,[146] β-Ga_2O_3.[166] Most of these FETs exhibit good performances in terms of mobility and on/off ratio, which are comparable to the corresponding oxide thin film transistor.[167] To get good performance, attention should be paid to the following aspects. Firstly, a small amount of liquid metal may stick on the 2D metal oxide as metallic residue after printing. For instance, the metallic Sn residual on the 2D SnO leads to a relative high mobility and low on/off ratio.[46, 146] A post thermal annealing can help to deal with the metallic residual issue.[46, 165] Besides, tuning the doping metal or level can help to promote the performance of the transistors (e.g., Sn or Zn-doped In_2O_3) [69, 165]. Currently, 2D metal oxide that prepared by liquid metal printing method usually features in the polycrystalline form, which is unfavorable for device performance and reliability in large-scale integration. Nevertheless, to get further improvement, it is possible to achieve controllable preparation of 2D metal oxide with desired crystallinity, thickness, and composition by adjusting the printing and post-treatment condition (e.g., liquid metal alloy composition, temperature, reaction time and oxidizing environment).[168]

4.1.2. High-κ dielectric

To achieve high performance 2D FET, many efforts has been made in improving the physical and electrical properties of semiconductor channel materials for high mobilities or bandgap modulation.[6] However, the ultimate FET performance is always determined by the quality of the gate dielectric layer and its interface with the semiconductor channel.[76]

The relative dielectric constant κ (also denoted as ε_r), bandgap, breaking down field, leakage current are significant metrics for evaluating the dielectric performance. The capacitance of the insulator is usually measured with LCR meter on a metal-insulator-metal (MIM) or metal-insulator-semiconductor (MIS) device in capacitance-voltage and capacitance-frequency mode (typically from 1kHz to 1MHz). The κ value of the dielectric material can be calculated from its capacitance at a relatively low frequency, as shown in Figure 9a. The high κ value is favorable for scaling the equivalent oxide thickness (EOT) according to the equation of EOT = 3.9t/κ, in which t is the thickness of the dielectric layer. Besides, a large breakdown field with low leakage current are required to ensure the device reliability and power efficiency, which typically rely on the material type, quality and stoichiometry. The breakdown field can be extracted from current-voltage sweeps curve of a device with MIM or MIS structure at which the leakage current exhibits an irreversible increased value of several orders of magnitude (Figure 9b). Ideally, the breakdown field of the dielectric should exceed 10 MV cm^{-1} for EOT below 1 nm and leakage current density requirement varies in different electronic applications.[76] Moreover, A large bandgap with sufficient band offset to channel material (ΔE > 1 eV) is important for reduce the gate leakage current (Figure 9c).[169] The band diagram of several high-κ materials and 2D channel semiconductor materials are depicted in Figure 9e. In 2D FET, the quality of dielectric/channel interface are mostly determined by the quality of the dielectric surface due to the atomic flat nature of 2D channel semiconductor. As shown in Figure 9d, the density of interface states D_{it} is often used to evaluate the interface quality, which can be estimated from the SS of the FET device based on the following equation:

$$SS = 1/slope = \ln(10)\frac{k_B T}{q}\left(1+\frac{C_{ch}+qD_{it}}{C_G}\right) \tag{2}$$

where k_B is Boltzmann constant, T is absolute temperature, q is the elementary charge, C_G is the gate insulator capacitance and C_{ch} is the depletion layer capacitance of 2D FETs. Typically, a perfect interface can lead to an ideal SS value of ~60 mV decade^{-1} at 300 K.

Metal oxides are usually high-κ material due to the inherent strong ionic polarization, in which conventional oxides like amorphous Al_2O_3 and HfO_2 thin films have been used as gate dielectric 2D FET. The amorphous HfO_2 thin film is alternative dielectric material for the electronic industry, which possesses a large relative dielectric constant (> 20) and a band gap of 5.2-5.9 eV. ALD or other CVD and PVD approaches are the conventional techniques for HfO_2 dielectric thin film preparation, by which the minimum deposited thickness is 3-5 nm.[170-171] However, the direct ALD growth of oxide films on 2D semiconductors may lead to a highly porous thin film due to the random nucleation at

defects, edges and impurities during the deposition.[172] The highly defective thin film not only has a large number of charge traps inside, but also dangling bonds at the interface with 2D semiconductors, leading to a deterioration of the device reliability and performance. The surface functionalization of 2D semiconductor has been proved as an efficient way to improve the quality of the dielectric film. Wang et al. demonstrated that a uniform and pinhole-free Al_2O_3 thin film can be deposited on the surface of MoS_2 after remote forming gas (H_2/N_2) plasma pretreatment. The MoS_2 FET with 6.1 nm Al_2O_3 top gate dielectric demonstrates excellent electrical performance with SS of 85 mV dec^{-1}. The leakage current was suppressed below $< 10^{-5}$ A cm^{-2} at 4 MV cm^{-1}. The non-ideal SS value (> 60 mV dec^{-1}) indicates a considerable density of traps remain at the interface between Al_2O_3 and MoS_2. Besides, using interfacial seeding layers such as oxide layers,[173-174] organic molecules,[175] boron nitride (BN)[176] are also useful for improving the quality of the followed deposition of oxide dielectric.[172] Recently, using 3,4,9,10-perylene-tetracarboxylic dianhydride (PTCDA) (~0.3 nm) as a buffer layer on graphene and TMDs can significantly improve the quality of HfO_2 dielectric. The 1.45 nm HfO_2 dielectrics (EOT =1 nm) on PTCDA exhibited a defect-free interface quality, high breakdown field (E_{bd} = 16.5 MV cm^{-1}) and low leakage current ($J < 10^{-2}$ A^{-1} cm^2) at 1 nm EOT. The MoS_2 FETs with PTCDA/HfO_2 dielectrics demonstrate an ideal SS (60 mV dec^{-1}) with low operating voltage of 0.8 V. The thinner EOT of 0.77 nm at thickness of 1.5 nm dielectric could be possible when the oxides with higher dielectric constant was applied, such as ZrO_2 (ε_r = 35).[177] However, making homogeneous PTCDA monolayer may be challenging due to its discrete molecular characteristic.

To overcome the challenges of interface states (e.g., impurities, oxide dangling bonds) and defect bands in amorphous oxide film dielectric, recent advances in 2D metal oxides have proposed some feasible ways to achieve high-performance in 2D FET device, including using native 2D oxides, molecular crystalline insulators without dangling bonds and crystalline insulators forming vdW gap with channel materials. **Table 4** has summarized **t**he performance of high-κ 2D metal oxide dielectric with sub-5 nm EOT, as well as the metal oxide thin films. Here, we will discuss the material design and principle underlying the excellent dielectric performance, as well as the opportunities and challenges.

To get clean dielectric/semiconductor interface and high-quality dielectric, many studies focus on partially oxidation of 2D TMDs to form metal oxide/2D TMDs heterojunction, such as HfS_2[159], $HfSe_2$ and $ZrSe_2$[178]. Utilizing native oxide (Figure 9f) as dielectric is highly expected to produce excellent semiconductor-dielectric interface and reduce the effects of interfacial traps, such as Si/SiO_2[179], or SiC/SiO_2[180]. Native high-κ dielectric HfO_2, Ta_2O_5, ZrO_2 are promising dielectric and highly compatible

with HfX_2, TaX_2, ZrX_2 (X=S, Se, Te), respectively. Lai et al.[159] have demonstrated a thickness-controllable chemical conversion of 2D HfS_2 into its native high-κ oxide HfO_2 using O_2 plasma treatment. The atomically sharp and clean HfS_2/HfO_2 interface can be obtained since the interface is confined inside of the hybrid structure during the plasma treatment. The converted HfO_2 has been confirmed as an effective dielectric material, with a low D_{it} value (6×10^{11} cm^{-2} eV^{-1}). Given by the high interface quality, the FET based on HfO_2/HfS_2 hybrid structure depicted excellent SS value of ~67 mV dec^{-1} and on/off current ratio up to 10^7, which exceeded the performance of the FET based on ALD HfO_2 on HfS_2.[181] The oxidization mechanism of $HfSe_2$ and $ZrSe_2$ under mild condition has been revealed by Mleczko et al.[178] Upon exposure of $HfSe_2$ and $ZrSe_2$ in an ambient condition, the amorphous sub-stoichiometric native oxide HfO_x and ZrO_x will be gradually and primarily formed from top-down without self-limiting, during which the Se atoms are displaced O atoms. They also fabricated top-gate $HfSe_2$-based FETs with native high-κ HfO_2 oxides. Although the device did not exhibit outstanding transistor performance due to the interface quality, from a qualitative point of view, insulating native oxide in $HfSe_2$ can suppress the thermal activation of the interfacial trap states. Thus, native 2D oxide exhibits various performance depending on the nature of the source 2D semiconductor. In addition, this strategy requires that native oxide of 2D semiconductor materials have excellent dielectric properties, such as HfO_x and ZrO_x. Still, these native 2D oxides are amorphous and therefore contain distinct defect bands, leading to degradation in dielectric performance relative to the crystalline one. However, up to now, the crystalline native 2D oxide can only form on the 2D material with special structure. Peng's group[156] has demonstrated that an atomically thin insulating layer of bismuth selenite (Bi_2SeO_5) crystal (ε_r ~ 21) can be conformally formed by layer-by-layer oxidation of Bi_2O_2Se at high temperatures, guaranteeing a chemically clean and atomically sharp interface between Bi_2SeO_5 dielectric and Bi_2O_2Se semiconductor. High-performance Bi_2O_2Se FETs can be fabricated with native oxide dielectric, showing SS value of ~75 mV dec^{-1} and mobility up to 300 cm^2 V^{-1} s^{-1}, and the integrated inverter circuits exhibit a large gain up to 150. Later, their group has improve the quality of dielectric β-Bi_2SeO_5 using UV-assisted intercalative oxidation approach.[157] The Bi_2O_2Se FET device with 2.7 nm native Bi_2SeO_5 exhibits SS value of 65 mV dec^{-1}. However, under oxygen plasma treatment at room temperature, the amorphous form, namely Bi_2SeO_x, will be obtained on the surface of Bi_2O_2Se.[158] Therefore, it seems to be possible to achieve high quality native 2D oxides by optimizing the preparation condition. Besides, exploring novel source 2D materials with excellent insulating native oxides is also a promising route.

Using dangling-bond-free metal oxide as dielectric is another alternative idea to improve the dielectric/2D semiconductor interfaces, since the amorphous nature and imperfect dielectric/2D

WILEY-VCH

semiconductor interfaces are always major obstacles to eliminate the charge scatters and traps. Additionally, the damage to 2D channels may occur during dielectric deposition processes[182]. vdW insulators, for instance, epitaxial calcium fluoride (CaF_2) and multilayer hBN have been investigated to preserve the intrinsic properties of 2D semiconductors in FETs.[78, 183] Recently, vdW 2D metal oxide dielectrics have been developed which exhibit great potential in 2D devices. As shown in Figure 9g, Liu et al.[34] fabricated an inorganic molecular crystalline film of antimony trioxide (Sb_2O_3) *via* thermal evaporation deposition. The Sb_2O_3 consists of Sb_4O_6 polyhedra, indicating a dangling-bond free surface with less charge traps. The atomically thin Sb_2O_3 possess a relative dielectric constant ε_r = 11.5 but a narrow bandgap of 4 eV and low breakdown field of 2.7 MV cm^{-1}. MoS_2 FETs with 10 nm Sb_2O_3 dielectric film (EOT=3.3 nm) exhibited a supply voltage of 0.8 V, on/off current ratio of 10^8 and SS of 64 mV dec^{-1}. However, when the Sb_2O_3 thickness reduced to 5 nm (EOT=1.6 nm), the leakage current started to increase owing to the direct tunnelling of current through the Sb_2O_3 film as a result of narrow bandgap. In other works, the Sb_2O_3 thin films in various amorphous degree exhibit ε_r values in the range of 5-13 and breakdown electric field below 6 MV cm^{-1}.[184] Peng et al. prepared 2D α-Sb_2O_3 nanoflake by CVT method, in which 2D α-Sb_2O_3 exhibited a unexpected low κ (ε_r = 2.0~2.5). The analysis revealed that low density of Sb_4O_6 molecular cage and polarity neutralization in the crystal played an essential role in the low κ nature.[184] Messalea et al. reported high-κ (ε_r = 84) dielectric 2D Sb_2O_3 by liquid metal printing, where the 2D Sb_2O_3 exhibited a thickness between ~1.5 and ~3 nm and the lateral dimensions up to millimeter, whose breakdown electric field reached ~10 MV cm^{-1}.[147] Thus, tuning the preparation methods have significant impact on the dielectric properties of molecular crystalline 2D metal oxide and therefore improve their performance in devices. Moreover, exploring other inorganic molecular crystals with higher dielectric constants and large bandgaps can probably realize 2D FETs with sub-1-nm gate dielectric.

Another promising strategy is to adopt crystalline insulating materials with atomically flat surfaces to get a better dielectric/2D semiconductor interfaces than deposited amorphous oxides. High-κ perovskite oxides such as $SrTiO_3$ (STO) (ε_r=300) is promising candidates for single crystalline dielectric in future 2D electronic devices. However, the bandgap of STO is below 4 eV (3.2-3.8 eV) which may cause high leakage current in thin film morphology. Introducing a clean vdW gap at dielectric/channel interface can form an effective barrier to reduce the tunnelling probability of carrier, suppressing the gate leakage currents (Figure 9h).[33, 76, 182]

Recently, the free-standing perovskite oxide films with thickness down to single unit cell have been synthesized and transferred onto various substrates.[44] The moderate transfer method has been

developed to make clean vdW interface of $SrTiO_3$/2D semiconductor, which can also avoid the damage to 2D semiconductor during direct deposition of $SrTiO_3$[44, 121, 185]. Yang et al.[186] have investigated n-type MoS_2 and p-type WSe_2-based FETs on silicon substrates with single-crystal STO flake as the top-gate dielectric. The STO is epitaxially grown on a water-soluble sacrificial layer $Sr_3Al_2O_6$ (SAO) and subsequently transferred with the help of PDMS. The clean interface gives MoS_2-based transistors an excellent performance with an on/off current ratio of 10^8 and a minimum SS of 66 mV dec^{-1}. Huang et al.[33] have successfully extended crystalline STO dielectric into wafer-scale and prove the existence of vdW gap at STO/semiconductor interface (Figure 9h). The back-gated FET arrays are made of scalable MoS_2 films by CVD and transferred 16 nm STO dielectrics (EOT = 1 nm), which exhibit steep SS (70 mV dec^{-1}) and on/off current ratios up to 10^7. However, the further scaling down of EOT may result in large tunneling leakage current due to their inherent relative narrow bandgap (< 4 eV). Therefore, the trade-off between κ value and bandgap is critical for optimizing the overall dielectric performance.

Notably, the transfer process should be carefully manipulated to avoid possible contamination, as well as structure delamination and crystal damage. Metal oxides are mostly hard and brittle in bulk form. However, reducing the thickness of a material into atomical level can substantially increase their flexibility.[92] Thus, 2D materials usually possess extremely high in-plane stiffness and out-plane bending flexibility. The systematical study on mechanical properties of 2D metal oxides have not been reported yet. However, it has been demonstrated that the freestanding $SrTiO_3$ with a few unit-cell thick become flexible and can be bent and even folded in on themselves, which is comparable to the covalent 2D vdW materials like graphene, hBN.[44] 2D ITO and InO_x-containing superlattices shows negligible fluctuation in resistance after thousands of bending cycles test, while the commercial ITO sample exhibits resistance failure in the same test.[29, 74] This finding suggests that 2D metal oxides could have excellent endurability for transfer process and potential in flexible electronics applications. Moreover, vdW 2D materials like graphene, hBN, and MoS_2 exhibit excellent chemical stability, while many other 2D material suffer from the sensitivity to ambient conditions, which has hindered their practical application in devices. In general, 2D metal oxides are mostly stable in ambient conditions, but some 2D metal oxides may deteriorate by absorbing moisture and chemical active molecules in humid air. Besides, the transfer process often involves various solutions, like organic solvent, etching solvent, and pure water. 2D metal oxides are mostly resistant to the organic solvents but may be sensitive to the acidic or basic etching solution. Thus, solvent-free (e.g., PDMS-assist transfer) or only organic solvent involved (e.g., PMMA-assist transfer) methods are mostly preferable for 2D metal oxides. Besides, water involved transfer method is suitable for

the water-stable 2D metal oxide, although the water molecules are probably adsorbed on the 2D metal oxide but can be completely removed by post-annealing without damage to the material.

4.1.3. Others functional layer

In addition to acting as a channel material and dielectric materials, 2D metal oxides also can play other important roles in the electronic and optoelectronic device to regulate the device performances, such as: 1) tunneling contact layer in metal-interlayer-semiconductor (MIS) contact, 2) doping layer on channel materials, 3) protective layer of the device and 4) wetting buffer layer on 2D TMDs or graphene (as shown in **Figure 10**).

Tunneling contact layer: Low contact resistance is critical for high performance 2D TMDs devices in terms of achieving high 'on' current, large photoresponse and high operation speed.[17] In general, the contact resistance (R_C) of the MIS contact is mainly consist of: (i) the Schottky barrier resistance (R_{SB}) depending on the Schottky barrier height (SBH) of the metal-semiconductor junction and (ii) the tunneling resistance (R_T) depending on the tunneling barrier formed by the interlayer ($R_C = R_{SB} + R_T$). The inserting interlayer can weaken FLP and suppress the SBH to reduce R_{SB}, but also induce additional tunneling barrier to give a considerable R_T with increasing thickness of interlayer. Thus, the thickness of interlayer should be optimized by a trade-off between R_{SB} and R_T for the low resistance contact.

In previous works, various materials have been used as interlayer to reduce the R_C on n-type MoS$_2$, including Ta$_2$O$_5$,[187] TiO$_2$,[188-189] MgO,[190] and h-BN.[191] However, the R_C reduction are mostly achieved by the reduction of R_{SB} at contacts, but no underlying mechanism has been proposed for further improvement in R_T reduction. Theoretical studies of MIS contact on n-type semiconductors have recommended that choosing interlayer with low conduction band offset to semiconductor (denoted as CBO-semiconductor) can reduce the tunneling barrier height and thus reach a lower contact resistance.[192-194] For example, Gupta et al.[194] have carried out theoretical and experimental study to evaluate the MIS contact resistance on n-type germanium (Ge) with various materials as interlayer (Al$_2$O$_3$, GeO$_2$, Si$_3$N$_4$, TiO$_2$, ZnO, ITO). The selected materials exhibit different bandgaps, dielectric constants, and conduction band offset to Ge (CBO-Ge). The results reveal that all the materials with optimized thickness can achieve low MIS R_C, while the materials (TiO$_2$, ZnO, ITO) with CBO-Ge of -0.1 eV can give additional benefit in further lowering R_C.

For p-type semiconductor, the tunneling contact layer with high work function has also been introduced to form p-type contacts on 2D semiconductor. Most of metal oxides have the relative low

work functions (< 5.6 eV), while MoO_3 exhibits high work function potential of up to ~6.6 eV and has been used as an efficient hole injection layer which could form p-type contact on MoS_2 and WSe_2.[195] As shown in Figure 10a, Farmanbar et al.[196] has carried out a theoretical study to evaluate the suitable interlayer for effective p-type contact on various MX_2 (M = Mo, W; X = S, Se, Te). The simulation chose the 2D materials with relative low work function materials (e.g., metallic graphene, insulating h-BN) and high work function materials (semiconducting MoO_3, metallic NbS_2) as interlayer. The result has revealed that a bilayer MoO_3 can give a zero SBH for contacts (*i.e.,* ohmic contact) to all MX_2 (M = Mo, W; X = S, Se, Te) as the Fermi level is pinned at the MoO_3 conduction band (CB), ensuring that bilayer-MoO_3 will act as effecient media to transport charge carriers into MX_2 instead of as a tunnel barrier (Figure 10b). Besides, layered V_2O_5 and WO_3 is also promising for p-type contact due to their large work functions of 7.0 eV and 6.4 eV, respectively. Notably, these metal oxides are strong oxidizing agents, which may suffer from chemical instability.

Channel doping layer: Deposition of ultrathin metal oxide on 2D TMD could lead to selective doping.[197] The Al_xO_y can give a n-type doping on MoS_2, but no significant doping on WS_2. The further studies have revealed that the selective doping phenomenon sources from donor states in the Al_xO_y band gap, which can donate electrons depending on the position of the CBM of the TMD.[197] With different band structure, the native oxides (e.g., WO_x,[150] MoO_3[198]) have been reported as p-type doping layer for the host 2D materials. The selective doping mechanism of metal oxide thin layer can be further explored for more complex device and circuit fabrication. Moreover, the strong doping can modify the work function of 2D TMDs and therefore change the carrier type, for example, from in original p-type into n-type carrier transport behavior.[199]

Similarly, 2D metal oxides also can realized carrier doping to the 2D semiconductor. As shown in Figure 10c, Holler et al[200] have fabricated a WSe_2-based FET devices and stacked the exfoliated MoO_3 layers on top of the channel. The FET device exhibits a typical n-type transfer curve in pristine state, while a prominent hole conduction behavior appears after stacking of MoO_3, resulting in an ambipolar carrier transport in the heterojunction channel (Figure 10d). The large work function MoO_3 can extract electrons from WSe_2 and achieve hole doping.

In addition, in diamond FET, high electron affinity transition metal oxides as a surface acceptor material can induce transfer doping on the hydrogen-terminated diamond surface. This process leaves behind corresponding holes within the diamond, forming a 2D hole gas (2DHG) beneath the surface, which can significantly improve the peak drain current of diamond FET. Crawford et al. demonstrated V_2O_5 incorporated on diamond surface. The devices with gate lengths down to 50 nm

exhibited a peak transconductance of ~150 mS mm^{-1} and a peak drain current of ~700mA mm^{-1}.[201] Similar doping effects have also been reported in Ga_2O_3,[144] MoO_3,[202] and WO_3.[203]

Encapsulation or protective layer: 2D materials like TMDs have fascinating physical properties that make them being promising candidates for future electronics and optoelectronics. However, during the process of device fabrication and integration, 2D materials may be exposed to environmental stimuli, such as chemical reagents, high temperature, and high energy irradiation, which will damage their structure and properties. Thus, it is also important to protect 2D materials from fabrication process, by passivation or encapsulation. MoS_2 and h-BN have been utilized as protective layer for 2D device,[143, 204] but the limitations still remain on the aspects of lateral size and quality.[205] As shown in Figure 10e, recently, 2D a-Ga_2O_3 has been proposed as a protective layer to passivate semiconducting materials.[143] 2D a-Ga_2O_3 generated on the liquid metal surface can be directly printed or transferred onto the WS_2 monolayer to form capping layer. The studies have revealed that the a-Ga_2O_3 passivation significantly enhances the optical property of WS_2 by suppressing effects of the defects in WS_2. Moreover, the 2D a-Ga_2O_3 can act as a protective layer for further deposition of dielectric Al_2O_3 layer in device integration process. As shown in Figure 10f, direct deposition of Al_2O_3 on top of bare WS_2 strongly quenches the exciton photoluminescence (PL). However, with the protective layer of 2D a-Ga_2O_3 or h-BN, exciton PL intensities can be enhanced with approximately two orders of magnitude in comparison to the WS_2/Al_2O_3, indicating the well protection function of 2D a-Ga_2O_3 or h-BN. Notably, the stronger PL intensity in WS_2/Ga_2O_3/Al_2O_3 sample reveals that 2D a-Ga_2O_3 is more compatible with oxide dielectric than 2D h-BN due to the similar ionic nature. Thus, the 2D metal oxide exhibits great potential in top-gate architecture fabrication in 2D oxide-based transistors.

Wetting buffer layer: As discussed before, direct ALD of metal oxide dielectric layer on 2D materials will cause random nucleation at edges, defects and impurities, resulting in highly porous thin films. Buffer layers have been developed for the uniform deposition of oxide dielectric on 2D materials, including oxidized metal layers, [173, 206] organic molecules,[182] h-BN,[207] and 2D surface activation.[174] 2D metal oxide also can be used to modify the non-dangling 2D surface as a buffer layer before the dielectric deposition. Addou et al.[18] has demonstrated high-κ dielectric Y_2O_3 monolayer on graphene by electron-beam evaporation (EBE) under ultra-high vacuum (UHV). Y_2O_3 monolayer layers can be adopted for charge doping of metal supported graphene and serve as atomic buffer or nucleation layers in consequent approaches.

Notably, the stacking of 2D metal oxide on 2D semiconductor usually has the cross and combination of the effects as-mentioned above. Thus, the specific role of 2D metal oxide should be analyzed according to the actual changes of material properties and device performance.

4.2. Photodetection

A photodetector is an electronic device that can convert incident light into an electrical signal. Emerging 2D materials are considered to be promising materials for photodetectors due to their unique optical and electrical properties, which could realize a wide response range from UV to long-wave infrared.[208] Besides, 2D heterojunction has been widely studied as a powerful tool to improve the performance and functionality of photodetector.[209] Despite remarkable progress, most of the 2D semiconductors have no expertise in UV detection owing to their relatively moderate bandgap (1-2 eV). 2D metal oxides semiconductor can be adopted as a complementary role in 2D photodetection, of which band gap located in the range of 3-5 eV are preferable for UV light detecting. The versatile band structure engineering strategies could be further empoyled to extend their capabilities for specific light detection or broad range light detection. Moreover, adding 2D metal oxide into the toolkit for 2D heterojunction can bring new insight in photodetection. In this section, we will discuss the recent progress of the photodetector based on 2D metal oxides and their heterojunctions.

4.2.1. Photodetector based on 2D metal oxide

The operation of a photodetector is monitoring the electrical signal variation as the light signal change. The photocurrent generation mechanism is mostly related to excitation of free carriers arising from optical transition (e.g., photoconductive effect (PCE), photovoltaic effect (PVE)), as well as thermal effect (e.g., photothermoelectric and bolometric effect). The photodetectors with planar metal-semiconductor-metal (MSM) configuration are usually designed based on PCE, in which photoinduced excess carriers increase the free carrier concentration, resulting in a higher light current (I_{light}) than dark current (I_{dark}) in the semiconductor under an applied voltage (as shown in **Figure 11**a). The photoresponsivity, external quantum efficiency (EQE), response time, specific detectivity (D^*) are important performance metrics for photodetector. The metal oxides are thought as promising candidates for high performance UV detection owing to the outstanding light sensitivity, wide bandgap, earth-abundance properties and environmental stability. With the recent advances of 2D material synthesis, several 2D metal oxides have been studied in photodetection in the wavelength of UV region, even up to visible and infrared region (as shown in Figure 11b).

WILEY-VCH

The 2D metal oxides with wide bandgap are typically capable for high performance visible-blind light detection. Krishnamurthi et al.[42] fabricated a visible-blind photodetector based on 2D ZnO that exfoliated from molten Zn. The UV-vis-NIR spectra of the ZnO nanosheets shows a peak adsorption at ~300 nm and absorption cut-off point at ~450 nm (Figure 11c). At a wavelength of 365 nm, the two-terminal photodetector based on this ZnO nanosheet demonstrated a responsivity (R), detectivity ($D*$) and external quantum efficiency (EQE) of 12.64 A W^{-1}, and 5.81 × 10^{15} Jones and 4.3 × 10^3 %. The device exhibited excellent figure of merit at low operating voltage and low optical intensity of light with 365 nm wavelength, while it showed a less responsivity at a wavelength of 280 nm owing to the strong density of states near the band edge (Figure 11d).

Owing to the atomically thin feature, incorporating a functional molecule on the surface of 2D metal oxide may significantly change their optical and electronic properties, leading to a variation in the photodetection performance. Yu et al.[35] have developed a photodetector based on solution-processed 2D ZnO-SDS nanosheet which showed a higher responsivity to the light of 254 nm wavelength (Figure 11f). The result can be attributed to the effect of surfactant bonded on the surface of 2D ZnO. As shown in Figure 11e, in the range of 330-200 nm, 2D ZnO-SDS can maintain a continuous increase of the absorption value while the strongest UV-vis absorption values are in 260-300 nm range. Thus, the surfactant-assisted 2D ZnO are expected to be more efficient for absorbing deep-UV light. The 2D ZnO based photodetector demonstrated an optimal rise/decay time (3.97 s/5.32 s) at the wavelength of 254 nm and long-term stability (>30 days) under ambient conditions.

Interestingly, the photodetection performance and carrier transport properties of 2D metal oxides exhibit a considerable thickness-dependent behavior, suggesting that thickness control is an efficient way to modulate the photodetector for desired application. Due to the unique structure, reduced dimension and interesting physical properties, 2D layered perovskite oxides can be applied in potential optoelectronic devices. Li et al.[30] synthesized 2D perovskite $Sr_2Nb_3O_{10}$ (SNO) nanosheets with 1.8 nm thicknesses via liquid exfoliation. As shown in Figure 11g, the 2D SNO sample showed a sharp absorption edge at 300 nm and negligible absorption over the visible range, with estimated optical bandgap of 3.90 eV, indicating the potential for UV detection. The photodetectors based on monocrystal of a few-layer SNO showed highly thickness-dependent dark current, demonstrating that thinner SNO have an extremely low dark current of ~10^{-14} A. The 2D SNO exhibited a thickness-dependent photodetection performance. As shown in Figure 11h, the thicker SNO showed higher responsivity due to the higher UV absorption in thicker materials. Besides, all the SNO photodetectors exhibited noticeable cutoff edges located at ~310 nm with the highest responsivity

WILEY-VCH

at 270 nm, representing that 4, 6, 7L SNO has similar bandgap which is consistent with the value in Figure 11g (3.9 eV). Notably, all the SNO devices showed narrowband responsivity, indicating an excellent wavelength selectivity. The optimized 7L SNO-based photodetector exhibited high external quantum efficiency (5.6×10^5 %), narrowband R (1214 A W^{-1}), high D^* (1.4×10^{14} Jones) and fast response speed. This work revealed that when light absorption dominates the thickness effect, the thicker 2D metal oxide will present better photodetection performance in terms of external quantum efficiency, photocurrent, responsivity and detectivity.

Control over the polymorph phase of a metal oxide is reasonable and effective for designing high-performance photodetector, since the various polymorphs of a given metal oxide possess different electronic and optical properties. For instance, the Bi_2O_3 has four main polymorphic structures (α-, β-, γ-, δ-Bi_2O_3), in which γ-Bi_2O_3 exhibits the largest bandgap (>2.9 eV) and highest UV absorption, indicating its great potential for UV detection among above polymorphs.[48] As shown in Figure 11i, Wu et al. synthesized high quality ultrathin γ-Bi_2O_3 single crystal flakes with thickness down to 4.8 nm on mica *via* vdW epitaxy method. XPS and TEM characterization revealed the high density of oxygen vacancies on γ-Bi_2O_3 surface. These oxygen vacancies are vital for the stability of metastable γ-Bi_2O_3 at room temperature. The optical bandgaps of 2D γ-Bi_2O_3 are estimated to be 3.1 eV to 3.4 eV (for samples from 26 nm to 6 nm), owing to the quantum confinement effect. At a wavelength of 365 nm, the 2D γ-Bi_2O_3 displays an ultrafast response speed (rise ≈ 290 μs and decay ≈ 870 μs), a responsivity of 64.5 A W^{-1} and a D^* of 1.3×10^{13} Jones (Figure 11j). The ultrafast response speed surpasses the most of photodetectors based on 2D metal oxide, which highlights the high crystallinity of 2D metal oxide growth by vdW epitaxy (CVD), even in the present of the high density of oxygen vacancies.

Synergism of photo-induced electric effect and photo-induced thermal effect can effectively enhance the performance and functionality of photodetectors, which may endow wide bandgap semiconductor materials with infrared light detection capabilities. The detection of ultrabroadband spectrum (from UV to LWIR) is promising for sensing, imaging and communication. Recently, Yin et al.[36] demonstrated ultrabroadband photodetector based on ultrathin Fe_3O_4 nanosheets synthesized by a space-confined CVD method with high performance. Optical absorption spectra in Figure 11k shows that the absorption edge of 8 nm-thick Fe_3O_4 is located at 463 cm^{-1}, corresponding to the 21.6 μm wavelength. The absorption edge of 2D Fe_3O_4 nanosheets will be ~310 cm^{-1} once the thickness is increased to ~25 nm, indicating 32.3 μm wavelength light can be detected. The performance of photodetectors based on transferred 2D Fe_3O_4 nanosheets were characterized under illumination of

WILEY-VCH

wavelength from 375 nm to 10.6 μm. As shown in Figure 11l, the value of R increases with augmented wavelength from near-wavelength infrared (NWIR) to LWIR (10.6 μm). At 10.6 μm wavelength, the remarkable responsivity (561.2 A W^{-1}), EQE (6.6×10^3 %), and D^* (7.42×10^8 Jones) can be achieved, and the high performance can be attributed to the synergistic effect of bolometric effect and photoconductive effect (Figure 11m). Photon absorption induced heating process may contribute to the resistance change in bolometric effect. The photoconductive effect involves generation of electron-hole pairs, trapping minority carriers and inducing more majority carriers to achieve large photogain.

Besides, the in-plane anisotropy in 2D metal oxide crystal could significantly affect the photodetection performance. Zhong et al.[210] used 2D α-MoO3 monocrystal for a solar-blind photodetector, depicting strong in-plane anisotropy in transport properties and optoelectronic response. Under 254 nm UV light, the photocurrent along b-axis is 5 times higher than the values along c-axis, and on/off current ratio is about 2 times high.

Table 5 summarizes the performances of 2D metal oxide photodetectors. The advantageous detection wavelength for most of 2D metal oxide is located in UV region due to their wide optical bandgap. The 2D metal oxides with good crystallinity usually demonstrate high photodetection performance while the defects in the materials will trap the photocurrent to give a low responsivity, detectivity and long rise/decay time. To solve these problems, improving the preparation process to enhance the crystal quality of 2D metal oxide is necessary. Moreover, numerous methods have been exploited to improve the performances of photodetectors, for instance, ferroelectric modulation, surface functionalization, heterojunction integration and doping. In the following section, we will introduce several examples of heterojunction strategies using 2D metal oxides, which can improve the device performance.

4.2.2. photodetector based on 2D metal oxide junction

The heterojunction can fundamentally modulate the photo-induced carrier and charge transport in photodetector, which can enable the improvement in photodetection performance. Several heterojunctions have been introduced in 2D photodetector with the assist of 2D metal oxides, such as channel p-n junction, channel/gate heterojunction and channel/contact electrode heterojunction.

The out-of-plane heterojunctions based on 2D metal oxides can bring new vdW interfaces into the semiconducting channel, where the heterojunction zone may exhibit a new bandgap structure. Especially, the p-n junction can act as a diode to provide effective charge generation and extraction.

Recently, 2D p-SnO/n-In$_2$O$_3$ vdW heterostructure was assembled using liquid metal vdW transfer technique (**Figure 12**a).[136] This work reveals that restacked 2D SnO and In$_2$O$_3$ shows a reduced bandgap of 2.3 eV while the bandgap of isolated sample is 4.08 eV for SnO[146] and 3.65 eV for In$_2$O$_3$.[211] The suitably narrow bandgap has improved the absorption ability, efficient charge separation of photogenerated electron-hole pair will occur, and the photoexcited electrons from the valence band (VB) of SnO can migrate to CB of In$_2$O$_3$ easily. The heterostructure performs much better photodetectivity than individual SnO and In$_2$O$_3$ devices, which shows a high D^* (5×10^9 Jones), responsivity (1047 A W^{-1}) and fast response time (≤ 1 ms) under 280 nm light illumination (Figure 12b-c). The heterojunction can also be formed in 2D metal oxide with TMDs.[164]

The photogating mechanism has been widely used to improve the performance of 2D photodetector by introducing sensitizers on 2D channel. The charge traps in sensitizers can act as a localized floating gate to modulate the channel conductance and therefore contributes to the enhancement of photo gain (G), while the slow detraping process could lead to long response time (t). To overcome this inherent G-t tradeoff, Guo et al.[212] has demonstrated a light-driven junction FET (LJFET), which consists of an n-type ZnO flake as the semiconductor channel and a p-type WSe$_2$ as a photoactive gate material (Figure 12d). In this architecture, WSe$_2$ nanosheet forms a p-n junction with ZnO. When the photon energy of the illuminating light is between the bandgap of WSe$_2$ (~1.2 eV) and ZnO (~3.3 eV), only photocarriers in WSe$_2$ are excited, which can slightly enlarge the depletion of the junction region to reduce the current in the ZnO channel. Meanwhile, the reduced resistance of WSe$_2$ under the illumination provides a conductive route for the negative top-gate voltage that reversely biases the junction, which leads further enlargement of depletion region and decrease of current in ZnO channel. This LJFET device exhibited a high R (4.83×10^3 A W^{-1}) with a rapid response time (~10 μs) and a gain of ~10^4. The LJFET architecture breaks the gain-response time (*G-t*) tradeoff by decoupling the gain from carrier lifetime, providing a novel approach to realize fast-response and high-gain phototransistors (Figure 12e-f).

In addition, photogating effect in photodetector may generate large noise dark current owing to the charge trapping effect of the sensitizer materials, resulting in limited detectivity. To achieve high detectivity, low operating voltage and low noise current in photodetector, Feng et al.[213] has demonstrated phototransistor with a double-heterojunction configuration, which consists of a MoS$_2$ channel and two α-MoO$_{3-x}$ electrodes (Figure 12g). The formed double MoS$_2$/α-MoO$_{3-x}$ heterojunctions can provide positive effect and the device exhibited an ultrahigh detectivity of 9.8×10^{16} cm Hz$^{1/2}$W^{-1} and a quick response speed (rise time: 95 μs, fall time:105 μs) (Figure 12h-i). The

WILEY-VCH

mechanism namely photo-induced barrier lowering (PIBL) revealed that introducing α-MoO_{3-x} can lower the barrier to facilitate large photo gain and large electron injection. Meanwhile, no photogenerated carriers will be trapped in this configuration, resulting in intrinsically fast respond. The PIBL mechanism can introduce new opportunity and shed light on the development of future photodetectors.

Besides the key figure of merits in individual photodetector, the evaluation of integrated sensor array is also important for 2D metal oxides towards future practical applications, such as flexible transparent image sensors, and selective light-detecting imagers, artificial-intelligence photosensors. 2D metal oxides with ultra-wide bandgap have showed great potential as promising image sensors candidates for light detection of UV, especially solar-blind UV region. For example, Ga_2O_3 thin film has been widely investigated in solar-blind image sensor array since its absorption cut-off wavelength is below 280 nm, covering the most of solar-blind region (200-280 nm).[214-218] The performance of individual device and uniformity of the array are highly related with the crystallinity and defect level in the oxide layer.[215-216] Thus, fabrication of large-area 2D metal oxides with high quality and uniformity is crucial for high resolution image sensor array integration, where the CVD and MBE growth method seems to be more preferable despite its relative high cost. Moreover, thinning metal oxides to atomical level can widen the bandgap, shifting cut-off wavelength to deeper UV, benefiting for selective UV-detecting. Unfortunately, image sensors based on 2D metal oxides are rarely reported. On the contrary, the image sensors based on moderate bandgap 2D materials (e.g., graphene, MoS_2, etc) have been widely demonstrated in broadband imaging system,[219] active pixel image sensors,[220] vision systems,[221] and neuromorphic vision systems.[222-224] Therefore, 2D metal oxides can be expected to create an enhanced machine vision intelligent systems through reasonable design and combination with other moderate bandgap 2D materials.

4.3. Piezotronics and piezo-phototronics

The emerging piezotronics and piezo-phototronics have excessive potential in electronics-human/ambience interactions, for instance, robotics, human-machine interfacing, self-powered wearable electronics and biomedical engineering. The piezotronics couple semiconducting properties and piezoelectricity of a material by stress/strain, which have the ability to convert mechanical force into electricity and *vice versa*. The piezotronics device usually have a vertical metal-semiconductor-metal sandwich-like structure, or a simple FET configuration. Meanwhile, piezo-

WILEY-VCH

phototronics couple photon with semiconducting properties and piezoelectricity in third-generation semiconductors.[225] A simple piezotronics device can work as a strain sensors, of which performance can be evaluated by a gauge factor. However, piezotronics and piezo-phototronics effect can be coupled into various devices to change their performance, including Schottky-contact sensors, LEDs, photodetectors, solar cells, etc. Thus, it seems difficult to define a universal figure of merit to evaluate the modulation of the piezotronics and piezo-phototronics.[225] But the effective piezoelectric coefficient (d_{eff}) is important for evaluating the piezoelectric materials. A quick development of miniaturized electronic devices in nano-electromechanical systems calls for discovery and synthesis of low-dimensional piezoelectric materials. The scaling down of ZnO from nanowire to nanoplatelet leads to higher pressure/strain sensitivity.[226-227] Recent development has shown that atomically thin ZnO has great potential as promising materials in piezotronics and piezo-phototronics.

For piezoelectric devices, the piezoelectricity is the crucial factor which directly governs the performance. Conductive piezoresponse force microscopy (PFM) is usually applied to explore the out-of-plane piezoelectricity (**Figure 13a**). In atomically thin 2D ZnO, metal cation Zn and anion O are still tetrahedrally coordinated, and their centers overlap (Figure 13b, left). Upon applying stress along an apex of the tetrahedron, the centers of negative and positive ions are displaced relatively, leading to a piezoelectric polarization (Figure 13b, right), which induces the piezoelectricity along the c-axis.

In addition to the performance characterization of individual device, piezotronic stress-gated OR logic gates are successfully demonstrated by using a series of two 2D piezotronic transistors (Figure 13c-d). Wang et al.[228] has demonstrated 2D ZnO based piezotronic transistors with a ~2 nm channel length, in which the ZnO is sandwiched between the top and bottom Au electrode in vertical configuration. The strain-dependent out-of-plane piezopotential of ultrathin ZnO will work as gate voltage to switch the carrier transport. The PFM analysis shows that the effective piezoelectric coefficient (d_{eff}) of 2D ZnO is estimated to be ~23.7 pm V^{-1} which is about two times larger than bulk ZnO's d_{eff} and even larger than the d_{eff} of several inorganic ferroelectric ceramics. The stress-gated series of two piezotronics transistors can recognize various logic gates under different ways of applying pressure, indicating a potential in human-machine interface and intelligent robotics.

To further investigate the piezoelectric properties of ultrathin ZnO, Mahmood et al.[37] scaled ZnO down to even sub-nanometer thin using liquid metal approach (Figure 13e). The ZnO sheets with the optimized thickness of ~1.1 nm presented extremely high out-of-plane piezopotential and produced

a giant piezoelectric coefficient (d_{33}) of 80 ± 0.8 pm V^{-1} (Figure 13f). The DFT studies revealed that the ZnO thickness and the interactions of the ZnO with the substrate play significant roles in the exceptional polarization effects, in which ~1.1 nm-thick ZnO can balance these factors to display highest d_{33} value.

Different from devices in vertical-configuration, the piezoelectric effect of planar device can be regulated by multiple ways including interface modulation, channel modulation and light modulation. An et al.[229] demonstrated a 2D piezotronic device based on ZnO sheets with Au electrode in a planar configuration. The piezotronic devices can be effectively modulated by external mechanical stimuli on channel region and metal-semiconductor contact region, which is correlated with channel width gating effect and metal-ZnO interface gating effect, respectively (Figure 13g). The experimental and theoretical simulation results revealed that the electrical conductance will be increased if applying the compressive force on the electrodes due to the decrease of Au-ZnO Schottky barriers (Figure 13h); on the contrary, the electrical conductance of the device obviously decreases as the force increases if applying the force on the ZnO channel due to channel depletion effect from the piezoelectric polarization (Figure 13i). Notably, the metal-semiconductor interface barrier modulating is the main mechanism for the piezotronic effect in such device. Furthermore, the piezo-phototronic effects were also investigated in this device as illustrated in Figure 13j. The pressure applied on the metal electrode can significantly affect the photoresponsivity of the device. Figure 13k reveals that the output current exhibits gradual and monotonical enhancement if the applied pressure increases from 0 MPa to 5.3 MPa. When applying a compressive pressure of 5.3 MPa on the metal-semiconductor contacts, the 2D ZnO device has shown a high responsivity (300 AW^{-1}) with voltage bias 2 V, which is 2.3 times higher than that of no-pressure condition (Figure 13l). This finding suggested that multi-physical stimuli may unlock greater potential of 2D nanodevices for nano system.

4.4. Memristors

Memristors, a combination of memory resistor, usually refer to the two-terminal resistance switches that regulate and retain internal resistance state based on the external electrical operations. A simple memristor is composed of a solid electrolyte (resistance switching layer) sandwiched between two electrodes. The "charge carriers" (e.g., electrons, defects, vacancies, and ions) may migrate under the electric field to modulate the conductance of the solid electrolyte based on various mechanisms (e.g., conductive filament, charge trapping, phase engineering). The memristors usually have multi-level conductance states that can be gradually regulated, where the linearity and

WILEY-VCH

symmetry of conductance regulation is crucial parameters for synaptic memristors, as well as the maximum/minimum conductance ratio. Differently, the resistive random access memory (ReRAM), as a member of memristors, have only two resistance states with a large on/off resistance ratio, in which on/off ratio, state retention, switching speed are important figure of merits. The memristors with gate electrical modulation (memtransistors) and optical signal modulation (electro-photonic memristors or all-photonic memristors) have been proposed to reinforce the functionalities of the memristors. The emerging memristors based on 2D materials are leading candidates for artificial synapses and further neuromorphic computing architectures owing to the advantage of high integration density and low power consumption. Besides the unique electronic and optical properties, atomically thin 2D metal oxides have inherent advantage in terms of device scaling and integration with planar wafer technology. The redox active nature makes metal oxide a good solid electrolyte for ion transport, where the ion transport is similar to the behavior of neurotransmitters in biological synapses. In this section, we will discuss the applications of 2D metal oxides in the representative configurations of memristors containing ReRAM, memtransistor, and electro-photonic memristor.

 2D metal oxides and their heterostructures can serve as efficient ion transport medium in ReRAM, where oxygen vacancies and redox reactions play crucial roles. For example, a heterostructure of amorphous Al_2O_3 and crystalline 2D ZnO (~0.75 nm thick) has been adopted as resistance switching layer in ReRAM device with lateral configuration, as shown in Figure 14a.[40] The ReRAM device exhibits a bipolar resistive switching behavior with the operation voltage between ±10 V and high endurance of over 10^6 switching cycles (Figure 14b-c). The operating voltage is as high as ±10 V due to the long electrodes distance (~3 μm). The actual operating electric field is 2.9×10^6 V m^{-1}, which is at least one order of magnitude lower than other ZnO-based ReRAM devices, suggesting a great potential to achieve low power consumption. The mobility and the drifting velocity in 2D ZnO at low resistance state are estimated to be ~2400 cm^2 V^{-1} s^{-1} and 1.6×10^5 m s^{-1}, respectively. The characterizations reveals that the unprecedented high mobility in 2D ZnO can be attributed to the high density of oxygen vacancies induced by redox reaction with Al_2O_3 coating layer, and the memristive behavior is caused by high-speed drift of oxygen vacancies in 2D ZnO. This result highlights the potential of 2D heterointerface in design of high-performance memristor devices.

 Memtransistors have the third modulatory terminal (gate voltage) to modulate the conductance in the semiconducting channel materials, which could be beneficial for improving the performance of memristors in terms of conductance max/min ratio and the linearity and symmetry of conductance

WILEY-VCH

regulation, suggesting their great potential for artificial synapses and neuromorphic computing. Semiconducting 2D metal oxides with high mobility are suitable for channel materials in memtransistor. Moreover, the 2D metal oxides with various oxidation forms have the additional potential for resistive switching. For example, SnO_2 exhibits high electron mobility with various oxidation phases (i.e., SnO_2, Sn_2O_3, Sn_3O_4, SnO, and even metallic Sn). Huang et al.[41] developed a gate-tunable oxide based memristor using ~2 nm-thick polycrystalline SnO_2 nanosheets by liquid metal process (Figure 14d). The synaptic potentiation and depression characteristics are depicted in Figure 14e, which confirm the modulation of conductance max/min ratio varies by varying gate voltage bias. The memristors exhibited low conductance in nano Siemens (nS) range, providing low-power consumption operation of ~4.8 pJ and indicating the great potential in energy-efficient system. The gate-tunability could improve the recognition accuracy up to ~92.25 % after training, which emphasized the advantage of three terminal devices in neuromorphic computing (Figure 14f).

In addition, the extra response from multiple chemical and physical stimuli (e.g., ionic and optical) can be introduced to the synaptic memristors, enabling more device functionality to mimicking complex synaptic functions. For example, Krishnamurthi et al.[42] fabricated sensory memory device based on 5-nm thick 2D ZnO crystalline exfoliated from molten zinc metal (Figure 14g). This biomimetic photonic synapse can mimic versatile important synaptic behaviors. As shown in Figure 14h, when two synapses in series (presynapse 1 and 2) are triggered with 280 nm and 365 nm light spikes, respectively, the applying sequence of two light spikes will result in different postsynaptic current (PSC) due to the accumulation and dissipation effect of photo-generated carriers. Thus, the device can be used to demonstrate an interactive associative learning, namely Pavlov's classical conditioning experiment. However, if the light spikes are the same, a symmetric spike-time-dependent plasticity (STDP) can be observed by varying the time interval between the spikes applied on each synapse, indicating the device is capable to mimic fundamental behavior of Hebbian learning (as shown in Figure 14i). Moreover, the energy consumption of this artificial optoelectronic synapse device can be projected to 7 fJ by scaling down the active area, which may facilitate the development of optoelectronic machine vision systems. This work has revealed the potential of 2D metal oxides in multifunctional memristors. So far, the demonstrations in memristors mostly focus on proof of concepts rather than practical systems. Further researches are required in optimizing device performance, raising integration, improving system functionality, and developing integration process.

4.5. Potential device applications

2D metal oxides are enormously versatile and have great potential in various electronic and optoelectronic applications in addition to the mentioned above, such as solar cell, spintronics, and superconductor electronics.

4.5.1. Solar cell

The solar cells, or photovoltaic (PV) cells are excitonic devices that use light-adsorber to generate electric energy from solar light. The common basic configuration of a PV device, for example, perovskite solar cell, usually consists of a bottom transparent conductive oxide (TCO) electrode, electron transport layer (ETL), photoactive layer, hole transport layer (HTL) and a top metal electrode.[230] A "inverted" structure with interchange of ETL and HTL is also widely employed in solar cell. Metal oxide thin films have been employed to construct all-oxide solar cells, and also adopted as TCO electrode or charge transport layers in organic, perovskite, and dye-sensitized solar cells.[231] 2D metal oxide is highly expected to inherit the functionality of the thin film to achieve the above functional components in solar cells. However, there are few reports on 2D metal oxides in the application of solar cells, mainly due to the difficulties in their preparation. Recent studies have shown that the 2D metal oxides have great potential for flexible transparent electrodes.

ITO, as key TCO electrode for solar cells, has been used in industry for several decades, owing to the high conductivity, excellent transparency, minimal toxicity and good compatibility with various substrates. However, the brittle nature limits its use in future flexible electronics. To increase the flexibility and transparency of the ceramic material, reducing the thickness to only a few atoms is considered to be an effective approach.[92] In 2020, Datta et al.[29] have successfully prepared centimeter-scale ternary oxide 2D ITO at low-temperature by a liquid metal printing technology due to the high solubility of tin ions in the indium oxide.[232-233] The 2D ITO monolayer (~1.5 nm) featured polycrystalline semiconductor with bandgap of 3.9 eV, consisting of crystal domains with 20 nm average lateral size in varying orientations. The 2D ITO monolayer demonstrates a transmittance loss of only 0.4% across the visible spectrum and resistance of 69.6 kΩ sq^{-1}, which is 6.25 times more transparent but two orders of magnitude more resistive than monolayer graphene[234]. Interestingly, a bilayer ITO material can be achieved by applying a secondary printing technique on a monolayer sample, possessing a vdW spacing in between. The bilayer samples possess significantly lower resistance of 5.4 kΩ sq^{-1}, maintaining 99.3% transparency across the visible spectrum. The ITO

resistance was increased by less than 3.5% after 3,000 cycles, indicating the excellent mechanical stability of the flexible 2D ITO film. The same study also demonstrated a transparent capacitive touch screen prototype, which has a typical configuration of PET/2D ITO/glass/2D ITO with one back electrode and four front electrodes. The device realizes highly sensitive recognition of touch point location, enabling fully functional planar touch screen operation.

2D heterostructure superlattice is an alternative way to improve the conductivity of transparent electrode in addition to the atom substitution strategy (e.g., tin substitutes indium site in ITO). Ye et al.[74] demonstrated a scalable and high-speed roller-based continuous liquid metal printing technique for fabricating 2D oxide superlattices on various substrates, where the superlattices are prepared by stacking selected 2D oxides (SnO_x, SbO_x, AlO_x, and GaO_x) with InO_x. By optimizing the band alignment, defect concentration, and layer ratio in superlattice, the hetero-superlattices of InO_x/GaO_x films exhibited 100 times improvement in conductivity while maintained its high transmittance (> 98% in visible range). The high conductivity in the 2D superlattice are attributed to effective doping effect of GaO_x on InO_x in which the GaO_x with numerous oxygen vacancy could pin the Fermi-level closer to its conduction band at the interface with InO_x. Besides, the high transparency for visible light is originated from the wide bandgap and ultra-thin thickness feature. Taking the advantages of excellent conductivity, transparency and efficient printing process, 2D TCOs and their heterostructures are promising conductors for future flexible optoelectronic devices.

4.5.2. Spintronics

Spintronics, known as spin electronics, involve electron spin signals in addition to charge transport in traditional electronics, in which the functionalities of spintronic devices can be realized through spin manipulation, spin transport and spin-charge conversion. Spin signal, as an extra degree of freedom, can (partially) replace the function of charge signal in the spintronic devices, which can effectively reduce the charge leakage and Joule heat generated by charge transport in principle, thereby reducing energy consumption. Thus, the spintronics is promising for low power spin-logic devices and memory devices. A spintronic device is usually composed of magnetic and non-magnetic material thin layers, which has been mostly demonstrated in dilute magnetic semiconductors (DMS) and Heusler alloys. Owing to the unique physical properties, the emerging 2D magnets (e.g., CrI_3, VSe_2, $CrSe_2$, $Cr_2Ge_2Te_6$, $MnPSe_3$) and 2D heterostructures have been considered as potential magnetic building blocks for future spintronic devices.[26, 235-237] However, the challenges still remain in low intrinsic Curie temperatures, air instability, as well as the complexity of magnetic.

Recently, inspired by previous studies on dilute metal oxides (DMO),[25] Chen et al. has prepared a room-temperature ferromagnetic 2D graphitic $Zn_{1-x}Co_xO$ (gZCO) monolayer by doping Co atoms into a non-magnetic 2D vdW gZnO.[38] The 2D gZCO exhibits strong chemical stability in ambient conditions and tunable magnetism from paramagnet to ferromagnet by changing Co-doping levels. Although 2D gZCO has not been demonstrated in spintronic device, this work shows some potential advantages of 2D magnetic oxide materials, including high Curie temperature and high stability. Moreover, the studies on 3D DMO materials can provide valuable references for design and modulation of novel 2D magnetic oxide materials to extend the library of 2D magnets. Of course, advanced synthesis method is still urgently required to get high-quality 2D magnetic oxide crystal and rule out the possible contamination in the modulation process (e.g., doping, defect engineering).[25] Besides, some high-quality freestanding 2D oxide monolayers such as $BiFeO_3$,[44] $La_{0.7}Sr_{0.3}MnO_3$,[121] have been successfully obtained, but the further demonstrations in spintronic devices are still rare.

4.5.3. Superconductor electronics

Superconductor electronics are functional electronic circuits containing superconducting systems that could effectively utilize the unique characteristics of superconductivity below the critical temperature (T_c) to meet some extreme demands, such as single-photon detection and single magnetic fluxes manipulation.[238] Superconductor systems can achieve high speed low-power circuits and control of quantum bits (qubits), which can be integrated with CMOS control circuits at cryogenic temperature, indicating their great potential in supercomputing and quantum computing.[239-240] The emerging crystalline 2D superconductors can access superconductivity at the 2D limit, and therefore could unveil the unprecedented quantum phenomena that are different from the ultrathin disordered superconducting metal film.[241-242]

In particular, various 2D superconductors have been developed in 2D metal oxides, including 2D vdW complex metal oxide (e.g., $Bi_2Sr_2CaCu_2O_{8+x}$),[39, 243] 2D nanopatterned complex metal oxide ($YBa_2Cu_3O_{7-x}$),[27] interfacial 2D system (e.g., $La_{2-x}Sr_xCuO_4/La_2CuO_4$,[28] $LaAlO_3/SrTiO_3$[244]), and electric double-layer transistor (EDLT; e.g., $SrTiO_3$,[245] $La_{2-x}Sr_xCuO_4$[246]). The mechanisms of superconducting transition in these materials are still debated, thus, the critical temperature (T_c) is intuitive and important for practical applications. To get high-T_c, optimizing the doping level is a common and effective way. The T_c of monolayer $Bi_2Sr_2CaCu_2O_{8+x}$ (Bi-2212) with optimized the doping level is almost the same as that of the high T_c (~88 K) bulk counterparts. Varying the etching time in 2D nanopatterned $YBa_2Cu_3O_{7-x}$ can gradually change the phase state and T_c, while changing the top layer

thickness in the interfacial $La_{2-x}Sr_xCuO_4/La_2CuO_4$ superconducting system can tune T_c up to 50 K. However, stability is a critical issue for 2D superconductors. The exfoliated Bi-2212 monolayer is extremely sensitive to the environment, which requires well-protection, such as inert atmosphere at low temperature[39] or graphene protection layer.[243] In the future, seeking and characterizing high-T_c 2D materials and heterostructures could probably lead to interesting discoveries, where the fabrication and protection techniques is critical for scalable high-quality samples. Moreover, the demonstration and evaluation of their compatibility with the CMOS logic circuits is significant for further commercialization.

5. Conclusions and Outlook

With the continuous development of semiconductor technology, 2D metal oxide has made explosive and comprehensive progress toward future electronic and optoelectronic technology. In this review, we have summarized the recent advances in emerging 2D metal oxides from structures, synthetic methods, and interesting properties to various potential electronic and optoelectronic applications. We introduced several key factors of 2D metal oxide structure that should be taken into consideration in the researches, such as crystal phase effects (forms with variable metal valence state, polymorphism, *etc.*), crystalline and defects (anisotropy, point defects, and grain boundary), thickness effects. In recent years, numerous synthesis methods have been adopted for the preparation of 2D metal oxides including mechanical exfoliation, liquid phase method, vapor phase deposition and native oxidation on metal source (liquid metal, polished metal, and 2D metal chalcogenides). In terms of the current progress, the vapor phase deposition (especially MBE) exhibits greater potential for high quality and scale-up synthesis of 2D metal oxides, and precisely controllable oxidation of metal source can bring new insight into new 2D metal oxides. The application of reported 2D metal oxide materials in electronics and optoelectronics is still in infancy, which are mainly used in FETs (as channel layer, high-κ dielectric layer and other functional layer), photodetectors as active layer. Combining the nature of metal oxide and state of recent progress, the 2D metal oxides have great prospects for developing ultrathin p-type 2D semiconductor with high stability and mobility, excellent high-κ dielectric with sub-nanometer EOT and functional buffer layer, which are complementary with common 2D materials. Besides, the 2D metal oxides have mainly advantages of high responsivity and good selectivity in UV detection due to their intrinsic wide bandgap feature, while their detection range can extend from deep UV to midinfrared with the coupling of other photo-induced effects. Nevertheless, the 2D metal oxides have also been

51

WILEY-VCH

investigated in piezotronics/piezo-phototronics, memristor derived artificial synapses, as well as potential applications in solar cell, spintronics and superconducting devices.

Despite that they have shown many intriguing performance and advantages mentioned above, the 2D metal oxides studies still have some challenges to resolve for the future use in electronics and optoelectronics. Some reasonable views on the major challenges and research trends are provided as follows.

For exploring novel structure, on the one hand, with the development of scientific theory, researchers can predict the structure and properties of 2D materials through computer software simulation like first-principles calculations.[247] For example, Guo et al.[57] systematically screened eighteen functional monolayer metal oxides, which are predicted to possess chemical stability, appropriate bandgap from 1.22 to 6.48 eV, high carrier mobility (8540 cm^2 V^{-1} s^{-1}), and outstanding absorption in the UV region. Therefore, the efforts should be devoted into the experimental synthesis of the simulated materials before further application study. Meanwhile, the development of thermodynamics and kinetics simulations are urgently needed to guide the experiment of synthesizing 2D metal oxides that are still in the simulation library. On the other hand, with the progress of synthesis equipment, researchers can realize atomically precise fabrication in developing atomic-level materials.[248] Some novel 2D metal oxide crystal structures have been obtained, such as gZnO,[53] h-BeO,[55] and h-TiO_2,[32] which possess different atomical layered structures that are different from the their conventional counterparts. These new crystal structures often have some fascinating optical or electrical properties, which can be used for high performance devices. For example, few-layer hexagonal TiO_2 (h-TiO_2) demonstrates a large hole mobility (950 cm^2 V^{-1} s^{-1}) at room temperature.[32] However, the research on novel 2D metal oxide materials (at least hexagonal MnO, Fe_2O_3, CoO, Ni_2O_3 and Cu_2O) is still at the primary phase of structure.[32] Thus, further investigation of novel 2D metal oxides should be carried out in electronics and optoelectronics according to the their characteristics. Moreover, the stability of novel 2D metal oxides is crucial for their application in devices and device operational stability. The fragility or stability of 2D metal oxides can be understood as the mechanical and chemical stability under environmental or operational conditions, which faces following challenges, such as mechanical fracture, metal valence change, phase transition, defects formation, and even complete structure failure. Environmental stability is crucial for the practical usage of 2D metal oxides. The corrosion of 2D metal oxides usually suffer from the potential redox reaction in the presence of O_2 and H_2O, or H_2, which mainly affect valence state of metal ions and thus the coordination number and symmetry of chemical bonding.

Therefore, environmentally fragile 2D metal oxides could be covered with suitable protective materials, such as graphene,[243] hexagonal boron nitride,[249] or self-assembly monolayer (SAM).[250] For operational stability, the 2D metal oxides in electronic and optoelectronic devices may be subjected to multi-fields including electric, thermal (high temperature or cryogenic condition), electromagnetic (e.g., light illumination) and elastic field. These physical field could possibly damage the structure of 2D metal oxides. Thus, discovery of new 2D metal oxides should also take the factors of their stability in corresponding operational environment into considerations. The endurance test of the device based on 2D metal oxides is necessary in the experimental studies. In addition, the computational methods such as first-principles calculations can play a key role in the prediction of the operational structure stability under a simulated physical environment.

For developing advanced synthesis method, the growth process of a single-crystalline structure in large area has become a serious bottleneck for scaling up applications of 2D materials.[19] It seems that the defects such as vacancies and grain boundaries cannot be completely eliminated in large area. However, the defect concentration should be controlled to extremely low level and has negligible influence on the device performance. Currently, native oxidation on metal source (liquid metal, polished metal) exhibits considerable potential for 2D metal oxide with large area but uncertain integrity and crystallinity. The vapor phase deposition are promising for wafer-scale single crystal growth of 2D materials, by which several 2D materials, like Graphene,[251-253] h-BN,[254] and TMDCs,[255-256] are successfully prepared. Meanwhile, wafer-scale molecular crystal Sb_2O_3 film is also achieved through thermal vapor deposition, but most of single crystalline 2D metal oxides are still in the state of flakes with micrometer lateral size by vapor phase. Those succeeded cases, especially wafer-scale synthesis of TMDCs, afford lessons for large scale single crystal synthesizing 2D metal oxides.[19] Thus, wafer-scale 2D metal oxides may be achieved by unidirectional alignment and seamless stitching of 2D domains or conversion of orient precursor.[255, 257] Liquid metal approach could be an efficient way for large scale 2D metal oxide synthesis beyond vapor phase deposition, but the unity, regularity, and repeatability needs to be improved.[143] A fully automated production line with super clean and controllable atmospheric environment can be beneficial for achieving large-area high quality 2D metal oxides through liquid metal approach. However, the fundamental mechanism indicates that only a few of metal oxides that meet certain conditions can form 2D morphology on the liquid metal surface.[168] Thus, further study is also necessary to expand the types of 2D metal oxides that synthesized by liquid metal method. In addition to large area preparation of stoichiometric 2D metal oxides, the non-stoichiometric form with desired defects is

also of great interest for property modulation and subsequent applications.[39] A pre-designed growth condition or a post-treatment process can be adopted to tuning the defective level.

For deepening and widening applications, the research on 2D metal oxides in previous works stays at primary stage of prototype device demonstration, although it covers the applications including FETs, photodetectors, piezotronics, transparent electronics, memristor derived artificial synapses. However, 2D metal oxides has shown more functionalities, such as ferromagnetic at room temperature[38] and high T_c superconducting behavior.[39] Therefore, further systematic and in-depth researches are needed. Moreover, extending the types of devices based on 2D metal oxides are also necessary for finding their killing applications in the electronics and optoelectronics fields. As a general idea, stacking 2D materials as atomic-scale Lego plays a significant role.[1] Thus, vdW integration of 2D metal oxides with other materials can be expected to change or enhance the performance of the devices, as well as widening the application of 2D metal oxides, such as light-emitting diodes, inverters, and other logic circuits. The potential candidate materials include 0D materials (e.g., C_{60}), 1D materials (e.g., quantum wire), 2D materials (e.g., TMDs, BP and graphene) and 3D materials (e.g., transfer electrodes, bulk semiconductors). The vdW gap widely exist at the interfaces of the stacking 2D contacts, of which thickness mostly vary in the range of 0.1~0.3 nm.[258] The vdW gap can play important role in the device applications. For example, in metal/2D semiconductor contact, the vdW gap poses a tunnel barrier for carrier transport (hopping and/or tunneling) in a unreacted contact interface, decreasing the carrier injection efficiency, but an ultra-thin vdW gap can significantly reduce the negative effect.[17, 177, 259-260] In dielectric/2D semiconductor contact, vdW gap can act as an effective tunnelling barrier that reduces the carrier tunnelling probability and thus suppresses the gate leakage currents.[33, 182] In semiconductor/semiconductor contact, a typical 2D carrier gas could be introduced at the interface to realize high carrier mobility in the device.[201] Thus, vdW integration can open a new era of material and device physics, which can possibly achieve vdW stacking materials with completely new functionalility and develop novel devices with unprecedented performance. Notably, the reliable and clean transfer process for large-area 2D metal oxides is the prerequisite for 2D stacking, which can be inspired from a modified roll-to-roll transfer of large-area graphene.[261] Besides, in-plane heterostructure, like 1T' $MoTe_2$-2H $MoTe_2$ homojunction,[262] is also interesting for 2D devices. The 2D metal oxides feature structure diversity that benefits the construction of in-plane heterostructures, for example, SnO_2-SnO homojunction and α-Sb_2O_3-β-Sb_2O_3 homojunction. These homojunctions may bring unexpected and surprising performance to the devices. In addition, Controlling the relative twist angle between successive layers in 2D materials offers an approach to manipulating their electronic and

WILEY-VCH

optoelectronic properties.[263] Twisted 2D metal oxides bilayers also can obtain new phenomena, for example, high-temperature topological superconductivity in twisted copper oxides,[264] configurable phonon polaritons in twisted α-MoO$_3$.[61-62] With the continuous development of 2D electronics and optoelectronics, adding 2D metal oxides to the 2D toolkit can provide an effective way to solve 2D challenges.
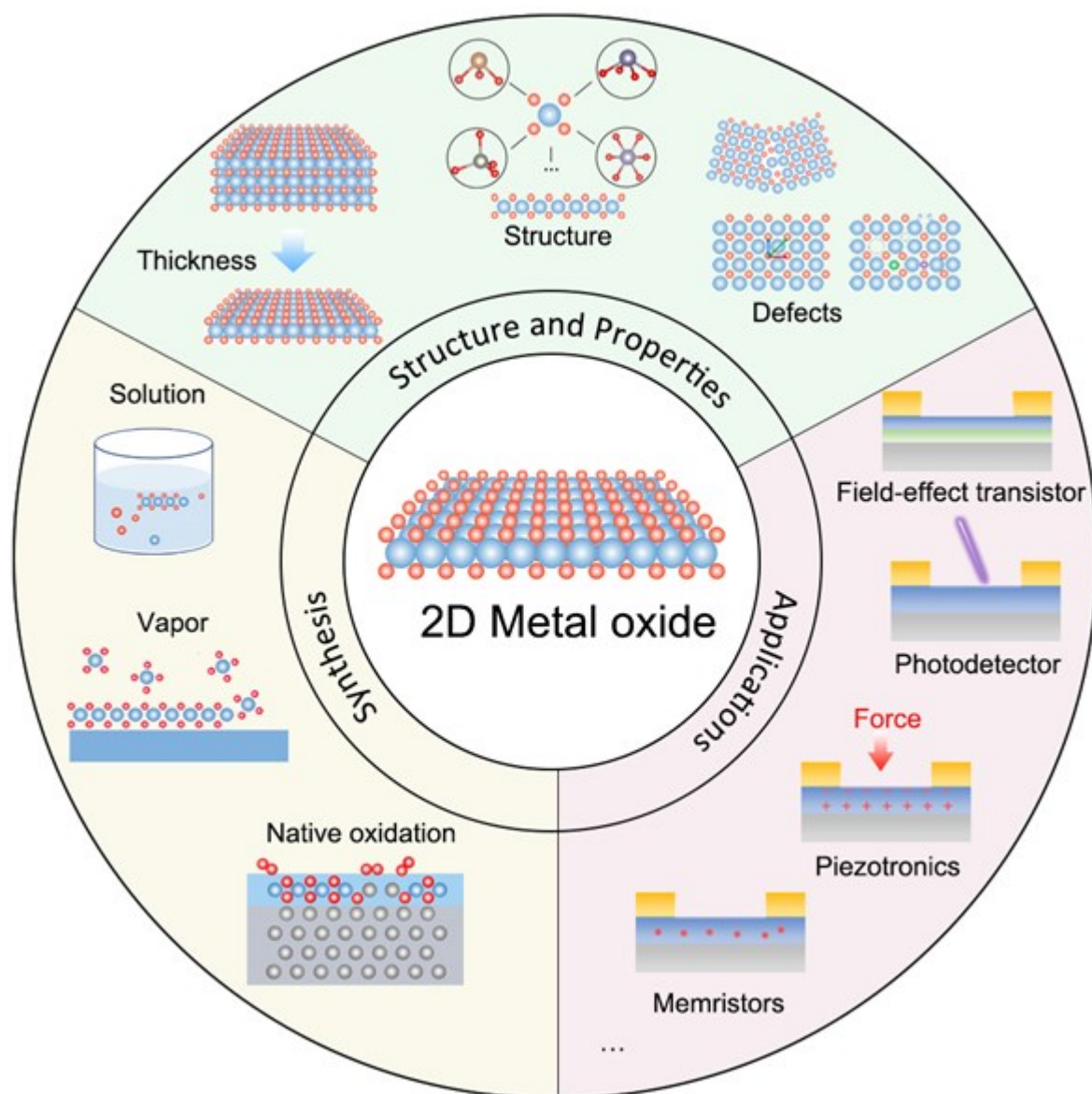
Figure 1. Schematic overview of structure-properties, synthesis strategies and electronic/optoelectronic applications of 2D metal oxides.
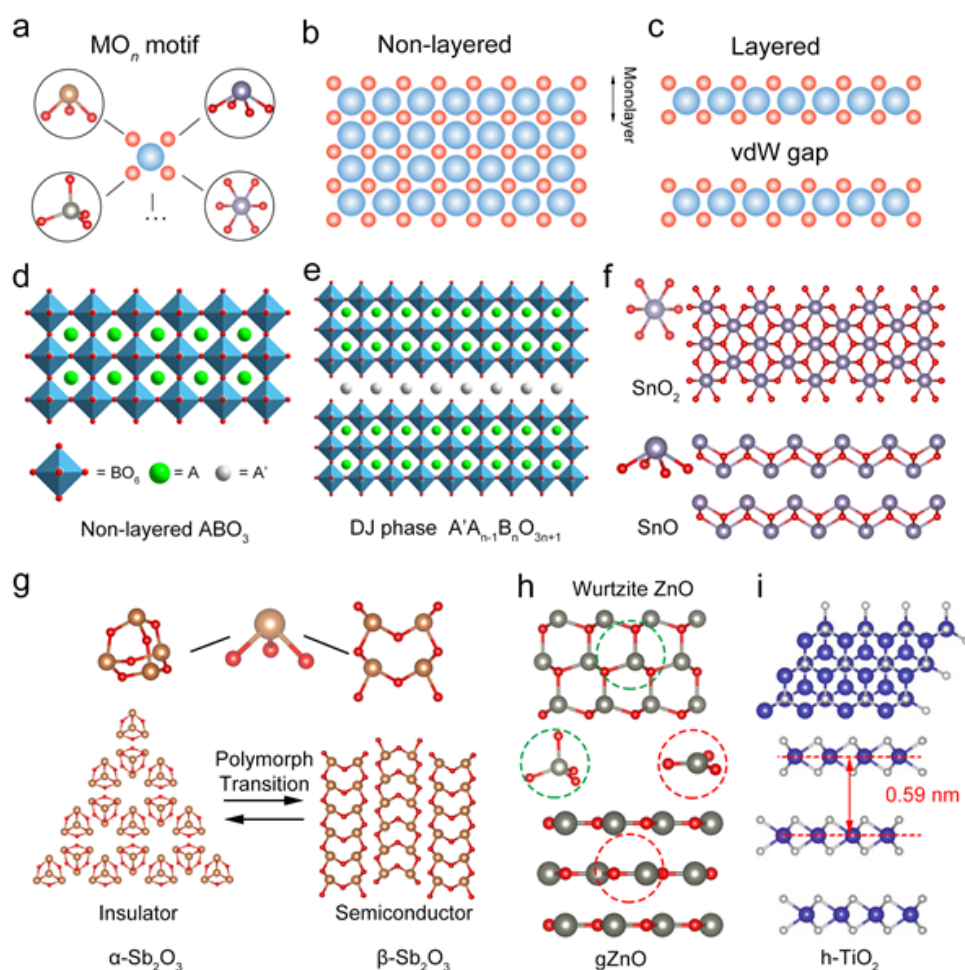
Figure 2. Structure diversity of 2D metal oxides. a) various MO_n motifs in 2D metal oxides, M for metal, O for oxygen, n is the coordination number of oxygens around metal center in the range from three to six. b) 2D metal oxide consists of MO_n motifs linked by corner, edge and face sharing to form non-layered and layered structure. d-e) 2D perovskite oxide as typical complex 2D metal oxide: d) non-layered ABO_3 type, e) Layered DJ phase $A'A_{n-1}B_nO_{3n+1}$. f) Structure illustration of n-type semiconducting SnO_2 and p-type semiconducting SnO as a representative case of metal valence affecting the structures and properties of 2D metal oxides. g) Structure illustration of insulating α-Sb_2O_3 and semiconducting β-Sb_2O_3 as a representative case of polymorphism affecting the structures and properties of 2D metal oxides. h-i) Novel layered 2D structure of conventional metal oxide, opening a hope for the exploration of novel 2D metal oxides: h) Layered structure of graphene-like ZnO (gZnO), which is different from conventional wurtzite ZnO, i) hexagonal TiO_2 (h-TiO_2). i) Reproduced with permission.[32] Copyright 2021, Nature Publishing Group.
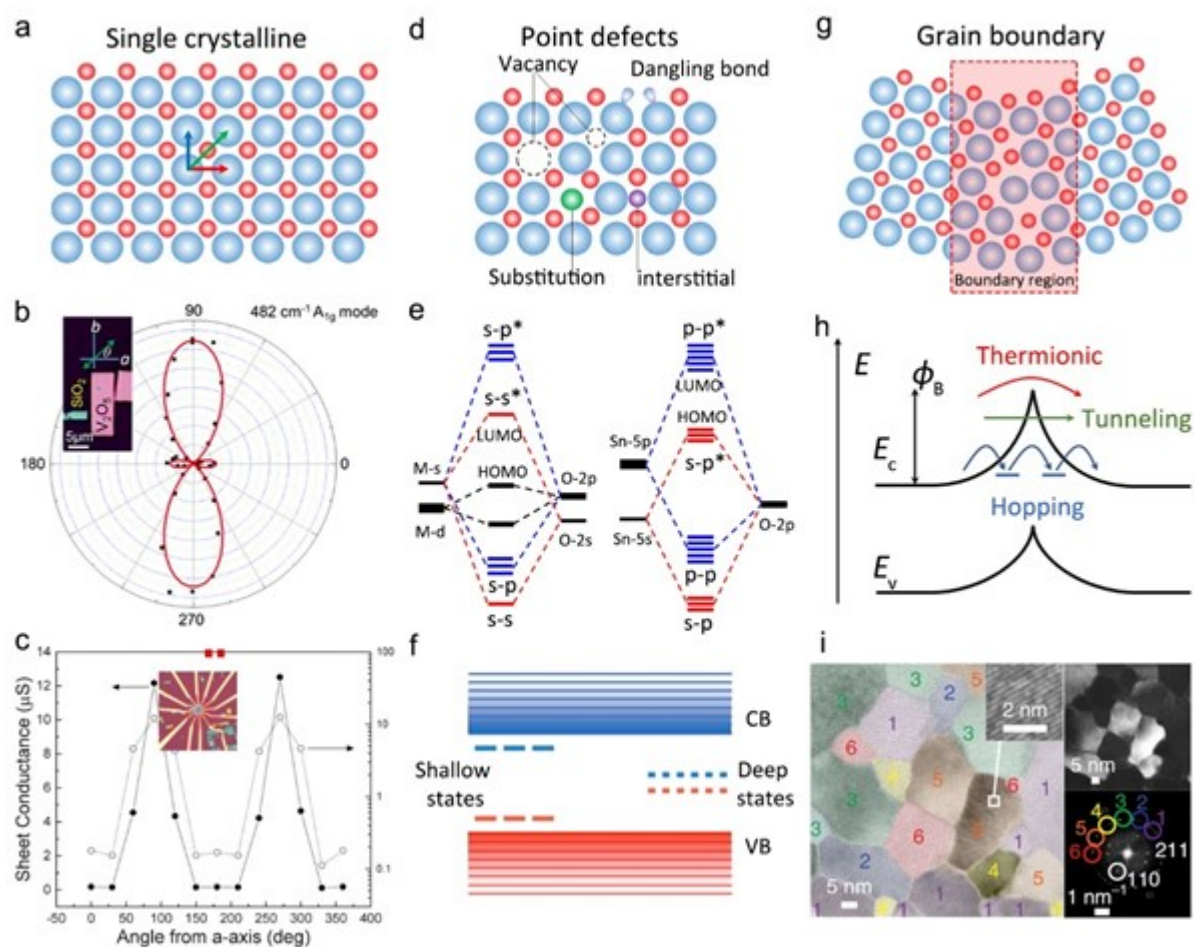
Figure 3. a) Schematic illustration of anisotropy in monocrystalline 2D metal oxides. b) Intensity of the A_{1g} mode at 482 cm^{-1} at different angle θ for parallel polarization. The inset demonstrates the optical image of the V_2O_5 flake. The green dot shows the location of the laser spot. c) Plot of four-terminal sheet conductance illustrated in linear (solid symbols) or log (open symbols) scale *vs* angle from principal *a* axis. The inset shows the optical image of the V_2O_5 device. d) Schematic illustration of various point defects in 2D metal oxides, such as vacancy, substitution, interstitial and dangling bonds. e) molecular orbital diagrams at particular *k*-points of the Brillouin zone: the Γ point in In_2O_3, ZnO, and SnO_2 (left) and the Γ point in SnO (right), only the relevant bonding orbitals (s-s, s-p, p-p) and anti-bonding orbitals (s-s*, s-p*, p-p*) are depicted for the sake of clarity. f) Schematic defects induced shallow states and deep states in the bandgap. g) Schematic illustration of grain boundary defects in 2D metal oxides. h) Schematic illustration of charge transport across grain boundary through thermionic, tunneling and hopping. i) HRTEM image of the optimized 2D ITO nanosheet. The colour code highlights the crystal orientation with grain boundary. b-c) Reproduced with permission.[58] Copyright 2017, American Chemical Society. e) Reproduced with permission.[65] Copyright 2016, AIP Publishing. i) Reproduced with permission.[29] Copyright 2020, Nature Publishing Group.
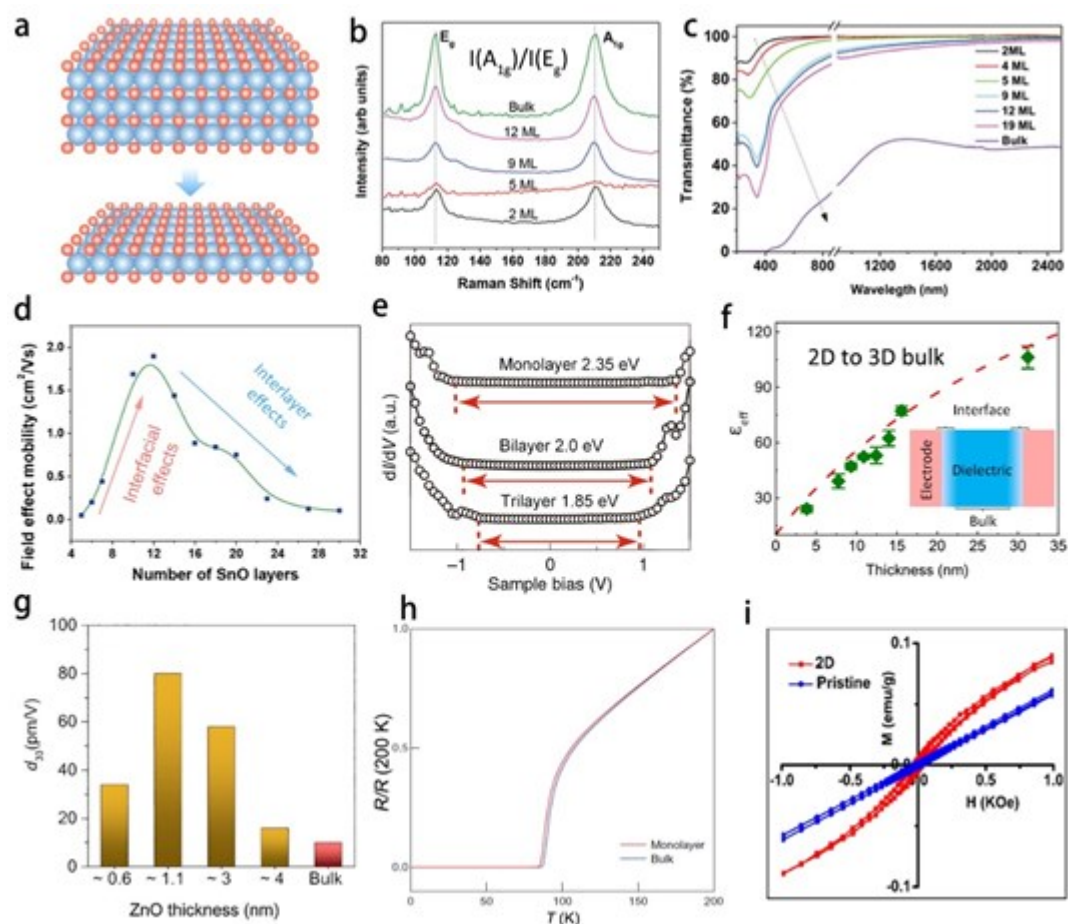
Figure 4. a) Schematic demonstration of thickness effect in 2D metal oxide. b) Raman spectra for SnO (bulk to 2-monolayer), displaying no shift in the peak positions, but variation of integrated intensity ratio between A1g and Eg peaks. c) Optical transmittance of SnO with various thicknesses. d) Variation of mobility as a function of the channel layer thickness. e) Bandgap variation as a function of the layer numbers in h-TiO$_2$. f) ε_{eff} with respect to the SrTiO$_3$ thickness. The red dashed lines denote the fitted curves by means of the 'dead layer' model (as shown in Inset). g) Experimentally measured behavior of d_{33} values with respect to ZnO sheet thickness. h) Temperature-dependent resistance of a monolayer Bi-2212 (red) and bulk counterpart (blue). i) Room-temperature *M-H* loops of the pristine ilmenite and 2D ilmenene. b-d) Reproduced with permission.[163] Copyright 2016, Wiley-VCH GmbH. e) Reproduced with permission.[32] Copyright 2021, Nature Publishing Group. f) Reproduced with permission.[33] Copyright 2022, Nature Publishing Group. g) Reproduced with permission.[37] Copyright 2020, Elsevier. h) Reproduced with permission.[39] Copyright 2019, Nature Publishing Group. i) Reproduced with permission.[89] Copyright 2018, American Chemical Society.

WILEY-VCH

60
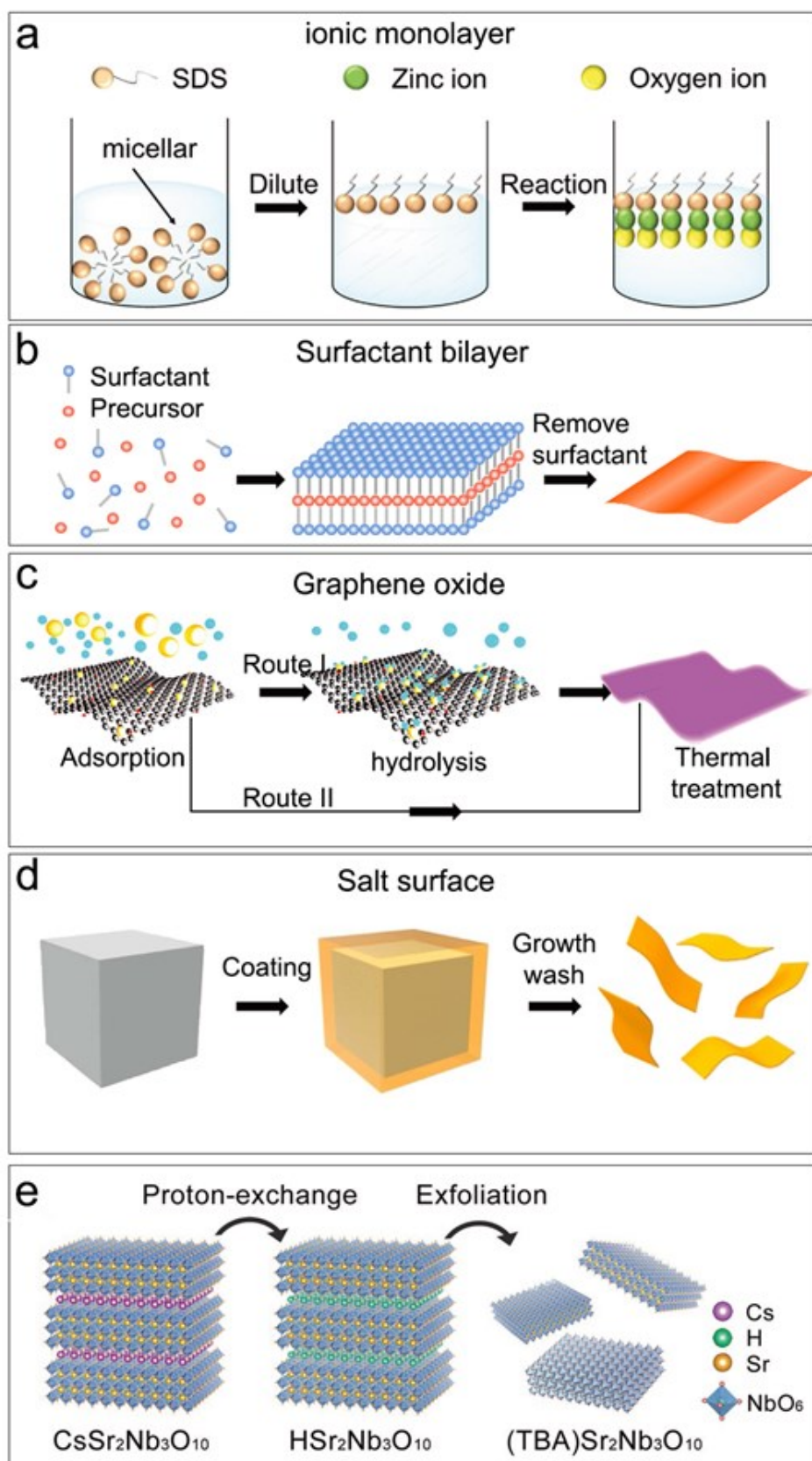
Figure 5. Solution processed synthesis of 2D metal oxide. Bottom-up method with various templates: a) Schematic illustration of SDS assist-synthesized 2D ZnO nanosheets. b) Schematic illustration of the 2D metal oxide synthesis at surfactant bilayer surfaces. c) Schematic illustration of the 2D metal oxide synthesis at graphene oxide surface. Route I: hydrolysis; Route II: direct thermal treatment. d) Schematic illustration of the 2D metal oxide synthesis at salt surface. Top-down method: e) Schematic illustration of the fabrication process of $Sr_2Nb_3O_{10}$ nanosheets by proton-exchange and exfoliation processes from bulk precursor $CsSr_2Nb_3O_{10}$. a) Reproduced with permission.[35] Copyright 2020, Wiley-VCH GmbH. c) Reproduced with permission.[109] Copyright 2017, Wiley-VCH GmbH. d) Reproduced with permission.[110] Copyright 2016, Nature Publishing Group. e) Reproduced with permission.[30] Copyright 2020, Wiley-VCH GmbH.
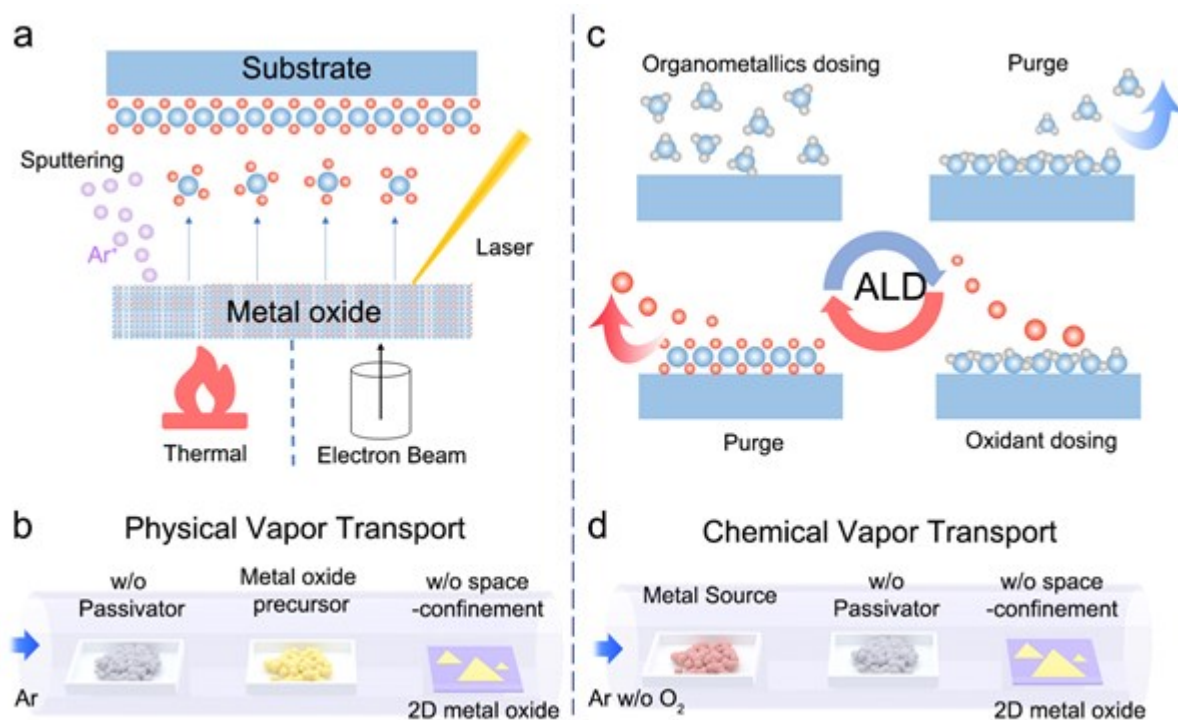
Figure 6. Vapor phase preparation of 2D metal oxides. a) Schematic illustration for PVD growth of 2D metal oxide including thermal evaporation, sputtering, electron beam evaporation and PLD. b) Schematic illustration of the physical vapor transport. c) Schematic illustration for ALD of 2D metal oxide atomic layer deposition. d) Schematic illustration for chemical vapor transport.
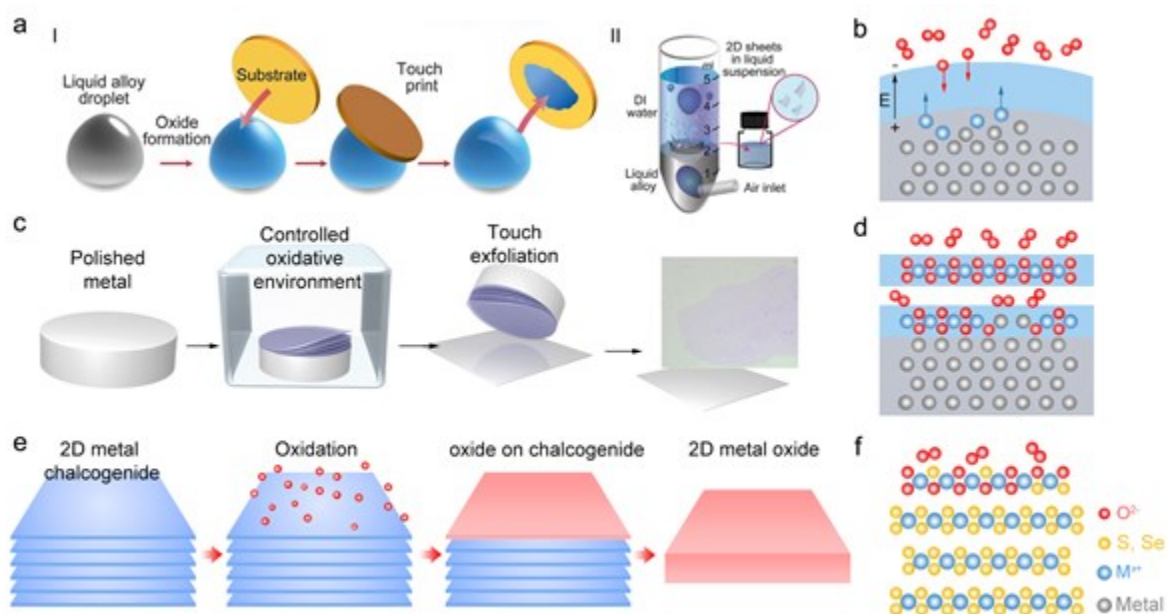
Figure 7. a) Schematic illustration of the vdW exfoliation technology. The pristine liquid metal droplet is initially exposed to an oxygen-containing environment. (I) Touching the liquid metal with a proper substrate allows transfer of the interfacial oxide layer and (II) gas injection method. b) Schematic illustration of Cabrera-Mott oxidation occurring at the liquid metal surface in the presence of oxygen to form 2D oxide skin. c) Schematic illustration of layered oxide growth and mechanical exfoliation approach. d) Schematic illustration of controllable oxygen diffusion and bonding with metal ion to form layered 2D metal oxide on the surface of polished metal. e) Schematic representation of 2D metal oxide derived from 2D metal chalcogenide *via* oxygen diffusion and ion exchange. f) Schematic illustration of oxygen diffusion and exchange with chalcogens ions to form 2D metal oxide on the 2D metal chalcogenide surface. a) Reproduced with permission.[133] Copyright 2017, AAAS. c) Reproduced with permission.[32] Copyright 2021, Nature Publishing Group.
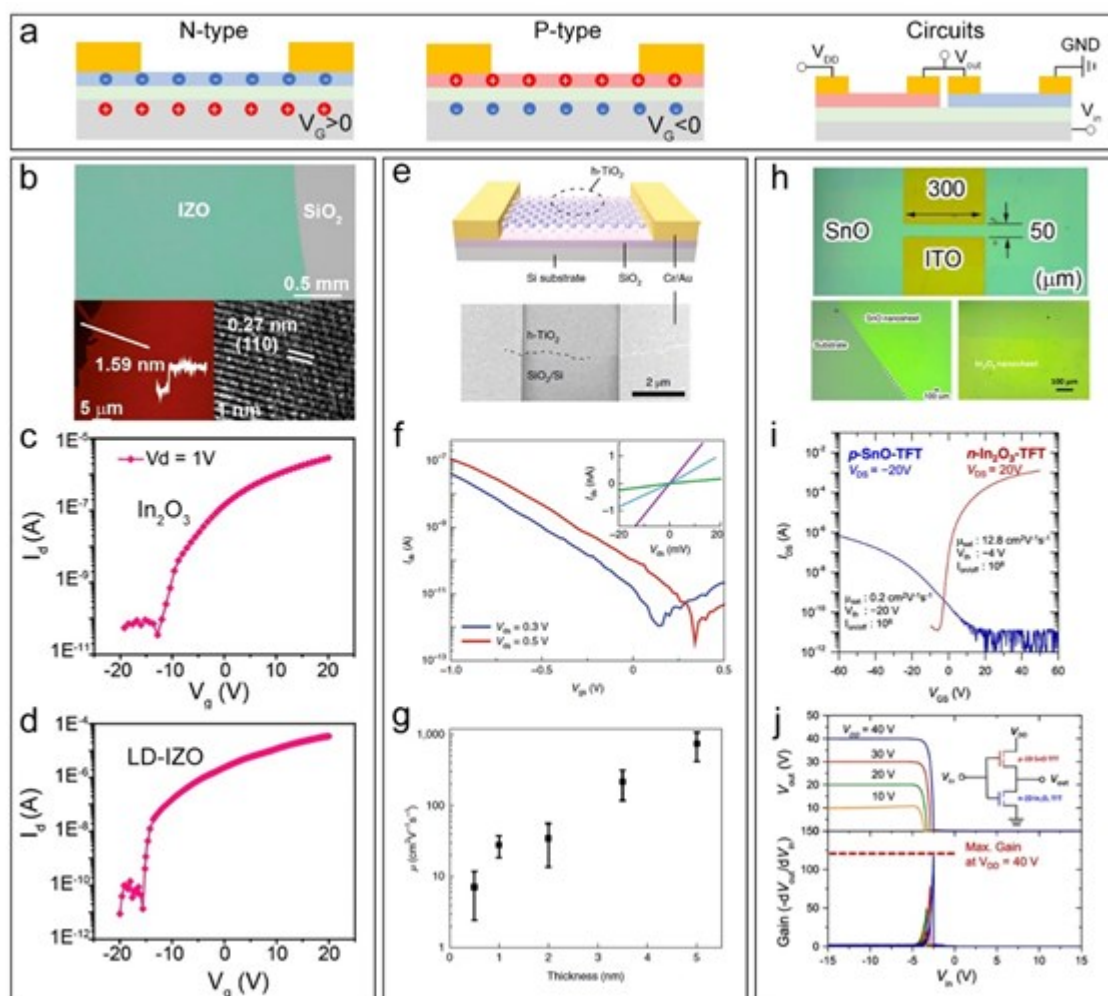
Figure 8. a) Schematic illustration of n-type FET (left), p-type FET (middle) and inverter circuit (right) based on 2D metal oxides. b) Morphology and structural characterization of 2D IZO sheets. c) I_{ds}-V_{gs} characteristics of 2D In$_2$O$_3$ transistor. d) I_{ds}-V_{gs} characteristics of 2D low doping level IZO transistor. e) Perspective view and the corresponding SEM image of a 2D h-TiO$_2$-based FET. f) I_{ds}-V_{gs} characteristics of a 1-nm thick h-TiO$_2$ FET at fixed V_{ds}; inset: I_{ds}-V_{ds} characteristics for low V_{ds} range. g) Mobilities with respect to the thicknesses of 2D h-TiO$_2$. h) Optical microscopy image of ultrathin SnO TFTs (top) and 2D SnO (bottom-left) and 2D In$_2$O$_3$ (bottom-right). i) I_{ds}-V_{gs} characteristics for the p-SnO TFT with V_{ds} = -20 V and n-In$_2$O$_3$ FET at V_{ds} = 20 V. j) VTC and the corresponding voltage gains of the p-SnO/n-In$_2$O$_3$ inverter. Inset: the schematic illustration of the inverter circuit. b-d) Reproduced with permission.[23] Copyright 2022, Nature Publishing Group. e-g) Reproduced with permission.[32] Copyright 2021, Nature Publishing Group. h-j) Reproduced with permission.[46] Copyright 2021, American Chemical Society.

Figure 9. a) Capacitances of parallel electrodes with 2D metal oxide as the insulating material at low frequency, from which the relative dielectric constant (ε_r) of the 2D metal oxide can be determined. Inset: schematic illustration of the devices for capacitance measurements. b) Leakage and breakdown measurement of 2D metal oxide. Horizontal red lines mark the limits of leakage current for diverse integrated circuits. Inset: schematic illustration of the measurement device. c) Schematic illustration of band diagram of a 2D metal oxide dielectric/semiconductor channel stack. ΔE_C and ΔE_V refers to the conduction and valence band offset. d) Schematic of transfer characteristics of 2D FET with 2D metal oxide as gate dielectric, showing SS (V_{th} is threshold voltage). Inset: schematic of the 2D FET device showing the density of interface states D_{it}. e) Band diagram depicting the alignment of the band gaps of typical insulators in 2D FETs. f) Schematic illustration of native 2D metal oxide on 2D metal chalcogenide with clean interface. g) Molecular crystal structure of Sb_2O_3 demonstrating the (111) plane and the structure of the ultrasmall molecule without dangling bond. h) Typical cross-sectional STM topography showing the heterostructure of transferred $SrTiO_3$ membrane onto Si (100) substrate with vdW interface. f) Reproduced with permission.[182] Copyright 2019, Nature Publishing Group. g) Reproduced with permission.[34] Copyright 2021, Nature Publishing Group. h) Reproduced with permission.[33] Copyright 2022, Nature Publishing Group.

Figure 10. Other roles of 2D metal oxides in FET, tunneling layer, doping layer, passivation/protection layer. a) Schematic illustration of the metal/buffer/2D structure, with possible buffer layers graphene, h-BN, NbS_2, and MoO_3. b) Densities of states of Pt(111) (left), bilayer-MoO_3 (middle), and MoS_2 (right). In a Pt/bilayer-MoO_3 /MoS_2 multilayer, the Fermi level is pinned at the bottom of the MoO_3 conduction band and at the top of the MoS_2 valence band. c) Schematic illustration of WSe_2/MoO_3 FET. d) Transfer characteristics of bare WSe_2 (blue line) and WSe_2/MoO_3 (red line) FET, indicating a hole doping effect of MoO_3. e) Optical microscopy and AFM images of a WS_2/Ga_2O_3 heterostructure (scale bar sizes: 200, 40 and 5 µm). f) PL spectra of monolayer WS_2 and WS_2/Al_2O_3 on SiO_2 (left); WS_2/hBN/Al_2O_3 and WS_2/Ga_2O_3/Al_2O_3 on SiO_2 (right). g) Schematics of Y_2O_3 buffer layer in MoS_2 FET. h) The band activation energy E_a and hopping energy E_h as a function of I_{ds} before and after the top-gate deposition. a-b) Reproduced with permission.[196] Copyright 2016, WILEY-VCH GmbH. c-d) Reproduced with permission.[200] Copyright 2020, WILEY-VCH GmbH. e-f) Reproduced with permission.[143] Copyright 2020, Wiley-VCH GmbH.
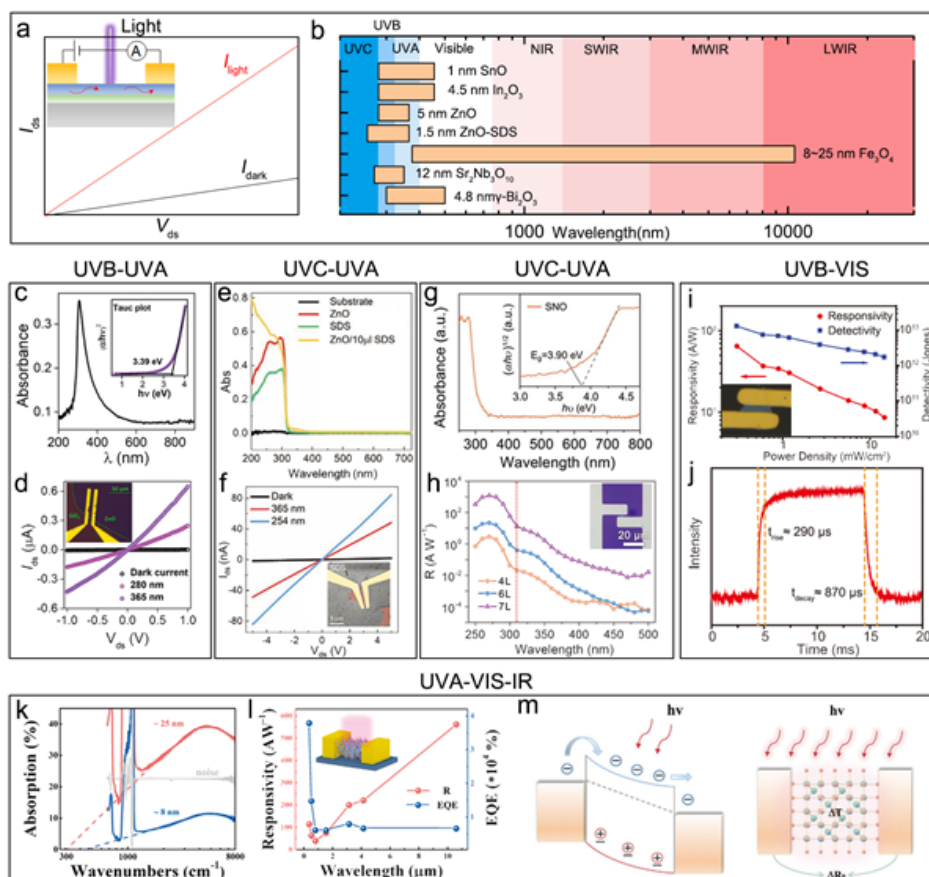
Figure 11. a) Photodetector based on planar metal-semiconductor-metal (MSM) configuration with photoconductive effect. Inset: schematic illustration of MSM photodetector. b) Summary of reported 2D metal oxide-based photodetector for different wavelength. UVC (200 to 280nm), UVB (280 to 315nm), UVA (315 to 400 nm), Visible (400 to 750 nm), Near-infrared NIR (0.75 to 1.4 µm), Short-wavelength infrared (1.4 to 3 µm), Mid-wavelength infrared (3 to 8 µm), Long-wavelength infrared (8-15 µm). c) The UV-vis-NIR spectra of liquid metal printed 2D ZnO nanosheets. Inset: Tauc plot extracted from the absorption spectrum. d) The $I-V$ characteristics under dark and UV illumination (3 mW cm^{-2}). Inset: Optical microscopy image of the 2D ZnO based photodetector. e) The UV–vis spectra of the PET substrate, ZnO nanowires, SDS without ZnO, and solution processed 2D ZnO-SDS. f) The photocurrent under UV illumination at 365 nm (76 µW cm^{-2}) and 254 nm (16 µW cm^{-2}). Inset: SEM images of 2D ZnO-SDS based photodetector. g) UV–vis absorption spectrum of liquid-exfoliated perovskite SNO. Inset: the corresponding Tauc curve. h) The responsivity of SNO nanosheets with numerous thicknesses. i) Light intensity dependent R and D^* of 2D γ-Bi$_2$O$_3$ based photodetector under 365 nm laser. j) Rise curve (rising time 290 µs) and decay curve (decay time 870 µs). k) Infrared absorption spectra of 2D Fe$_3$O$_4$ nanosheets. l) R and EQE of 2D Fe$_3$O$_4$ based photodetector in the range from 375 nm to 10.6 µm. Inset: schematic diagram of the 2D Fe$_3$O$_4$-based photodetector. m) Schematic illustration of the photo-induced bolometric effect and photoconductive effect. c-d) Reproduced with permission.[42] Copyright 2021, WILEY-VCH GmbH. e-f) Reproduced with permission.[35] Copyright 2020, Wiley-VCH GmbH. g-h) Reproduced with permission.[30] Copyright 2019, Wiley-VCH GmbH. i-j) Reproduced with permission.[50] Copyright 2021, Wiley-VCH GmbH. k-m) Reproduced with permission.[36] Copyright 2020, Wiley-VCH GmbH.
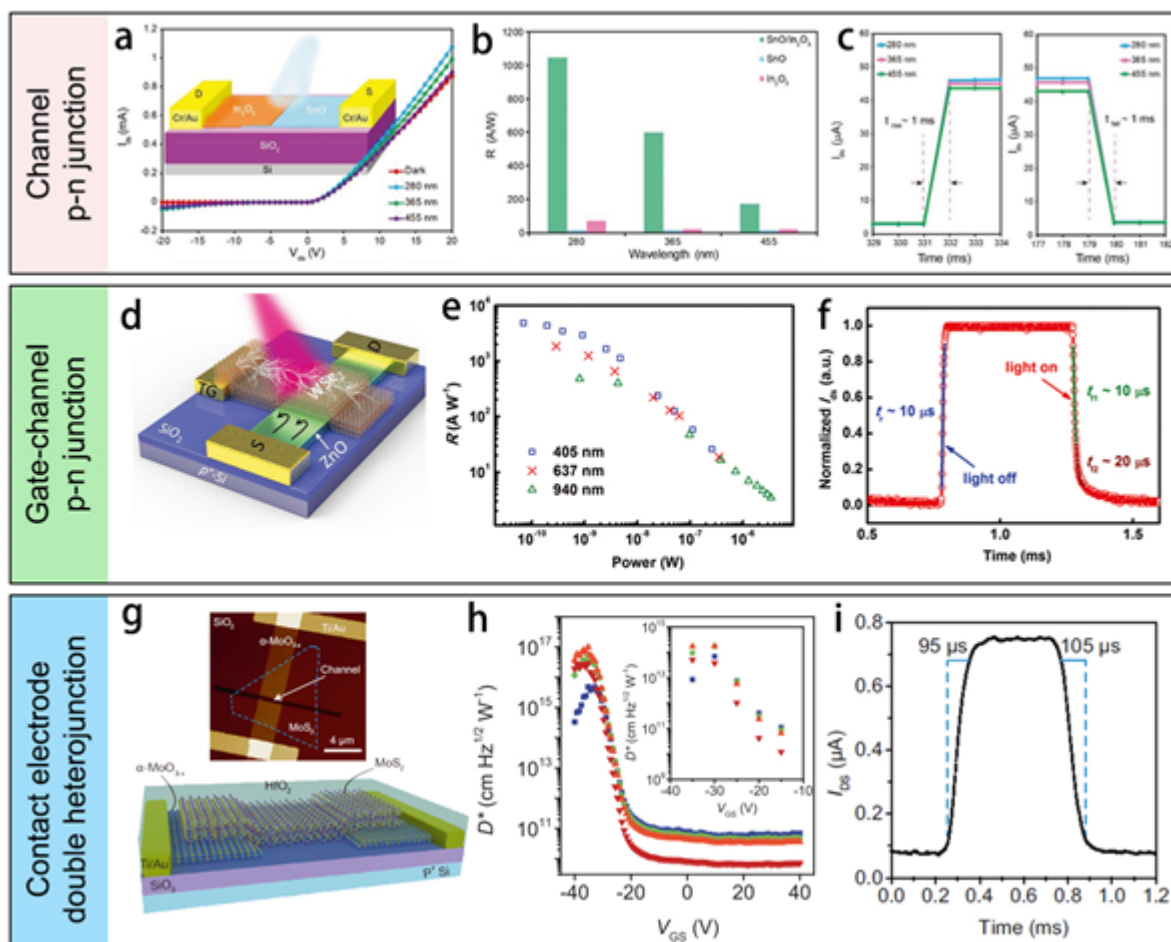
Figure 12. a) The I_{ds}-V_{ds} curves of the 2D SnO/In$_2$O$_3$ heterostructure under dark and light illumination. Inset: schematic illustration of the device. b) R of SnO/In$_2$O$_3$ heterostructure, SnO and In$_2$O$_3$ devices for different light illumination. c) The photocurrent responses with respect to time for the 2D SnO/In$_2$O$_3$ photodetector under diverse light illumination. d) Structure of WSe$_2$-ZnO LJFET with operating light illumination. e) R as a function of light power. f) Temporal response of the device with a single modulation cycle (rise time: ~10 μs, fall time: a fast component of ~10 μs and a slow component of ~20 μs). g) Schematic illustration of the α-MoO$_{3-x}$/MoS$_2$/α-MoO$_{3-x}$ phototransistor. Inset: AFM image of the device. h) V_{gs}-dependent D^*. i) Response speed of the phototransistor (rise time: 95 μs, fall time: 105 μs). a-c) Reproduced with permission.[136] Copyright 2019, Wiley-VCH GmbH. d-f) Reproduced with permission.[212] Copyright 2019, WILEY-VCH GmbH. g-i) Reproduced with permission.[213] Copyright 2021, Nature Publishing Group.
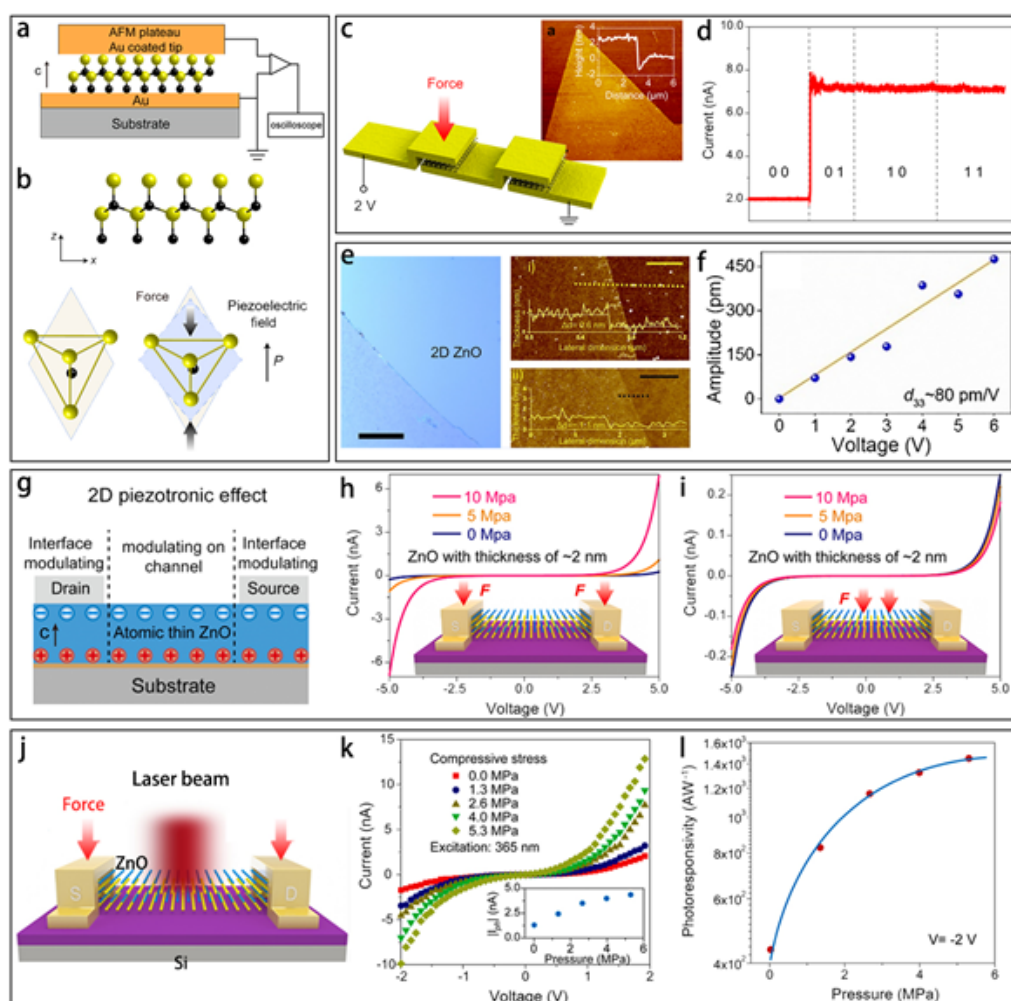
Figure 13. a) Schematic illustration of the ultrathin vertical piezotronics transistor with AFM measurement. b) Illustration of strong out-of-plane piezoelectricity in ZnO. c-d) Stress-gated OR logic gates formed by a series of piezotronic transistors. c) OR logic gate with one force on and d) the measured output currents for the "01" state. e) Optical image of the ZnO sheet, scale bar: 100 μm (left) and AFM images of ~0.6 nm thick ZnO sheets, scale bar: 500 nm and ~1.1 nm thick ZnO sheet, scale bar: 4 μm (right). f) Slope showing the largest d_{33} slope of 80 ± 0.8 pm/V in optimized ZnO thickness (~1.1 nm). g) Schematic illustration of ZnO based planar piezotronic device with metal/semiconductor interface modulating and channel modulating. h-i) Theoretically calculated I-V characteristics of ZnO devices with Schottky contacts. Transfer characteristics of 2 nm ZnO devices under 10 MPa, 5 MPa and 0 MPa applied at: h) metal-semiconductor contacts and i) transport channel. j) Schematic illustration of piezo-phototronic effect enhanced ZnO photodetector. k) Transfer characteristic of the ZnO device under different pressure applied at metal-semiconductor contacts under illumination (10 μW cm^{-2}). Inset: the photocurrent with respect to applied pressures. l) R of ZnO photodetector with respect to applied pressure at metal-semiconductor contact. a-d) Reproduced with permission.[228] Copyright 2018, American Chemical Society. e-f) Reproduced with permission.[37] Copyright 2021, Elsevier. g-l) Reproduced with permission[229]. Copyright 2021, Elsevier.
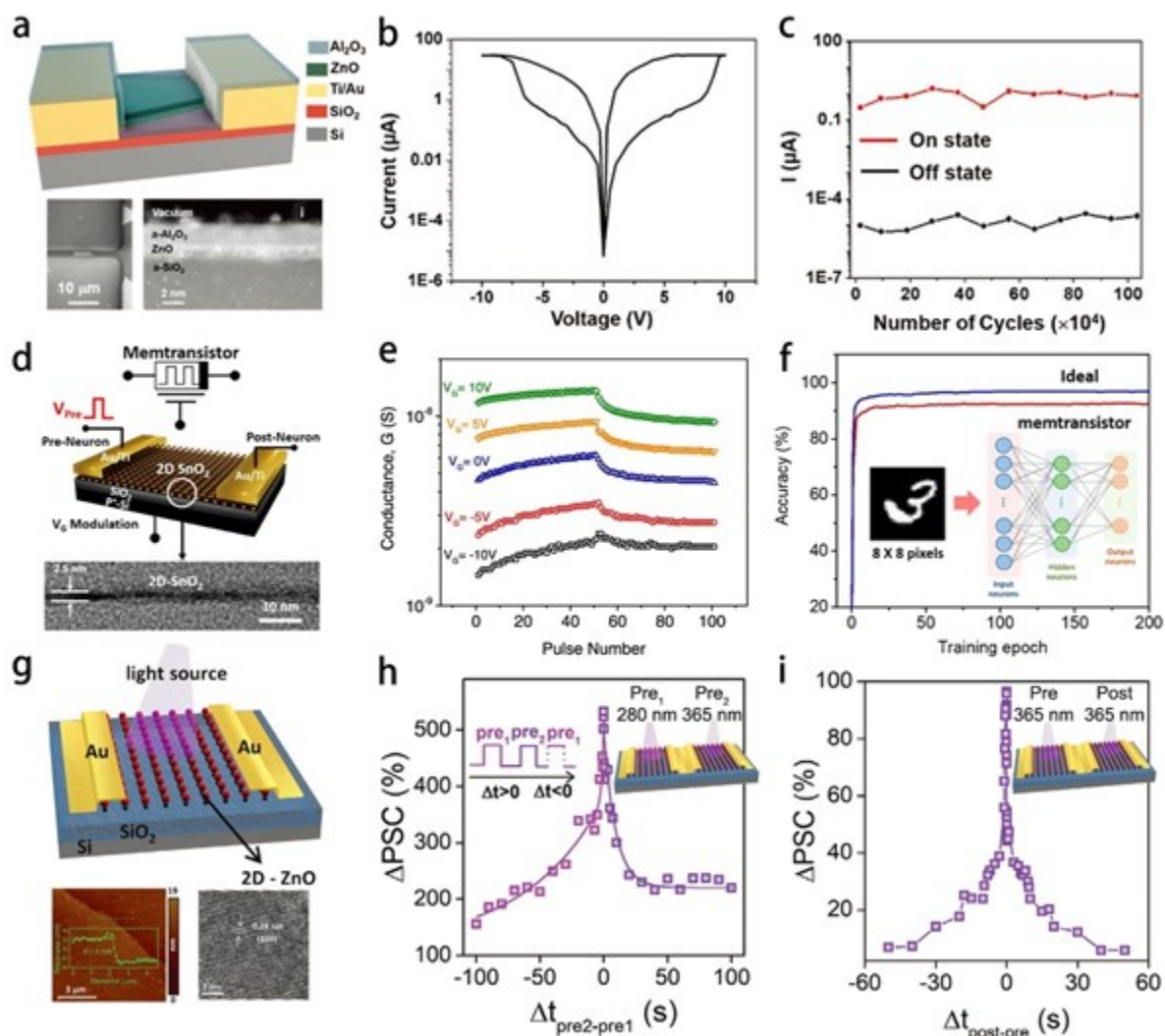
Figure 14. a) Schematic of a 2D ZnO/Al$_2$O$_3$ heterolayered nanosheet memristor with SEM and TEM image of device stucture. b) The typical resistive swiching *I-V* curve of 2D ZnO/Al$_2$O$_3$ memristor. c) Endurance of one device over 10^6 cycles at "On" and "Off" states. d) Schematic illustration of the gate-tunable 2D SnO$_2$ memristor. e) Analog switching behavior of the 2D-SnO$_2$ memristor by potentiation and depression training pulses under different gate voltages. f) Simulated pattern recognition accuracy of the 2D SnO$_2$ memristor. g) Schematic illustration of 2D ZnO synaptic devices. h) Change in PSC as a function of the time interval between optical stimulations when excited at presynapse 1 and presynapse 2. i) ΔPSC as a function of the time difference between pre and postsynaptic pulses. a-c) Reproduced with permission.[40] Copyright 2020, Wiley-VCH GmbH. d-f) Reproduced with permission.[41] Copyright 2021, American Chemical Society. g-i) Reproduced with permission.[42]

Table 1. Summary of structure, bandgap and thickness of the 2D metal oxides prepared by various methods.

Materials	Structure	Crystal system	Space group	Bandgap [eV]	Thickness [nm]	Methods	Ref.
In_2O_3	Non-layered	Cubic	*Ia-3*	2.61-3.75	1.53 [69]	Liquid metal printing	[46, 69, 136]
ITO	Non-layered	Cubic	*Ia-3*	3.5-4.3	1.5 [29]	Liquid metal printing, Sputtering	[29, 165, 265]
ZnO	Non-Layered	Hexagonal	*P63mc*	3.5	0.6 [37]	Liquid metal printing	[37, 42]
ZnO-SDS	Non-Layered	Hexagonal	*P63mc*	3.37	0.75 [40]	AILE	[35, 40, 100, 225, 228, 266]
SnO_2	Non-layered	Tetragonal	*P42/mnm*	3.6-4.0	2 [41]	Liquid metal printing	[41]
β-Ga_2O_3	Non-layered	Monoclinic	*C12/m1*	4.9	2.7 [166]	Liquid metal printing	[166]
α-Bi_2O_3	Non-layered	Monoclinic	*P21/c*	3.5	0.75 [145]	Liquid metal printing	[145]
γ-Bi_2O_3	Non-layered	Cubic	*I23*	3.4	4.8 [50]	CVD	[50]
MoO_2	Non-layered	-	-	-	6 [267]	CVD	[267]
VO_2	Non-layered	Tetragonal	*P42/mnm*	Metallic	30 [52]	CVD	[52]
		Monoclinic	*P21/c*	~0.55			
TiO_2	Non-layered	Tetragonal	*P42/mnm*	-	~2 [134]	Liquid metal printing	[134]
Fe_3O_4	Non-layered	Cubic	*Fd-3m*	-	1.95 [36]	CVD	[36]
HfO_2	Non-layered	Monoclinic	*P21/c*	6	0.5 [133]	Liquid metal printing, ALD	[133, 182]
Gd_2O_3	Non-layered	Cubic	*Ia-3*	~5.4	0.51 [133]	Liquid metal printing	[133]
Al_2O_3	Non-layered	Trigonal	*R-3c*	7	1.1 [133]	Liquid metal printing	[133]
Y_2O_3	Non-layered	Hexagonal	-	-	-	MBE	[18]
h-TiO_2	Layered	Hexagonal	-	2.35	0.45 [32]	Metal-gas interface	[32]
h-MnO	layered	Hexagonal	-	-	0.65 [32]	Metal-gas interface	[32]
h-Fe_2O_3	layered	Hexagonal	-	-	0.64 [32]	Metal-gas interface	[32]
h-CoO	layered	Hexagonal	-	-	0.84 [32]	Metal-gas interface	[32]
h-Ni_2O_3	layered	Hexagonal	-	-	0.71 [32]	Metal-gas interface	[32]
h-Cu_2O	layered	Hexagonal	-	-	0.42 [32]	Metal-gas interface	[32]
h-Al_2O_3	layered	Hexagonal	-	-	0.62 [32]	Metal-gas interface	[32]
h-GeO_2	layered	Hexagonal	-	-	0.51 [32]	Metal-gas interface	[32]
h-Gd_2O_3	layered	Hexagonal	-	-	0.71 [32]	Metal-gas interface	[32]
RuO_2	layered	Tetragonal	*P42/mnm*	-	~2 [117]	Ion exchange liquid	[117]

						exfoliation	
TiO_x	Layered	-	-	-	1.5 [268]	Ion exchange liquid exfoliation	[268]
SnO	Layered	Tetragonal	P4/nmm	4.21	0.6 [146]	Liquid metal printing, PLD	[46, 136, 146, 163]
α-MoO_3	Layered	Orthorhombic	Pnma	2.72-3.2	4 [269]	PVT, Mechanical exfoliation	[200, 269-271]
WO_3	Layered	Monoclinic	$P2_1/c$	3.53	0.72 [125]	ALD	[125]
V_2O_5	Layered	Orthorhombic	Pmmn	2.2-2.7	40 [58]	Mechanical exfoliation	[58]
α-Sb_2O_3	Layered	Cubic	Fd-3m	3.0-5.6	0.64 [43] 1.5 [147] 2 [184]	CVD, Thermal evaporation, Liquid metal printing	[34, 43, 147, 184]
h-BeO	Layered	Hexagonal	-	6	0.3 [55]	MBE	[55]
gZnO	Layered	Hexagonal	-	4.8	0.28 [54]	Solution-Based GO template	[54]
gZn(Co)O	Layered	Hexagonal	-	-	0.28 [38]	Solution-Based GO template	[38]
$Ca_2Nb_3O_{10}$	Layered	Orthorhombic	Cmm2	3.85	1.8 [45]	Ion exchange liquid exfoliation	[45]
$Sr_2Nb_3O_{10}$	Layered	Orthorhombic	Cmm2	3.9	1.8 [30]	Ion exchange liquid exfoliation	[30]
$Ca_2Nb_{2.5}Ta_{0.5}O_{10}$	Layered	Orthorhombic	Cmm2	3.65	3.5 [119]	Ion exchange liquid exfoliation	[119]
$SrTiO_3$	Non-layered	Cubic	Pm-3m	3.25/3.75	4.6 [272] 0.4 [44]	PLD	[44, 272]
$BiFeO_3$	Non-layered	Cubic	Pm-3m	2.74	0.4 [44]	MBE	[44]

Table 2. Comparison of synthesis methods.

Method[a]	Defect Density	Material Size	Surface Clearness	Thickness Control	Substrate	Cost	Production Efficiency	Applicable range
ME	Excellent	Inferior	Excellent	Average	Good	Excellent	Poor	Poor
LPE	Average	Poor	Inferior	Inferior	Excellent	Excellent	Excellent	Poor
Template-assist Solution Process	Inferior	Inferior	Inferior	Poor	Average	Good	Good	Good
Liquid metal printing	Average	Excellent	Average	Average	Good	Excellent	Good	Average
Metal-gas interface	Good	Good`	Good	Good	Average	Poor	Poor	Good
Native Oxide	Inferior	Inferior	Excellent	Good	Average	Good	Poor	Poor
PVD/PVT	Good	Good	Good	Excellent	Inferior	Average	Good	Excellent
MBE	Excellent	Excellent	Excellent	Excellent	Poor	Poor	Average	Good
ALD	Inferior	Excellent	Good	Excellent	Inferior	Average	Good	Excellent
CVD/CVT	Good	Good	Good	Excellent	Inferior	Average	Good	Excellent

a) Original name and abbreviation: Mechanical exfoliation (ME), Liquid Phase Exfoliation (LPE), Common Physical Vapor Deposition/Transport (PVD/PVT), Molecular Beam Epitaxy (MBE), Chemical Vapor Deposition/Transport (CVD/CVT).

Table 3. Summary of key figures-of-merit of FETs with 2D metal oxide as channel materials

Material	Method	Thickness [nm]	carrier type	Mobility [cm^2 V^{-1} s^{-1}]	On/off	Ref.
In$_2$O$_3$	Liquid metal printing	1.53	electron	μ_{FE}=4	10^5	[69]
In$_2$O$_3$	Liquid metal printing	-	electron	μ_{FE}=3.3	-	[165]
In$_2$O$_3$	Liquid metal printing	-	electron	μ_{sat}=12.8	10^8	[46]
SnO$_2$	Liquid metal printing	-	electron	μ_{sat}=2	10^4	[46]
ITO	Liquid metal printing	1.9	electron	μ_{sat}=27	10^9	[165]
IZO (0.5 wt %)	Liquid metal printing	1.59	electron	μ_{FE}=87	10^5	[69]
IZO (5 wt %)	Liquid metal printing	1.7	electron	μ_{FE}=18	10^5	[69]
α-MoO$_3$	CVD	6	electron	μ_{FE}=0.03	10^3	[273]
SnO	Liquid metal printing	0.6	hole	μ_{FE}=0.7	20	[146]
SnO	Liquid metal printing	1	hole	μ_{FE}=0.47	10^6	[46]
SnO	PLD	2.5-6	hole	μ_{FE}=0.05-1.9	-	[163]
β-Ga$_2$O$_3$	Liquid metal printing	3-6	hole	μ_{FE}=21.3	10^4	[166]
α-MoO$_3$	Mechanical exfoliation	11	hole	μ_{FE}>1100	<10^3	[274]
h-TiO$_2$	Metal-gas interface	0.5-5	hole	μ_{FE}=10-950	~10^4	[32]
ZnO-SOS	AILE	1~2	hole	μ_{FE}=0.1	-	[100]
ZnO-SDS	AILE	1.5	hole	μ_{FE}=0.31	4	[35]

Table 4. Summary of key figures-of-merit of 2D FETs with 2D metal oxides and metal oxide thin films as gate dielectric.

Dielectric layer (Buffer layer)	Channel material	Dielectric constants ε_{eff}	EOT [nm]	Leakage J [A cm^{-2}]	E_{bd} [MV cm^{-1}]	Channel Length	SS [mV dec^{-1}]	Ref.
4 nm HfO$_2$	CVD-MoS$_2$	8.2	1.9	1.25×10^{-2}	-	L[a)]	80	[275]
1.45nm HfO$_2$ (PTCDA)	Graphene	5.7	1	1.5×10^{-2}	16.5	L	-	[182]
3 nm HfO$_2$ (PTCDA)	CVD-MoS$_2$	9	1.3	2.5×10^{-5}	-	L	60	[182]
3 nm HfO$_2$ (PTCDA)	CVD-WSe$_2$	9	1.3	-	-	L	67	[182]
6 nm HfO$_2$ (PTCDA)	Graphene	11.7	2	1.0×10^{-6}	9.6	L	-	[182]
6 nm HfO$_2$ (PTCDA)	CVD-MoS$_2$	11.7	2	$\sim1.0\times10^{-6}$	-	L	-	[182]
16 nm SrTiO$_3$	CVD-MoS$_2$	63	1	-	5.75	L	71.5	[33]
6.1 nm Al$_2$O$_3$	MoS$_2$ (FG plasma)	6.7	3.55	8.0×10^{-6}	-	L	85	[276]
5 nm HfO$_2$ (Hf)	Graphene	13	1.5	1.0×10^{-8} ~ 1.0×10^{-5}	9	L	< 60 (Tunnelling transistor)	[277]
9 nm HfO$_2$ (Y$_2$O$_3$)	MoS$_2$	8	4.4	2.0×10^{-7} ~8.0×10^{-5}	7.2	L	65	[278]
5.3 nm Al$_2$O$_3$ (TiOPc)	WSe$_2$	6.9	3	4.6×10^{-6}	10	L	80	[175]
10 nm Sb$_2$O$_3$	MoS$_2$	11.5	3.3	1.0×10^{-7} ~1.0×10^{-3}	2.7	L	64	[34]
5 nm Bi$_2$SeO$_5$	Bi$_2$O$_2$Se	19~21	0.9	4.6×10^{-2}	18	L	73	[156]
20 nm Bi$_2$SeO$_5$	Bi$_2$O$_2$Se	21	3.6	1.0×10^{-7} ~1.0×10^{-4}	-	L	75	[156]
2.2 nm CaF$_2$	CVD-MoS$_2$	8.6	1	2.0×10^{-5} ~ 1.0×10^{-2}	27.8[183]	L	91	[78]
4 nm Al$_2$O$_3$	CVD-MoS$_2$	6.2	2.5	-	-	10 nm	120	[279]
4 nm HfO$_2$	CVD-MoS$_2$	8.2	1.9	-	-	29 nm	120	[275]
6 nm HfO$_2$ / PTCDA	CVD-MoS$_2$	11.7	2	$\sim1.0\times10^{-6}$	-	20 nm	73	[182]

| 16 nm $SrTiO_3$ | CVD-MoS_2 | 63 | 1 | - | 5.75 | 25 nm | 86.5 | [33] |

a) L represent the channel length >100 nm.

Table 5. Summary of key figures-of-merit of photodetector with 2D metal oxide as active layer.

Materials	Detection light	Bias [V]	Responsivity [A W^{-1}]	EQE [%]	On/off current ratio	Rise/Fall time [ms]	D* [Jones]	ref
$Ca_2Nb_3O_{10}$	280 nm	3	14.94	-	3.4×10^4	0.08/5.6	8.7×10^{13}	[45]
$Sr_2Nb_3O_{10}$	270 nm	1	1.21×10^3	5.6×10^5	10^5	0.4/40	1.4×10^{14}	[30]
$Ca_2Nb_{2.5}Ta_{0.5}O_{10}$	295 nm	1	4.7×10^2	1.97×10^5	5.6×10^4	0.9/152	7.65×10^{13}	[119]
α-MoO_3	254 nm	2	6.79×10	3.3×10^4	10	-	-	[210]
α-MoO_{3-x}	365 nm	0.1	5.44×10	-	-	0.2/0.2	-	[271]
ZnO-SDS	254 nm	5	2.0×10^4	-	-	$3.97\times10^3/5.32\times10^3$	6.83×10^{14}	[35]
ZnO	365 nm	0.05	1.26×10	4.3×10^3	-	$1.16\times10^4/9.37\times10^4$	5.81×10^{15}	[42]
γ-Bi_2O_3	365 nm	5	6.45×10	9.18×10^2	10^3	0.29/0.87	1.3×10^{13}	[50]
a-Ga_2O_3	254 nm	5	7.33×10^2	4.1×10^5	3.9×10^7	-	3.9×10^{16}	[215]
α-Bi_2O_3	365 nm	3	4.0×10^2	-	-	0.07/4.3	~1.1×10^{13}	[145]
Ga_2O_3	254 nm	10	3.3	1.6×10^3	-	-	4.0×10^{12}	[155]
Fe_3O_4	10.6 μm	3	5.61×10^2	6.6×10^3	-	$9\times10^2/7\times10^2$	7.42×10^8	[36]
MgO	150 nm	4	1.86	1.54×10^3	~10^2	$1\times10^3/1\times10^3$	1.8×10^{10}	[280]

Accepted Article

WILEY-VCH

Emerging two-dimensional (2D) metal oxides exhibit intriguing electronic and optical properties, which have great potential in emerging functional devices. Diverse structures and various synthesis methods open a new field of vision for device fabrication based 2D metal oxides. Their unique properties could bring new vigor and vitality into 2D material family.

Kui Zhou, Gang Shang, Hsiao-Hsuan Hsu, Su-Ting Han, Vellaisamy A. L. Roy and Ye Zhou*

Emerging Two-Dimensional Metal Oxides: From Synthesis to Device Integration

WILEY-VCH
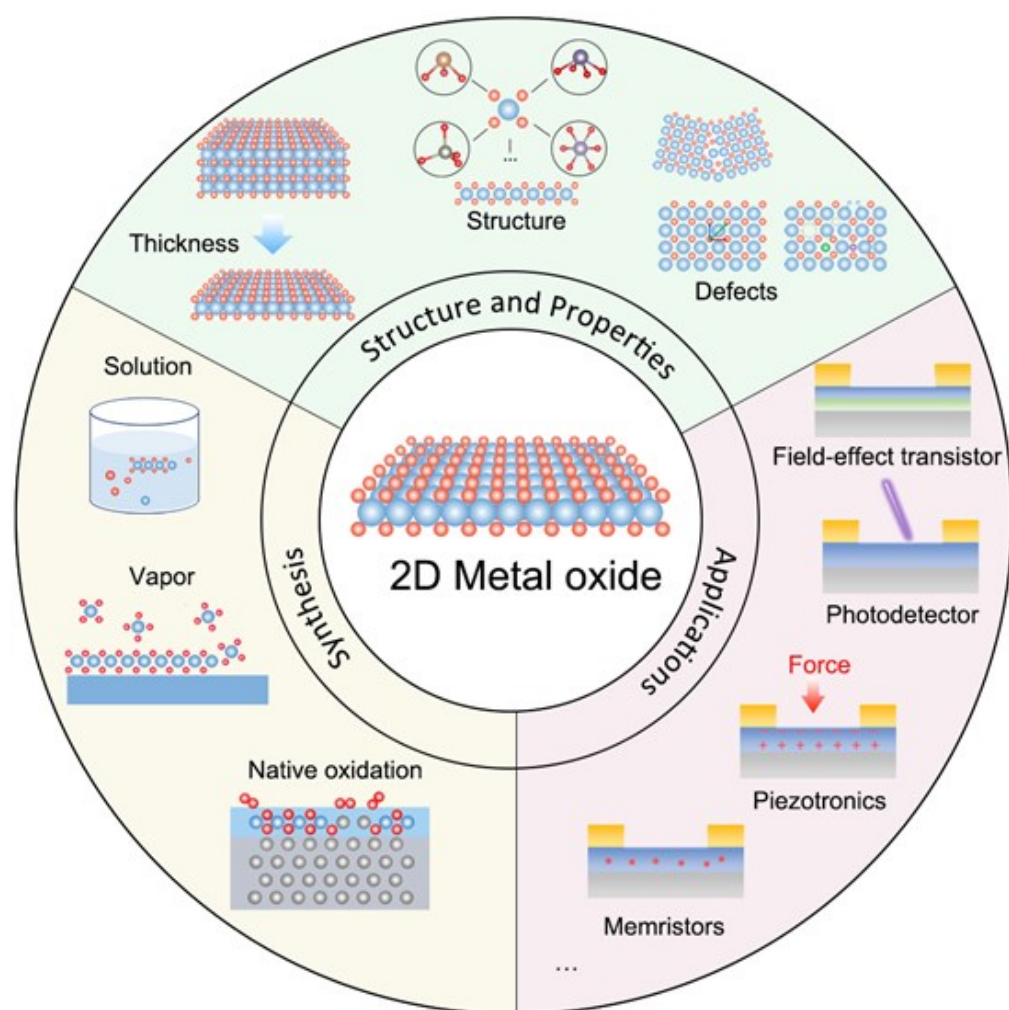
Reference

[1] P. V. Pham, S. C. Bodepudi, K. Shehzad, Y. Liu, Y. Xu, B. Yu, X. Duan, *Chem. Rev.* **2022**, *122*, 6514.

[2] F. Wang, K. Pei, Y. Li, H. Li, T. Zhai, *Adv. Mater.* **2021**, *33*, 2005303.

[3] K. Zhu, C. Wen, A. A. Aljarb, F. Xue, X. Xu, V. Tung, X. Zhang, H. N. Alshareef, M. Lanza, *Nat. Electron.* **2021**, *4*, 775.

[4] J. D. Yao, G. W. Yang, *Nano Today* **2021**, *36*, 101026.

[5] A. G. Ricciardulli, S. Yang, J. H. Smet, M. Saliba, *Nat. Mater.* **2021**, *20*, 1325.

[6] Y. Liu, X. Duan, H.-J. Shin, S. Park, Y. Huang, X. Duan, *Nature* **2021**, *591*, 43.

[7] N. R. Glavin, R. Rao, V. Varshney, E. Bianco, A. Apte, A. Roy, E. Ringe, P. M. Ajayan, *Adv. Mater.* **2020**, *32*, 1904302.

[8] X. Liu, M. C. Hersam, *Nat. Rev. Mater.* **2019**, *4*, 669.

[9] R. You, Y.-Q. Liu, Y.-L. Hao, D.-D. Han, Y.-L. Zhang, Z. You, *Adv. Mater.* **2020**, *32*, 1901981.

[10] R. Wang, X.-G. Ren, Z. Yan, L.-J. Jiang, W. E. I. Sha, G.-C. Shan, *Front. Phys.* **2018**, *14*, 13603.

[11] X.-T. Liu, J.-R. Chen, Y. Wang, S.-T. Han, Y. Zhou, *Adv. Funct. Mater.* **2021**, *31*, 2004733.

[12] S. Roy, X. Zhang, A. B. Puthirath, A. Meiyazhagan, S. Bhattacharyya, M. M. Rahman, G. Babu, S. Susarla, S. K. Saju, M. K. Tran, L. M. Sassi, M. A. S. R. Saadi, J. Lai, O. Sahin, S. M. Sajadi, B. Dharmarajan, D. Salpekar, N. Chakingal, A. Baburaj, X. Shuai, A. Adumbumkulath, K. A. Miller, J. M. Gayle, A. Ajnsztajn, T. Prasankumar, V. V. J. Harikrishnan, V. Ojha, H. Kannan, A. Z. Khater, Z. Zhu, S. A. Iyengar, P. A. d. S. Autreto, E. F. Oliveira, G. Gao, A. G. Birdwell, M. R. Neupane, T. G. Ivanov, J. Taha-Tijerina, R. M. Yadav, S. Arepalli, R. Vajtai, P. M. Ajayan, *Adv. Mater.* **2021**, *33*, 2101589.

[13] T. Tan, X. Jiang, C. Wang, B. Yao, H. Zhang, *Adv. Sci.* **2020**, *7*, 2000058.

[14] T. Chowdhury, E. C. Sadler, T. J. Kempa, *Chem. Rev.* **2020**, *120*, 12563.

[15] G. Ding, B. Yang, R.-S. Chen, K. Zhou, S.-T. Han, Y. Zhou, *Appl. Phys. Rev.* **2021**, *8*, 011316.

[16] H. Xu, A. Ren, J. Wu, Z. Wang, *Adv. Funct. Mater.* **2020**, *30*, 2000907.

[17] A. Allain, J. Kang, K. Banerjee, A. Kis, *Nat. Mater.* **2015**, *14*, 1195.

[18] R. Addou, A. Dahal, M. Batzill, *Nat. Nanotechnol.* **2013**, *8*, 41.

[19] X. Xu, T. Guo, H. Kim, M. K. Hota, R. S. Alsaadi, M. Lanza, X. Zhang, H. N. Alshareef, *Adv. Mater.* **2022**, *34*, 2108258.

[20] X. Wang, Y. Sun, K. Liu, *2D Mater.* **2019**, *6*, 042001.

[21] M. Si, Z. Lin, Z. Chen, P. D. Ye, presented at *2021 Symposium on VLSI Technology*, 13-19 June 2021, **2021**.

[22] A. Charnas, M. Si, Z. Lin, P. D. Ye, *Appl. Phys. Lett.* **2021**, *118*, 052107.

[23] M. Si, Z. Lin, Z. Chen, X. Sun, H. Wang, P. D. Ye, *Nat. Electron.* **2022**, *5*, 164.

[24] M. Si, Y. Hu, Z. Lin, X. Sun, A. Charnas, D. Zheng, X. Lyu, H. Wang, K. Cho, P. D. Ye, *Nano Lett.* **2021**, *21*, 500.

[25] S. B. Ogale, *Adv. Mater.* **2010**, *22*, 3125.

[26] M. Gibertini, M. Koperski, A. F. Morpurgo, K. S. Novoselov, *Nat. Nanotechnol.* **2019**, *14*, 408.

[27] C. Yang, Y. Liu, Y. Wang, L. Feng, Q. He, J. Sun, Y. Tang, C. Wu, J. Xiong, W. Zhang, X. Lin, H. Yao, H. Liu, G. Fernandes, J. Xu, J. M. Valles, J. Wang, Y. Li, *Science* **2019**, *366*, 1505.

[28] A. Gozar, G. Logvenov, L. F. Kourkoutis, A. T. Bollinger, L. A. Giannuzzi, D. A. Muller, I. Bozovic, *Nature* **2008**, *455*, 782.

WILEY-VCH

[29]   R. S. Datta, N. Syed, A. Zavabeti, A. Jannat, M. Mohiuddin, M. Rokunuzzaman, B. Yue Zhang, M. A. Rahman, P. Atkin, K. A. Messalea, M. B. Ghasemian, E. D. Gaspera, S. Bhattacharyya, M. S. Fuhrer, S. P. Russo, C. F. McConville, D. Esrafilzadeh, K. Kalantar-Zadeh, T. Daeneke, *Nat. Electron.* **2020**, *3*, 51.

[30]   S. Li, Y. Zhang, W. Yang, H. Liu, X. Fang, *Adv. Mater.* **2020**, *32*, 1905443.

[31]   S. S. Hong, J. H. Yu, D. Lu, A. F. Marshall, Y. Hikita, Y. Cui, H. Y. Hwang, *Sci. Adv.* **2017**, *3*, eaao5173.

[32]   B. Y. Zhang, K. Xu, Q. Yao, A. Jannat, G. Ren, M. R. Field, X. Wen, C. Zhou, A. Zavabeti, J. Z. Ou, *Nat. Mater.* **2021**, *20*, 1073.

[33]   J.-K. Huang, Y. Wan, J. Shi, J. Zhang, Z. Wang, W. Wang, N. Yang, Y. Liu, C.-H. Lin, X. Guan, L. Hu, Z.-L. Yang, B.-C. Huang, Y.-P. Chiu, J. Yang, V. Tung, D. Wang, K. Kalantar-Zadeh, T. Wu, X. Zu, L. Qiao, L.-J. Li, S. Li, *Nature* **2022**, *605*, 262.

[34]   K. Liu, B. Jin, W. Han, X. Chen, P. Gong, L. Huang, Y. Zhao, L. Li, S. Yang, X. Hu, J. Duan, L. Liu, F. Wang, F. Zhuge, T. Zhai, *Nat. Electron.* **2021**, *4*, 906.

[35]   H. Yu, Q. Liao, Z. Kang, Z. Wang, B. Liu, X. Zhang, J. Du, Y. Ou, M. Hong, J. Xiao, Z. Zhang, Y. Zhang, *Small* **2020**, *16*, 2005520.

[36]   C. Yin, C. Gong, J. Chu, X. Wang, C. Yan, S. Qian, Y. Wang, G. Rao, H. Wang, Y. Liu, X. Wang, J. Wang, W. Hu, C. Li, J. Xiong, *Adv. Mater.* **2020**, *32*, 2002237.

[37]   N. Mahmood, H. Khan, K. Tran, P. Kuppe, A. Zavabeti, P. Atkin, M. B. Ghasemian, J. Yang, C. Xu, S. A. Tawfik, M. J. S. Spencer, J. Z. Ou, K. Khoshmanesh, C. F. McConville, Y. Li, K. Kalantar-Zadeh, *Mater. Today* **2021**, *44*, 69.

[38]   R. Chen, F. Luo, Y. Liu, Y. Song, Y. Dong, S. Wu, J. Cao, F. Yang, A. N'Diaye, P. Shafer, Y. Liu, S. Lou, J. Huang, X. Chen, Z. Fang, Q. Wang, D. Jin, R. Cheng, H. Yuan, R. J. Birgeneau, J. Yao, *Nat. Commun.* **2021**, *12*, 3952.

[39]   Y. Yu, L. Ma, P. Cai, R. Zhong, C. Ye, J. Shen, G. D. Gu, X. H. Chen, Y. Zhang, *Nature* **2019**, *575*, 156.

[40]   X. Yin, Y. Wang, T.-h. Chang, P. Zhang, J. Li, P. Xue, Y. Long, J. L. Shohet, P. M. Voyles, Z. Ma, X. Wang, *Adv. Mater.* **2020**, *32*, 2000801.

[41]   C.-H. Huang, H. Chang, T.-Y. Yang, Y.-C. Wang, Y.-L. Chueh, K. Nomura, *ACS Appl. Mater. Interfaces* **2021**, *13*, 52822.

[42]   V. Krishnamurthi, T. Ahmed, M. Mohiuddin, A. Zavabeti, N. Pillai, C. F. McConville, N. Mahmood, S. Walia, *Adv. Opt. Mater.* **2021**, *9*, 2100449.

[43]   W. Han, P. Huang, L. Li, F. Wang, P. Luo, K. Liu, X. Zhou, H. Li, X. Zhang, Y. Cui, T. Zhai, *Nat. Commun.* **2019**, *10*, 4728.

[44]   D. Ji, S. Cai, T. R. Paudel, H. Sun, C. Zhang, L. Han, Y. Wei, Y. Zang, M. Gu, Y. Zhang, W. Gao, H. Huyan, W. Guo, D. Wu, Z. Gu, E. Y. Tsymbal, P. Wang, Y. Nie, X. Pan, *Nature* **2019**, *570*, 87.

[45]   Y. Zhang, S. Li, Z. Li, H. Liu, X. Liu, J. Chen, X. Fang, *Nano Lett.* **2021**, *21*, 382.

[46]   C.-H. Huang, Y. Tang, T.-Y. Yang, Y.-L. Chueh, K. Nomura, *ACS Appl. Mater. Interfaces* **2021**, *13*, 52783.

[47]   Z. Hai, Z. Wei, C. Xue, H. Xu, F. Verpoort, *J. Mater. Chem. C* **2019**, *7*, 12968.

[48]   A. C. Gandhi, C.-Y. Lai, K.-T. Wu, P. V. R. K. Ramacharyulu, V. B. Koli, C.-L. Cheng, S.-C. Ke, S. Y. Wu, *Nanoscale* **2020**, *12*, 24119.

[49]   H. Razavi-Khosroshahi, K. Edalati, J. Wu, Y. Nakashima, M. Arita, Y. Ikoma, M. Sadakiyo, Y. Inagaki, A. Staykov, M. Yamauchi, Z. Horita, M. Fuji, *J. Mater. Chem. A* **2017**, *5*, 20298.

[50]   J. Wu, F. Wang, H. Li, S. Yang, P. Li, Y. Zhao, Y. Li, T. Zhai, *Small* **2022**, *18*, 2104244.

[51]   J. P. Allen, J. J. Carey, A. Walsh, D. O. Scanlon, G. W. Watson, *J. Phys. Chem. C* **2013**, *117*, 14759.

[52]   M. Ran, C. Zhao, X. Xu, X. Kong, Y. Lee, W. Cui, Z.-Y. Hu, A. Roxas, Z. Luo, H. Li, F. Ding, L. Gan, T. Zhai, *Fundam. Res.* **2022**, *2*, 456.

[53]   C. Tusche, H. L. Meyerheim, J. Kirschner, *Phys. Rev. Lett.* **2007**, *99*, 026102.

[54]   K. B. Tom, S. Lin, L. F. Wan, J. Wang, N. Ahlm, A. T. N'Diaye, K. Bustillo, J. Huang, Y. Liu, S. Lou, R. Chen, S. Yan, H. Wu, D. Jin, H. Yuan, D. Prendergast, J. Yao, *ACS Nano* **2018**, *12*, 7554.

[55]   H. Zhang, M. Holbrook, F. Cheng, H. Nam, M. Liu, C.-R. Pan, D. West, S. Zhang, M.-Y. Chou, C.-K. Shih, *ACS Nano* **2021**, *15*, 2497.

[56]   K. V. Larionov, D. G. Kvashnin, P. B. Sorokin, *J. Phys. Chem. C* **2018**, *122*, 17389.

[57]   Y. Guo, L. Ma, K. Mao, M. Ju, Y. Bai, J. Zhao, X. C. Zeng, *Nanoscale Horiz.* **2019**, *4*, 592.

[58]   S. Sucharitakul, G. Ye, W. R. L. Lambrecht, C. Bhandari, A. Gross, R. He, H. Poelman, X. P. A. Gao, *ACS Appl. Mater. Interfaces* **2017**, *9*, 23949.

[59]   Y. Gong, Y. Zhao, Z. Zhou, D. Li, H. Mao, Q. Bao, Y. Zhang, G. P. Wang, *Adv. Opt. Mater.* **2022**, *10*, 2200038.

[60]   Y. Wu, Q. Ou, Y. Yin, Y. Li, W. Ma, W. Yu, G. Liu, X. Cui, X. Bao, J. Duan, G. Álvarez-Pérez, Z. Dai, B. Shabbir, N. Medhekar, X. Li, C.-M. Li, P. Alonso-González, Q. Bao, *Nat. Commun.* **2020**, *11*, 2646.

[61]   G. Hu, Q. Ou, G. Si, Y. Wu, J. Wu, Z. Dai, A. Krasnok, Y. Mazor, Q. Zhang, Q. Bao, C.-W. Qiu, A. Alù, *Nature* **2020**, *582*, 209.

[62]   M. Chen, X. Lin, T. H. Dinh, Z. Zheng, J. Shen, Q. Ma, H. Chen, P. Jarillo-Herrero, S. Dai, *Nat. Mater.* **2020**, *19*, 1307.

[63]   W. Li, J. Shi, K. H. L. Zhang, J. L. MacManus-Driscoll, *Mater. Horiz.* **2020**, *7*, 2832.

[64]   E. Pastor, M. Sachs, S. Selim, J. R. Durrant, A. A. Bakulin, A. Walsh, *Nat. Rev. Mater.* **2022**, *7*, 503.

[65]   V.-A. Ha, D. Waroquiers, G.-M. Rignanese, G. Hautier, *Appl. Phys. Lett.* **2016**, *108*, 201902.

[66]   Z. Wang, P. K. Nayak, J. A. Caraveo-Frescas, H. N. Alshareef, *Adv. Mater.* **2016**, *28*, 3831.

[67]   H. Raebiger, S. Lany, A. Zunger, *Phys. Rev. B* **2007**, *76*, 045209.

[68]   H. Bian, Y. Y. Goh, Y. Liu, H. Ling, L. Xie, X. Liu, *Adv. Mater.* **2021**, *33*, 2006469.

[69]   A. Jannat, N. Syed, K. Xu, M. A. Rahman, M. M. M. Talukder, K. A. Messalea, M. Mohiuddin, R. S. Datta, M. W. Khan, T. Alkathiri, B. J. Murdoch, S. Z. Reza, J. Li, T. Daeneke, A. Zavabeti, J. Z. Ou, *ACS Nano* **2021**, *15*, 4045.

[70]   S. R. Thomas, P. Pattanasattayavong, T. D. Anthopoulos, *Chem. Soc. Rev.* **2013**, *42*, 6910.

[71]   V. H. Nguyen, U. Gottlieb, A. Valla, D. Muñoz, D. Bellet, D. Muñoz-Rojas, *Mater. Horiz.* **2018**, *5*, 715.

[72]   Y. Magari, T. Kataoka, W. Yeh, M. Furuta, *Nat. Commun.* **2022**, *13*, 1078.

[73]   P. Y. Huang, C. S. Ruiz-Vargas, A. M. van der Zande, W. S. Whitney, M. P. Levendorf, J. W. Kevek, S. Garg, J. S. Alden, C. J. Hustedt, Y. Zhu, J. Park, P. L. McEuen, D. A. Muller, *Nature* **2011**, *469*, 389.

[74]   Y. Ye, A. B. Hamlin, J. E. Huddy, M. S. Rahman, W. J. Scheideler, *Adv. Funct. Mater.* **2022**, *n/a*, 2204235.

[75]   M. Chen, B. Peng, H. Li, *J. Mater. Chem. C* **2022**, *10*, 4985.

[76]   Y. Y. Illarionov, T. Knobloch, M. Jech, M. Lanza, D. Akinwande, M. I. Vexler, T. Mueller, M. C. Lemme, G. Fiori, F. Schwierz, T. Grasser, *Nat. Commun.* **2020**, *11*, 3385.

[77]   C. Lee, S. Rathi, M. A. Khan, D. Lim, Y. Kim, S. J. Yun, D.-H. Youn, K. Watanabe, T. Taniguchi, G.-H. Kim, *Nanotechnology* **2018**, *29*, 335202.

[78]   Y. Y. Illarionov, A. G. Banshchikov, D. K. Polyushkin, S. Wachter, T. Knobloch, M. Thesberg, L. Mennel, M. Paur, M. Stöger-Pollach, A. Steiger-Thirsfeld, *Nat. Electron.* **2019**, *2*, 230.

[79]   S.-L. Li, H. Miyazaki, H. Song, H. Kuramochi, S. Nakaharai, K. Tsukagoshi, *ACS Nano* **2012**, *6*, 7381.

[80]   Y. Y. Wang, Z. H. Ni, Z. X. Shen, H. M. Wang, Y. H. Wu, *Appl. Phys. Lett.* **2008**, *92*, 043121.

[81]   A. Molina-Sánchez, D. Sangalli, K. Hummer, A. Marini, L. Wirtz, *Phys. Rev. B* **2013**, *88*, 045412.

[82]   Y. Huang, E. Sutter, J. T. Sadowski, M. Cotlet, O. L. A. Monti, D. A. Racke, M. R. Neupane, D. Wickramaratne, R. K. Lake, B. A. Parkinson, P. Sutter, *ACS Nano* **2014**, *8*, 10743.

[83]   S. Das, J. Appenzeller, *physica status solidi (RRL) – Rapid Research Letters* **2013**, *7*, 268.

[84]   R. Hinchet, U. Khan, C. Falconi, S.-W. Kim, *Mater. Today* **2018**, *21*, 611.

[85]   W. Wu, L. Wang, Y. Li, F. Zhang, L. Lin, S. Niu, D. Chenet, X. Zhang, Y. Hao, T. F. Heinz, J. Hone, Z. L. Wang, *Nature* **2014**, *514*, 470.

[86]   T. Zhang, P. Cheng, W.-J. Li, Y.-J. Sun, G. Wang, X.-G. Zhu, K. He, L. Wang, X. Ma, X. Chen, Y. Wang, Y. Liu, H.-Q. Lin, J.-F. Jia, Q.-K. Xue, *Nat. Phys.* **2010**, *6*, 104.

[87]   S. Qin, J. Kim, Q. Niu, C.-K. Shih, *Science* **2009**, *324*, 1314.

[88]   Y. Guo, Y.-F. Zhang, X.-Y. Bao, T.-Z. Han, Z. Tang, L.-X. Zhang, W.-G. Zhu, E. G. Wang, Q. Niu, Z. Q. Qiu, J.-F. Jia, Z.-X. Zhao, Q.-K. Xue, *Science* **2004**, *306*, 1915.

[89]   A. Puthirath Balan, S. Radhakrishnan, R. Kumar, R. Neupane, S. K. Sinha, L. Deng, C. A. de los Reyes, A. Apte, B. M. Rao, M. Paulose, R. Vajtai, C. W. Chu, G. Costin, A. A. Martí, O. K. Varghese, A. K. Singh, C. S. Tiwary, M. R. Anantharaman, P. M. Ajayan, *Chem. Mater.* **2018**, *30*, 5923.

[90]   S. T. Xu, Y. Q. Ma, G. H. Zheng, Z. X. Dai, *Nanoscale* **2015**, *7*, 6520.

[91]   J. Wang, A. Scholl, H. Zheng, S. B. Ogale, D. Viehland, D. G. Schlom, N. A. Spaldin, K. M. Rabe, M. Wuttig, L. Mohaddes, J. Neaton, U. Waghmare, T. Zhao, R. Ramesh, *Science* **2005**, *307*, 1203.

[92]   C. Androulidakis, K. Zhang, M. Robertson, S. Tawfick, *2D Mater.* **2018**, *5*, 032005.

[93]   K. S. Novoselov, A. K. Geim, S. V. Morozov, D. Jiang, Y. Zhang, S. V. Dubonos, I. V. Grigorieva, A. A. Firsov, *Science* **2004**, *306*, 666.

[94]   Y. Huang, Y.-H. Pan, R. Yang, L.-H. Bao, L. Meng, H.-L. Luo, Y.-Q. Cai, G.-D. Liu, W.-J. Zhao, Z. Zhou, L.-M. Wu, Z.-L. Zhu, M. Huang, L.-W. Liu, L. Liu, P. Cheng, K.-H. Wu, S.-B. Tian, C.-Z. Gu, Y.-G. Shi, Y.-F. Guo, Z. G. Cheng, J.-P. Hu, L. Zhao, G.-H. Yang, E. Sutter, P. Sutter, Y.-L. Wang, W. Ji, X.-J. Zhou, H.-J. Gao, *Nat. Commun.* **2020**, *11*, 2453.

[95]   B. A. Holler, K. Crowley, M.-H. Berger, X. P. A. Gao, *Adv. Electron. Mater.* **2020**, *6*, 2000635.

[96]   K. Kalantar-zadeh, A. Vijayaraghavan, M.-H. Ham, H. Zheng, M. Breedon, M. S. Strano, *Chem. Mater.* **2010**, *22*, 5660.

[97]   Y. Zhang, Q. Su, J. Zhu, S. Koirala, S. J. Koester, X. Wang, *Appl. Phys. Lett.* **2020**, *116*, 202101.

[98]   T.-H. Yang, Y. Shi, A. Janssen, Y. Xia, *Angew. Chem. Int. Ed.* **2020**, *59*, 15378.

[99]   R. Dong, T. Zhang, X. Feng, *Chem. Rev.* **2018**, *118*, 6189.

[100] F. Wang, J.-H. Seo, G. Luo, M. B. Starr, Z. Li, D. Geng, X. Yin, S. Wang, D. G. Fraser, D. Morgan, Z. Ma, X. Wang, *Nat. Commun.* **2016**, *7*, 10444.

[101] X. Yin, Q. Chen, P. Tian, P. Zhang, Z. Zhang, P. M. Voyles, X. Wang, *Chem. Mater.* **2018**, *30*, 3308.

[102] J. Yang, Z. Zeng, J. Kang, S. Betzler, C. Czarnik, X. Zhang, C. Ophus, C. Yu, K. Bustillo, M. Pan, J. Qiu, L.-W. Wang, H. Zheng, *Nat. Mater.* **2019**, *18*, 970.

[103] C. Schliehe, H. Juarez Beatriz, M. Pelletier, S. Jander, D. Greshnykh, M. Nagel, A. Meyer, S. Foerster, A. Kornowski, C. Klinke, H. Weller, *Science* **2010**, *329*, 550.

[104] S. C. Junggeburth, L. Diehl, S. Werner, V. Duppel, W. Sigle, B. V. Lotsch, *Journal of the American Chemical Society* **2013**, *135*, 6157.

[105] J. N. Israelachvili, D. J. Mitchell, B. W. Ninham, *J. Chem. Soc., Faraday Trans. 2* **1976**, *72*, 1525.

[106] Z. Sun, T. Liao, Y. Dou, S. M. Hwang, M.-S. Park, L. Jiang, J. H. Kim, S. X. Dou, *Nat. Commun.* **2014**, *5*, 3813.

[107] D. Chen, H. Feng, J. Li, *Chem. Rev.* **2012**, *112*, 6027.

[108] V. K. LaMer, R. H. Dinegar, *Journal of the American Chemical Society* **1950**, *72*, 4847.

[109] H. Zhao, Y. Zhu, F. Li, R. Hao, S. Wang, L. Guo, *Angew. Chem. Int. Ed.* **2017**, *56*, 8766.

[110] X. Xiao, H. Song, S. Lin, Y. Zhou, X. Zhan, Z. Hu, Q. Zhang, J. Sun, B. Yang, T. Li, L. Jiao, J. Zhou, J. Tang, Y. Gogotsi, *Nat. Commun.* **2016**, *7*, 11296.

[111] L. Huang, Z. Hu, H. Jin, J. Wu, K. Liu, Z. Xu, J. Wan, H. Zhou, J. Duan, B. Hu, J. Zhou, *Adv. Funct. Mater.* **2020**, *30*, 1908486.

[112] H. Wang, Z. Yao, G. S. Jung, Q. Song, M. Hempel, T. Palacios, G. Chen, M. J. Buehler, A. Aspuru-Guzik, J. Kong, *Matter* **2021**, *4*, 3339.

[113] T. Li, H. Jin, Z. Liang, L. Huang, Y. Lu, H. Yu, Z. Hu, J. Wu, B. Y. Xia, G. Feng, J. Zhou, *Nanoscale* **2018**, *10*, 6844.

[114] V. Nicolosi, M. Chhowalla, G. Kanatzidis Mercouri, S. Strano Michael, N. Coleman Jonathan, *Science* **2013**, *340*, 1226419.

[115] M. M. Y. A. Alsaif, A. F. Chrimes, T. Daeneke, S. Balendhran, D. O. Bellisario, Y. Son, M. R. Field, W. Zhang, H. Nili, E. P. Nguyen, K. Latham, J. van Embden, M. S. Strano, J. Z. Ou, K. Kalantar-zadeh, *Adv. Funct. Mater.* **2016**, *26*, 91.

[116] L. Liang, K. Li, C. Xiao, S. Fan, J. Liu, W. Zhang, W. Xu, W. Tong, J. Liao, Y. Zhou, B. Ye, Y. Xie, *Journal of the American Chemical Society* **2015**, *137*, 3102.

[117] S. Y. Kim, S.-i. Kim, M. K. Kim, J. Kim, S. Mizusaki, D.-S. Ko, C. Jung, D.-J. Yun, J. W. Roh, H.-S. Kim, H. Sohn, J.-H. Lim, J.-M. Oh, H. M. Jeong, W. H. Shin, *Inorg. Chem. Front.* **2021**, *8*, 4482.

[118] S.-H. Kweon, M. Im, W.-H. Lee, S. Nahm, J.-W. Choi, S.-J. Hwang, *J. Mater. Chem. C* **2016**, *4*, 178.

[119] X. Liu, S. Li, Z. Li, Y. Zhang, W. Yang, Z. Li, H. Liu, D. V. Shtansky, X. Fang, *Adv. Funct. Mater.* **2021**, *31*.

[120] B. Li, L. Ding, P. Gui, N. Liu, Y. Yue, Z. Chen, Z. Song, J. Wen, H. Lei, Z. Zhu, X. Wang, M. Su, L. Liao, Y. Gao, D. Zhang, G. Fang, *Adv. Mater. Interfaces* **2019**, *6*, 1901156.

[121] D. Lu, D. J. Baek, S. S. Hong, L. F. Kourkoutis, Y. Hikita, Harold Y. Hwang, *Nat. Mater.* **2016**, *15*, 1255.

[122] A. K. Geim, I. V. Grigorieva, *Nature* **2013**, *499*, 419.

[123] M. Golalikhani, Q. Lei, R. U. Chandrasena, L. Kasaei, H. Park, J. Bai, P. Orgiani, J. Ciston, G. E. Sterbinsky, D. A. Arena, P. Shafer, E. Arenholz, B. A. Davidson, A. J. Millis, A. X. Gray, X. X. Xi, *Nat. Commun.* **2018**, *9*, 2206.

[124] L. Liao, J. Bai, Y. Qu, Y.-c. Lin, Y. Li, Y. Huang, X. Duan, *Proceedings of the National Academy of Sciences* **2010**, *107*, 6711.

[125] Z. Hai, M. K. Akbari, C. Xue, H. Xu, L. Hyde, S. Zhuiykov, *Appl. Surf. Sci.* **2017**, *405*, 169.

[126] J. Yuan, A. Balk, H. Guo, Q. Fang, S. Patel, X. Zhao, T. Terlier, D. Natelson, S. Crooker, J. Lou, *Nano Lett.* **2019**, *19*, 3777.

[127] X. Hu, P. Huang, B. Jin, X. Zhang, H. Li, X. Zhou, T. Zhai, *Journal of the American Chemical Society* **2018**, *140*, 12909.

[128] N. Cabrera, N. F. Mott, *Rep. Prog. Phys.* **1949**, *12*, 163.

[129] K. Thürmer, E. Williams, J. Reutt-Robey, *Science* **2002**, *297*, 2033.

[130] T. Daeneke, K. Khoshmanesh, N. Mahmood, I. A. de Castro, D. Esrafilzadeh, S. J. Barrow, M. D. Dickey, K. Kalantar-zadeh, *Chem. Soc. Rev.* **2018**, *47*, 4073.

[131] M. Karbalaei Akbari, F. Verpoort, S. Zhuiykov, *J. Mater. Chem. A* **2021**, *9*, 34.

[132] S. Zhao, J. Zhang, L. Fu, *Adv Mater* **2021**, *33*, e2005544.

[133] A. Zavabeti, Z. Ou Jian, J. Carey Benjamin, N. Syed, R. Orrell-Trigg, L. H. Mayes Edwin, C. Xu, O. Kavehei, P. O'Mullane Anthony, B. Kaner Richard, K. Kalantar-zadeh, T. Daeneke, *Science* **2017**, *358*, 332.

[134] T. Alkathiri, N. Dhar, A. Jannat, N. Syed, M. Mohiuddin, M. M. Y. A. Alsaif, R. S. Datta, K. A. Messalea, B. Y. Zhang, M. W. Khan, A. Elbourne, N. Pillai, J. Z. Ou, A. Zavabeti, T. Daeneke, *Chem. Commun.* **2020**, *56*, 4914.

[135] P. Atkin, R. Orrell-Trigg, A. Zavabeti, N. Mahmood, M. R. Field, T. Daeneke, I. S. Cole, K. Kalantar-zadeh, *Chem. Commun.* **2018**, *54*, 2102.

[136] M. M. Y. A. Alsaif, S. Kuriakose, S. Walia, N. Syed, A. Jannat, B. Y. Zhang, F. Haque, M. Mohiuddin, T. Alkathiri, N. Pillai, T. Daeneke, J. Z. Ou, A. Zavabeti, *Adv. Mater. Interfaces* **2019**, *6*, 1900007.

[137] N. Syed, A. Zavabeti, K. A. Messalea, E. Della Gaspera, A. Elbourne, A. Jannat, M. Mohiuddin, B. Y. Zhang, G. Zheng, L. Wang, S. P. Russo, D. Esrafilzadeh, C. F. McConville, K. Kalantar-Zadeh, T. Daeneke, *Journal of the American Chemical Society* **2019**, *141*, 104.

[138] B. J. Carey, J. Z. Ou, R. M. Clark, K. J. Berean, A. Zavabeti, A. S. R. Chesman, S. P. Russo, D. W. M. Lau, Z.-Q. Xu, Q. Bao, O. Kavehei, B. C. Gibson, M. D. Dickey, R. B. Kaner, T. Daeneke, K. Kalantar-Zadeh, *Nat. Commun.* **2017**, *8*, 14482.

[139] A. Zavabeti, P. Aukarasereenont, H. Tuohey, N. Syed, A. Jannat, A. Elbourne, K. A. Messalea, B. Y. Zhang, B. J. Murdoch, J. G. Partridge, M. Wurdack, D. L. Creedon, J. van Embden, K. Kalantar-Zadeh, S. P. Russo, C. F. McConville, T. Daeneke, *Nat. Electron.* **2021**, *4*, 277.

[140] N. Syed, A. Zavabeti, M. Mohiuddin, B. Zhang, Y. Wang, R. S. Datta, P. Atkin, B. J. Carey, C. Tan, J. van Embden, A. S. R. Chesman, J. Z. Ou, T. Daeneke, K. Kalantar-zadeh, *Adv. Funct. Mater.* **2017**, *27*, 1702295.

[141] J. Crawford, A. Cowman, A. P. O'Mullane, *RSC Adv.* **2020**, *10*, 29181.

[142] M. B. Ghasemian, M. Mayyas, S. A. Idrus-Saidi, M. A. Jamal, J. Yang, S. S. Mofarah, E. Adabifiroozjaei, J. Tang, N. Syed, A. P. O'Mullane, T. Daeneke, K. Kalantar-Zadeh, *Adv. Funct. Mater.* **2019**, *29*, 1901649.

WILEY-VCH

[143]   M. Wurdack, T. Yun, E. Estrecho, N. Syed, S. Bhattacharyya, M. Pieczarka, A. Zavabeti, S.-Y. Chen, B. Haas, J. Müller, M. N. Lockrey, Q. Bao, C. Schneider, Y. Lu, M. S. Fuhrer, A. G. Truscott, T. Daeneke, E. A. Ostrovskaya, *Adv. Mater.* **2021**, *33*, 2005732.

[144]   K. Xing, P. Aukarasereenont, S. Rubanov, A. Zavabeti, D. L. Creedon, W. Li, B. C. Johnson, C. I. Pakes, J. C. McCallum, T. Daeneke, D.-C. Qi, *ACS Appl. Electron. Mater.* **2022**, *4*, 2272.

[145]   K. A. Messalea, B. J. Carey, A. Jannat, N. Syed, M. Mohiuddin, B. Y. Zhang, A. Zavabeti, T. Ahmed, N. Mahmood, E. Della Gaspera, K. Khoshmanesh, K. Kalantar-Zadeh, T. Daeneke, *Nanoscale* **2018**, *10*, 15615.

[146]   T. Daeneke, P. Atkin, R. Orrell-Trigg, A. Zavabeti, T. Ahmed, S. Walia, M. Liu, Y. Tachibana, M. Javaid, A. D. Greentree, S. P. Russo, R. B. Kaner, K. Kalantar-Zadeh, *ACS Nano* **2017**, *11*, 10974.

[147]   K. A. Messalea, N. Syed, A. Zavabeti, M. Mohiuddin, A. Jannat, P. Aukarasereenont, C. K. Nguyen, M. X. Low, S. Walia, B. Haas, C. T. Koch, N. Mahmood, K. Khoshmanesh, K. Kalantar-Zadeh, T. Daeneke, *ACS Nano* **2021**, *15*, 16067.

[148]   A. Azam, J. Kim, J. Park, T. G. Novak, A. P. Tiwari, S. H. Song, B. Kim, S. Jeon, *Nano Lett.* **2018**, *18*, 5646.

[149]   B. Chamlagain, Q. Cui, S. Paudel, M. M.-C. Cheng, P.-Y. Chen, Z. Zhou, *2D Mater.* **2017**, *4*, 031002.

[150]   J. Chen, Q. Wang, Y. Sheng, G. Cao, P. Yang, Y. Shan, F. Liao, Z. Muhammad, W. Bao, L. Hu, R. Liu, C. Cong, Z.-J. Qiu, *ACS Appl. Mater. Interfaces* **2019**, *11*, 43330.

[151]   S. Kang, Y. S. Kim, J. H. Jeong, J. Kwon, J. H. Kim, Y. Jung, J. C. Kim, B. Kim, S. H. Bae, P. Y. Huang, J. C. Hone, H. Y. Jeong, J.-W. Park, C.-H. Lee, G.-H. Lee, *ACS Appl. Mater. Interfaces* **2021**, *13*, 1245.

[152]   M. Yamamoto, S. Dutta, S. Aikawa, S. Nakaharai, K. Wakabayashi, M. S. Fuhrer, K. Ueno, K. Tsukagoshi, *Nano Lett.* **2015**, *15*, 2067.

[153]   C.-S. Pang, T. Y. T. Hung, A. Khosravi, R. Addou, Q. Wang, M. J. Kim, R. M. Wallace, Z. Chen, *Adv. Electron. Mater.* **2020**, *6*, 1901304.

[154]   H. Zhu, X. Qin, L. Cheng, A. Azcatl, J. Kim, R. M. Wallace, *ACS Appl. Mater. Interfaces* **2016**, *8*, 19119.

[155]   W. Feng, X. Wang, J. Zhang, L. Wang, W. Zheng, P. Hu, W. Cao, B. Yang, *J. Mater. Chem. C* **2014**, *2*, 3254.

[156]   T. Li, T. Tu, Y. Sun, H. Fu, J. Yu, L. Xing, Z. Wang, H. Wang, R. Jia, J. Wu, C. Tan, Y. Liang, Y. Zhang, C. Zhang, Y. Dai, C. Qiu, M. Li, R. Huang, L. Jiao, K. Lai, B. Yan, P. Gao, H. Peng, *Nat. Electron.* **2020**, *3*, 473.

[157]   Y. Zhang, J. Yu, R. Zhu, M. Wang, C. Tan, T. Tu, X. Zhou, C. Zhang, M. Yu, X. Gao, Y. Wang, H. Liu, P. Gao, K. Lai, H. Peng, *Nat. Electron.* **2022**.

[158]   T. Tu, Y. Zhang, T. Li, J. Yu, L. Liu, J. Wu, C. Tan, J. Tang, Y. Liang, C. Zhang, Y. Dai, Y. Han, K. Lai, H. Peng, *Nano Lett.* **2020**, *20*, 7469.

[159]   S. Lai, S. Byeon, S. K. Jang, J. Lee, B. H. Lee, J.-H. Park, Y.-H. Kim, S. Lee, *Nanoscale* **2018**, *10*, 18758.

[160]   S. Wang, L. Pan, J.-J. Song, W. Mi, J.-J. Zou, L. Wang, X. Zhang, *Journal of the American Chemical Society* **2015**, *137*, 2975.

[161]   L. Li, Y. Yu, G. J. Ye, Q. Ge, X. Ou, H. Wu, D. Feng, X. H. Chen, Y. Zhang, *Nat. Nanotechnol.* **2014**, *9*, 372.

[162]   H. Zhou, C. Wang, J. C. Shaw, R. Cheng, Y. Chen, X. Huang, Y. Liu, N. O. Weiss, Z. Lin, Y. Huang, X. Duan, *Nano Lett.* **2015**, *15*, 709.

[163]   K. J. Saji, K. Tian, M. Snure, A. Tiwari, *Adv. Electron. Mater.* **2016**, *2*, 1500453.

[164]   Z. Wang, X. He, X.-X. Zhang, H. N. Alshareef, *Adv. Mater.* **2016**, *28*, 9133.

[165]   Y. Tang, C.-H. Huang, K. Nomura, *ACS Nano* **2022**, *16*, 3280.

[166]   J. Lin, Q. Li, T.-Y. Liu, Y. Cui, H. Zheng, J. Liu, *physica status solidi (RRL) – Rapid Research Letters* **2019**, *13*, 1900271.

[167]   X. Yu, T. J. Marks, A. Facchetti, *Nat. Mater.* **2016**, *15*, 383.

[168]   P. Aukarasereenont, A. Goff, C. K. Nguyen, C. F. McConville, A. Elbourne, A. Zavabeti, T. Daeneke, *Chem. Soc. Rev.* **2022**, *51*, 1253.

[169]   D. C. Hays, B. P. Gila, S. J. Pearton, F. Ren, *Appl. Phys. Rev.* **2017**, *4*, 021301.

[170]   J. H. Choi, Y. Mao, J. P. Chang, *Materials Science and Engineering: R: Reports* **2011**, *72*, 97.

[171]   M. L. Green, M. Y. Ho, B. Busch, G. D. Wilk, T. Sorsch, T. Conard, B. Brijs, W. Vandervorst, P. I. Räisänen, D. Muller, M. Bude, J. Grazul, *J. Appl. Phys.* **2002**, *92*, 7168.

[172]   H. G. Kim, H.-B.-R. Lee, *Chem. Mater.* **2017**, *29*, 3809.

[173]   Y. Zhu, Y. Li, G. Arefe, R. A. Burke, C. Tan, Y. Hao, X. Liu, X. Liu, W. J. Yoo, M. Dubey, Q. Lin, J. C. Hone, *Nano Lett.* **2018**, *18*, 3807.

[174]   J. Wang, S. Li, X. Zou, J. Ho, L. Liao, X. Xiao, C. Jiang, W. Hu, J. Wang, J. Li, *Small* **2015**, *11*, 5932.

[175]   J. H. Park, S. Fathipour, I. Kwak, K. Sardashti, C. F. Ahles, S. F. Wolf, M. Edmonds, S. Vishwanath, H. G. Xing, S. K. Fullerton-Shirey, A. Seabaugh, A. C. Kummel, *ACS Nano* **2016**, *10*, 6888.

[176]   L. Britnell, R. V. Gorbachev, R. Jalil, B. D. Belle, F. Schedin, M. I. Katsnelson, L. Eaves, S. V. Morozov, A. S. Mayorov, N. M. R. Peres, A. H. Castro Neto, J. Leist, A. K. Geim, L. A. Ponomarenko, K. S. Novoselov, *Nano Lett.* **2012**, *12*, 1707.

[177]   Y. Liu, J. Guo, E. Zhu, L. Liao, S.-J. Lee, M. Ding, I. Shakir, V. Gambin, Y. Huang, X. Duan, *Nature* **2018**, *557*, 696.

[178]   J. Mleczko Michal, C. Zhang, R. Lee Hye, H.-H. Kuo, B. Magyari-Köpe, G. Moore Robert, Z.-X. Shen, R. Fisher Ian, Y. Nishi, E. Pop, *Sci. Adv.*, *3*, e1700481.

[179]   A. I. Kingon, J.-P. Maria, S. K. Streiffer, *Nature* **2000**, *406*, 1032.

[180]   I. Vickridge, J. Ganem, Y. Hoshino, I. Trimaille, *J. Phys. D: Appl. Phys.* **2007**, *40*, 6254.

[181]   K. Xu, Y. Huang, B. Chen, Y. Xia, W. Lei, Z. Wang, Q. Wang, F. Wang, L. Yin, J. He, *Small* **2016**, *12*, 3106.

[182]   W. Li, J. Zhou, S. Cai, Z. Yu, J. Zhang, N. Fang, T. Li, Y. Wu, T. Chen, X. Xie, H. Ma, K. Yan, N. Dai, X. Wu, H. Zhao, Z. Wang, D. He, L. Pan, Y. Shi, P. Wang, W. Chen, K. Nagashio, X. Duan, X. Wang, *Nat. Electron.* **2019**, *2*, 563.

[183]   C. Wen, A. G. Banshchikov, Y. Y. Illarionov, W. Frammelsberger, T. Knobloch, F. Hui, N. S. Sokolov, T. Grasser, M. Lanza, *Adv. Mater.* **2020**, *32*, 2002525.

[184]   J. Peng, W. Pu, S. Lu, X. Yang, C. Wu, N. Wu, Z. Sun, H.-T. Wang, *Nano Lett.* **2021**, *21*, 203.

[185]   H. S. Kum, H. Lee, S. Kim, S. Lindemann, W. Kong, K. Qiao, P. Chen, J. Irwin, J. H. Lee, S. Xie, S. Subramanian, J. Shim, S.-H. Bae, C. Choi, L. Ranno, S. Seo, S. Lee, J. Bauer, H. Li, K. Lee, J. A. Robinson, C. A. Ross, D. G. Schlom, M. S. Rzchowski, C.-B. Eom, J. Kim, *Nature* **2020**, *578*, 75.

[186]   A. J. Yang, K. Han, K. Huang, C. Ye, W. Wen, R. Zhu, R. Zhu, J. Xu, T. Yu, P. Gao, Q. Xiong, X. Renshaw Wang, *Nat. Electron.* **2022**, *5*, 233.

[187]   S. Lee, A. Tang, S. Aloni, H. S. Philip Wong, *Nano Lett.* **2016**, *16*, 276.

[188]   Y. Pak, W. Park, S. Mitra, A. A. Sasikala Devi, K. Loganathan, Y. Kumaresan, Y. Kim, B. Cho, G.-Y. Jung, M. M. Hussain, I. S. Roqan, *Small* **2018**, *14*, 1703176.

[189]   N. Kaushik, D. Karmakar, A. Nipane, S. Karande, S. Lodha, *ACS Appl. Mater. Interfaces* **2016**, *8*, 256.

[190]   J.-R. Chen, P. M. Odenthal, A. G. Swartz, G. C. Floyd, H. Wen, K. Y. Luo, R. K. Kawakami, *Nano Lett.* **2013**, *13*, 3106.

[191]   J. Wang, Q. Yao, C.-W. Huang, X. Zou, L. Liao, S. Chen, Z. Fan, K. Zhang, W. Wu, X. Xiao, C. Jiang, W.-W. Wu, *Adv. Mater.* **2016**, *28*, 8302.

[192]   A. M. Roy, J. Y. J. Lin, K. C. Saraswat, *IEEE Electron Device Lett.* **2010**, *31*, 1077.

[193]   M. H. Liao, C. Lien, *AIP Adv.* **2015**, *5*, 057117.

[194]   S. Gupta, P. P. Manik, R. K. Mishra, A. Nainani, M. C. Abraham, S. Lodha, *J. Appl. Phys.* **2013**, *113*, 234505.

[195]   S. Chuang, C. Battaglia, A. Azcatl, S. McDonnell, J. S. Kang, X. Yin, M. Tosun, R. Kapadia, H. Fang, R. M. Wallace, A. Javey, *Nano Lett.* **2014**, *14*, 1337.

[196]   M. Farmanbar, G. Brocks, *Adv. Electron. Mater.* **2016**, *2*, 1500405.

[197]   A. Leonhardt, D. Chiappe, V. V. Afanas'ev, S. El Kazzi, I. Shlyakhov, T. Conard, A. Franquet, C. Huyghebaert, S. de Gendt, *ACS Appl. Mater. Interfaces* **2019**, *11*, 42697.

[198]   C. Zhou, Y. Zhao, S. Raju, Y. Wang, Z. Lin, M. Chan, Y. Chai, *Adv. Funct. Mater.* **2016**, *26*, 4223.

[199]   Y. J. Park, A. K. Katiyar, A. T. Hoang, J.-H. Ahn, *Small* **2019**, *15*, 1901772.

[200]   B. A. Holler, K. Crowley, M. H. Berger, X. P. A. Gao, *Adv. Electron. Mater.* **2020**, *6*.

[201]   K. G. Crawford, J. D. Weil, P. B. Shah, D. A. Ruzmetov, M. R. Neupane, K. Kingkeo, A. G. Birdwell, T. G. Ivanov, *IEEE Trans. Electron Devices* **2020**, *67*, 2270.

[202]   Z. Ren, J. Zhang, J. Zhang, C. Zhang, S. Xu, Y. Li, Y. Hao, *IEEE Electron Device Lett.* **2017**, *38*, 786.

[203]   Z. Yin, M. Tordjman, A. Vardi, R. Kalish, J. A. d. Alamo, *IEEE Electron Device Lett.* **2018**, *39*, 540.

[204]   A. Surrente, D. Dumcenco, Z. Yang, A. Kuc, Y. Jing, T. Heine, Y.-C. Kung, D. K. Maude, A. Kis, P. Plochocka, *Nano Lett.* **2017**, *17*, 4130.

[205]   T. Knobloch, Y. Y. Illarionov, F. Ducry, C. Schleich, S. Wachter, K. Watanabe, T. Taniguchi, T. Mueller, M. Waltl, M. Lanza, M. I. Vexler, M. Luisier, T. Grasser, *Nat. Electron.* **2021**, *4*, 98.

[206]   N. Fang, S. Toyoda, T. Taniguchi, K. Watanabe, K. Nagashio, *Adv. Funct. Mater.* **2019**, *29*, 1904465.

[207]   G.-H. Lee, Y.-J. Yu, C. Lee, C. Dean, K. L. Shepard, P. Kim, J. Hone, *Appl. Phys. Lett.* **2011**, *99*, 243114.

[208]   M. Long, P. Wang, H. Fang, W. Hu, *Adv. Funct. Mater.* **2019**, *29*, 1803807.

[209]   N. Huo, G. Konstantatos, *Adv. Mater.* **2018**, *30*, 1801164.

[210]   M. Zhong, K. Zhou, Z. Wei, Y. Li, T. Li, H. Dong, L. Jiang, J. Li, W. Hu, *2D Mater.* **2018**, *5*, 035033.

[211]   N. Balakrishnan, Z. R. Kudrynskyi, E. F. Smith, M. W. Fay, O. Makarovsky, Z. D. Kovalyuk, L. Eaves, P. H. Beton, A. Patanè, *2D Mater.* **2017**, *4*, 025043.

[212]   N. Guo, L. Xiao, F. Gong, M. Luo, F. Wang, Y. Jia, H. Chang, J. Liu, Q. Li, Y. Wu, Y. Wang, C. Shan, Y. Xu, P. Zhou, W. Hu, *Adv. Sci.* **2020**, *7*, 1901637.

[213]   S. Feng, C. Liu, Q. Zhu, X. Su, W. Qian, Y. Sun, C. Wang, B. Li, M. Chen, L. Chen, W. Chen, L. Zhang, C. Zhen, F. Wang, W. Ren, L. Yin, X. Wang, H.-M. Cheng, D.-M. Sun, *Nat. Commun.* **2021**, *12*, 4094.

[214]   Z. X. Jiang, Z. Y. Wu, C. C. Ma, J. N. Deng, H. Zhang, Y. Xu, J. D. Ye, Z. L. Fang, G. Q. Zhang, J. Y. Kang, T. Y. Zhang, *Mater. Today Phys.* **2020**, *14*, 100226.

[215]   Y. Qin, L.-H. Li, Z. Yu, F. Wu, D. Dong, W. Guo, Z. Zhang, J.-H. Yuan, K.-H. Xue, X. Miao, S. Long, *Adv. Sci.* **2021**, *8*, 2101106.

[216]   R. Lin, W. Zheng, D. Zhang, Y. Li, F. Huang, *ACS Appl. Electron. Mater.* **2019**, *1*, 2166.

[217]   J. Xu, W. Zheng, F. Huang, *J. Mater. Chem. C* **2019**, *7*, 8753.

[218]   X. Hou, X. Zhao, Y. Zhang, Z. Zhang, Y. Liu, Y. Qin, P. Tan, C. Chen, S. Yu, M. Ding, G. Xu, Q. Hu, S. Long, *Adv. Mater.* **2022**, *34*, 2106923.

[219]   S. Goossens, G. Navickaite, C. Monasterio, S. Gupta, J. J. Piqueras, R. Pérez, G. Burwell, I. Nikitskiy, T. Lasanta, T. Galán, E. Puma, A. Centeno, A. Pesquera, A. Zurutuza, G. Konstantatos, F. Koppens, *Nat. Photonics* **2017**, *11*, 366.

[220]   S. Hong, N. Zagni, S. Choo, N. Liu, S. Baek, A. Bala, H. Yoo, B. H. Kang, H. J. Kim, H. J. Yun, M. A. Alam, S. Kim, *Nat. Commun.* **2021**, *12*, 3559.

[221]   C. Choi, M. K. Choi, S. Liu, M. Kim, O. K. Park, C. Im, J. Kim, X. Qin, G. J. Lee, K. W. Cho, M. Kim, E. Joh, J. Lee, D. Son, S.-H. Kwon, N. L. Jeon, Y. M. Song, N. Lu, D.-H. Kim, *Nat. Commun.* **2017**, *8*, 1664.

[222]   Q.-B. Zhu, B. Li, D.-D. Yang, C. Liu, S. Feng, M.-L. Chen, Y. Sun, Y.-N. Tian, X. Su, X.-M. Wang, S. Qiu, Q.-W. Li, X.-M. Li, H.-B. Zeng, H.-M. Cheng, D.-M. Sun, *Nat. Commun.* **2021**, *12*, 1798.

[223]   C. Choi, J. Leem, M. Kim, A. Taqieddin, C. Cho, K. W. Cho, G. J. Lee, H. Seung, H. J. Bae, Y. M. Song, T. Hyeon, N. R. Aluru, S. Nam, D.-H. Kim, *Nat. Commun.* **2020**, *11*, 5934.

[224]   L. Mennel, J. Symonowicz, S. Wachter, D. K. Polyushkin, A. J. Molina-Mendoza, T. Mueller, *Nature* **2020**, *579*, 62.

[225]   C. Pan, J. Zhai, Z. L. Wang, *Chem. Rev.* **2019**, *119*, 9303.

[226]   W. Wu, X. Wen, L. Wang Zhong, *Science* **2013**, *340*, 952.

[227]   S. Liu, L. Wang, X. Feng, Z. Wang, Q. Xu, S. Bai, Y. Qin, Z. L. Wang, *Adv. Mater.* **2017**, *29*, 1606346.

[228]   L. Wang, S. Liu, G. Gao, Y. Pang, X. Yin, X. Feng, L. Zhu, Y. Bai, L. Chen, T. Xiao, X. Wang, Y. Qin, Z. L. Wang, *ACS Nano* **2018**, *12*, 4903.

[229]   C. An, H. Qi, L. Wang, X. Fu, A. Wang, Z. L. Wang, J. Liu, *Nano Energy* **2021**, *82*, 105653.

[230]   S. Bellani, A. Bartolotta, A. Agresti, G. Calogero, G. Grancini, A. Di Carlo, E. Kymakis, F. Bonaccorso, *Chem. Soc. Rev.* **2021**, *50*, 11870.

[231]   A. Pérez-Tomás, A. Mingorance, D. Tanenbaum, M. Lira-Cantú, in *The Future of Semiconductor Oxides in Next-Generation Solar Cells*, (Ed: M. Lira-Cantu), Elsevier, 2018.

[232]   A. Preuß, B. Adolphi, T. Wegener, *Fresenius' Journal of Analytical Chemistry* **1995**, *353*, 399.

[233]   N. Nadaud, N. Lequeux, M. Nanot, J. Jové, T. Roisnel, *J. Solid State Chem.* **1998**, *135*, 140.

[234]   S. Bae, H. Kim, Y. Lee, X. Xu, J.-S. Park, Y. Zheng, J. Balakrishnan, T. Lei, H. Ri Kim, Y. I. Song, Y.-J. Kim, K. S. Kim, B. Özyilmaz, J.-H. Ahn, B. H. Hong, S. Iijima, *Nat. Nanotechnol.* **2010**, *5*, 574.

[235]   J. F. Sierra, J. Fabian, R. K. Kawakami, S. Roche, S. O. Valenzuela, *Nat. Nanotechnol.* **2021**, *16*, 856.

[236]   X. Lin, W. Yang, K. L. Wang, W. Zhao, *Nat. Electron.* **2019**, *2*, 274.

WILEY-VCH

[237] Q. Hao, H. Dai, M. Cai, X. Chen, Y. Xing, H. Chen, T. Zhai, X. Wang, J.-B. Han, *Adv. Electron. Mater.*, *n/a*, 2200164.

[238] A. I. Braginski, *J. Supercond. Novel Magn.* **2019**, *32*, 23.

[239] S. Frasca, E. Charbon, *Nat. Electron.* **2019**, *2*, 433.

[240] A. N. McCaughan, V. B. Verma, S. M. Buckley, J. P. Allmaras, A. G. Kozorezov, A. N. Tait, S. W. Nam, J. M. Shainline, *Nat. Electron.* **2019**, *2*, 451.

[241] Y. Saito, T. Nojima, Y. Iwasa, *Nat. Rev. Mater.* **2016**, *2*, 16094.

[242] D. Qiu, C. Gong, S. Wang, M. Zhang, C. Yang, X. Wang, J. Xiong, *Adv. Mater.* **2021**, *33*, 2006124.

[243] D. Jiang, T. Hu, L. You, Q. Li, A. Li, H. Wang, G. Mu, Z. Chen, H. Zhang, G. Yu, J. Zhu, Q. Sun, C. Lin, H. Xiao, X. Xie, M. Jiang, *Nat. Commun.* **2014**, *5*, 5708.

[244] Z. Chen, A. G. Swartz, H. Yoon, H. Inoue, T. A. Merz, D. Lu, Y. Xie, H. Yuan, Y. Hikita, S. Raghu, H. Y. Hwang, *Nat. Commun.* **2018**, *9*, 4008.

[245] K. Ueno, S. Nakamura, H. Shimotani, A. Ohtomo, N. Kimura, T. Nojima, H. Aoki, Y. Iwasa, M. Kawasaki, *Nat. Mater.* **2008**, *7*, 855.

[246] A. T. Bollinger, G. Dubuis, J. Yoon, D. Pavuna, J. Misewich, I. Božović, *Nature* **2011**, *472*, 458.

[247] A. R. Oganov, C. J. Pickard, Q. Zhu, R. J. Needs, *Nat. Rev. Mater.* **2019**, *4*, 331.

[248] L. Wang, M. S. H. Boutilier, P. R. Kidambi, D. Jang, N. G. Hadjiconstantinou, R. Karnik, *Nat. Nanotechnol.* **2017**, *12*, 509.

[249] C. R. Dean, A. F. Young, I. Meric, C. Lee, L. Wang, S. Sorgenfrei, K. Watanabe, T. Taniguchi, P. Kim, K. L. Shepard, J. Hone, *Nat. Nanotechnol.* **2010**, *5*, 722.

[250] C. Su, Z. Yin, Q.-B. Yan, Z. Wang, H. Lin, L. Sun, W. Xu, T. Yamada, X. Ji, N. Zettsu, K. Teshima, J. H. Warner, M. Dincă, J. Hu, M. Dong, G. Su, J. Kong, J. Li, *Proceedings of the National Academy of Sciences* **2019**, *116*, 20844.

[251] J.-H. Lee, E. K. Lee, W.-J. Joo, Y. Jang, B.-S. Kim, J. Y. Lim, S.-H. Choi, S. J. Ahn, J. R. Ahn, M.-H. Park, C.-W. Yang, B. L. Choi, S.-W. Hwang, D. Whang, *Science* **2014**, *344*, 286.

[252] K. V. Emtsev, A. Bostwick, K. Horn, J. Jobst, G. L. Kellogg, L. Ley, J. L. McChesney, T. Ohta, S. A. Reshanov, J. Röhrl, E. Rotenberg, A. K. Schmid, D. Waldmann, H. B. Weber, T. Seyller, *Nat. Mater.* **2009**, *8*, 203.

[253] T. Wu, X. Zhang, Q. Yuan, J. Xue, G. Lu, Z. Liu, H. Wang, H. Wang, F. Ding, Q. Yu, X. Xie, M. Jiang, *Nat. Mater.* **2016**, *15*, 43.

[254] A. R. Jang, S. Hong, C. Hyun, S. I. Yoon, G. Kim, H. Y. Jeong, T. J. Shin, S. O. Park, K. Wong, S. K. Kwak, N. Park, K. Yu, E. Choi, A. Mishchenko, F. Withers, K. S. Novoselov, H. Lim, H. S. Shin, *Nano Lett.* **2016**, *16*, 3360.

[255] P. Yang, S. Zhang, S. Pan, B. Tang, Y. Liang, X. Zhao, Z. Zhang, J. Shi, Y. Huan, Y. Shi, S. J. Pennycook, Z. Ren, G. Zhang, Q. Chen, X. Zou, Z. Liu, Y. Zhang, *ACS Nano* **2020**, *14*, 5036.

[256] J. Wang, X. Xu, T. Cheng, L. Gu, R. Qiao, Z. Liang, D. Ding, H. Hong, P. Zheng, Z. Zhang, Z. Zhang, S. Zhang, G. Cui, C. Chang, C. Huang, J. Qi, J. Liang, C. Liu, Y. Zuo, G. Xue, X. Fang, J. Tian, M. Wu, Y. Guo, Z. Yao, Q. Jiao, L. Liu, P. Gao, Q. Li, R. Yang, G. Zhang, Z. Tang, D. Yu, E. Wang, J. Lu, Y. Zhao, S. Wu, F. Ding, K. Liu, *Nat. Nanotechnol.* **2022**, *17*, 33.

[257] X. Xu, Z. Wang, S. Lopatin, M. A. Quevedo-Lopez, H. N. Alshareef, *2D Mater.* **2019**, *6*, 015030.

[258] Y. Liu, Y. Huang, X. Duan, *Nature* **2019**, *567*, 323.

[259]   S. Najmaei, M. R. Neupane, B. M. Nichols, R. A. Burke, A. L. Mazzoni, M. L. Chin, D. A. Rhodes, L. Balicas, A. D. Franklin, M. Dubey, *Small* **2018**, *14*, 1703808.

[260]   D. Jena, K. Banerjee, G. H. Xing, *Nat. Mater.* **2014**, *13*, 1076.

[261]   N. Hong, D. Kireev, Q. Zhao, D. Chen, D. Akinwande, W. Li, *Adv. Mater.* **2022**, *34*, 2106615.

[262]   Y. Wang, M. Zhang, Z. Xue, X. Chen, Y. Mei, P. K. Chu, Z. Tian, X. Wu, Z. Di, *Small* **2022**, *18*, 2200913.

[263]   S. Carr, D. Massatt, S. Fang, P. Cazeaux, M. Luskin, E. Kaxiras, *Phys. Rev. B* **2017**, *95*, 075420.

[264]   O. Can, T. Tummuru, R. P. Day, I. Elfimov, A. Damascelli, M. Franz, *Nat. Phys.* **2021**, *17*, 519.

[265]   G. Feng, J. Jiang, Y. Li, D. Xie, B. Tian, Q. Wan, *Adv. Funct. Mater.* **2021**, *31*, 2104327.

[266]   L. Wang, S. Liu, Z. Zhang, X. Feng, L. Zhu, H. Guo, W. Ding, L. Chen, Y. Qin, Z. L. Wang, *Nano Energy* **2019**, *60*, 724.

[267]   H. Wu, X. Zhou, J. Li, X. Li, B. Li, W. Fei, J. Zhou, J. Yin, W. Guo, *Small* **2018**, *14*, 1802276.

[268]   J. Wang, C. Teng, Z. Zhang, W. Chen, J. Tan, Y. Pan, R. Zhang, H. Zhou, B. Ding, H.-M. Cheng, B. Liu, *ACS Nano* **2021**, *15*, 15123.

[269]   A. J. Molina-Mendoza, J. L. Lado, J. O. Island, M. A. Niño, L. Aballe, M. Foerster, F. Y. Bruno, A. López-Moreno, L. Vaquero-Garzon, H. S. J. van der Zant, G. Rubio-Bollinger, N. Agraït, E. M. Pérez, J. Fernández-Rossier, A. Castellanos-Gomez, *Chem. Mater.* **2016**, *28*, 4042.

[270]   S. Puebla, R. D'Agosta, G. Sanchez-Santolino, R. Frisenda, C. Munuera, A. Castellanos-Gomez, *npj 2D Mater. Appl.* **2021**, *5*, 37.

[271]   A. Arash, T. Ahmed, A. Govind Rajan, S. Walia, F. Rahman, A. Mazumder, R. Ramanathan, S. Sriram, M. Bhaskaran, E. Mayes, M. S. Strano, S. Balendhran, *2D Mater.* **2019**, *6*, 035031.

[272]   K. v. Benthem, C. Elsässer, R. H. French, *J. Appl. Phys.* **2001**, *90*, 6156.

[273]   J. H. Kim, J. K. Dash, J. Kwon, C. Hyun, H. Kim, E. Ji, G.-H. Lee, *2D Mater.* **2018**, *6*, 015016.

[274]   S. Balendhran, J. Deng, J. Z. Ou, S. Walia, J. Scott, J. Tang, K. L. Wang, M. R. Field, S. Russo, S. Zhuiykov, M. S. Strano, N. Medhekar, S. Sriram, M. Bhaskaran, K. Kalantar-zadeh, *Adv. Mater.* **2013**, *25*, 109.

[275]   Q. Smets, G. Arutchelvan, J. Jussot, D. Verreck, I. Asselberghs, A. N. Mehta, A. Gaur, D. Lin, S. E. Kazzi, B. Groven, M. Caymax, I. Radu, presented at *2019 IEEE International Electron Devices Meeting (IEDM)*, 7-11 Dec. 2019, **2019**.

[276]   X. Wang, T.-B. Zhang, W. Yang, H. Zhu, L. Chen, Q.-Q. Sun, D. W. Zhang, *Appl. Phys. Lett.* **2017**, *110*, 053110.

[277]   S.-J. Jeong, Y. Gu, J. Heo, J. Yang, C.-S. Lee, M.-H. Lee, Y. Lee, H. Kim, S. Park, S. Hwang, *Sci. Rep.* **2016**, *6*, 20907.

[278]   X. Zou, J. Wang, C.-H. Chiu, Y. Wu, X. Xiao, C. Jiang, W.-W. Wu, L. Mai, T. Chen, J. Li, J. C. Ho, L. Liao, *Adv. Mater.* **2014**, *26*, 6255.

[279]   K. Ashokbhai Patel, R. W. Grady, K. K. H. Smithe, E. Pop, R. Sordan, *2D Mater.* **2019**, *7*, 015018.

[280]   W. Zheng, R. Lin, Y. Zhu, Z. Zhang, X. Ji, F. Huang, *ACS Appl. Mater. Interfaces* **2018**, *10*, 20696.

Accepted Article

Kui Zhou received his Ph.D. degree in Materials Science and Engineering from Wuhan University of Technology in 2017. He is currently an associate research fellow in the Institute for Advanced Study, Shenzhen University. His research interests focus on cluster-assembled materials and metal–organic frameworks, as well as their promising applications in electronics and optoelectronics.

Ye Zhou is a Fellow of the Royal Society of Chemistry (FRSC), a Fellow of the Institute of Physics (FInstP), a Fellow of the Institution of Engineering and Technology (FIET), and a group leader in the Institute for Advanced Study, Shenzhen University. His research interests include nanostructured materials and nano-scale devices for technological applications, such as logic circuits, data storage, photonics, and sensors.